

ADVANCES IN

Adhesives, Adhesion Science, and Testing

STP 1463

Editor:
Dennis Damico



INTERNATIONAL
Standards Worldwide

STP 1463

Advances in Adhesives, Adhesion Science, and Testing

Dennis Damico, editor

ASTM Stock Number: STP1463



ASTM International
100 Barr Harbor Drive
PO Box C700
West Conshohocken, PA 19428-2959

Printed in the U.S.A.

Library of Congress Cataloging-in-Publication Data

Symposium on Advances in Adhesives, Adhesion Science, and Testing (2004 : Washington, D.C.)

Advances in adhesives, adhesion science, and testing / Dennis Damico, editor.

p. cm. — (STP ; 1463)

ISBN: 0-8031-3489-4 (alk. paper)

1. Adhesives—Congresses. 2. Adhesion—Research—Congresses. 3. Adhesion—Testing—Congresses. I. Damico, Dennis J., 1947– II. Title. III. Series: ASTM special technical publication ; 1463.

TP967.S956 2004

620.1'99—dc22

2005022769

Copyright © 2005 ASTM International, West Conshohocken, PA. All rights reserved. This material may not be reproduced or copied, in whole or in part, in any printed, mechanical, electronic, film, or other distribution and storage media, without the written consent of the publisher.

Photocopy Rights

Authorization to photocopy items for internal, personal, or educational classroom use, or the internal, personal, or educational classroom use of specific clients, is granted by ASTM International (ASTM) provided that the appropriate fee is paid to the Copyright Clearance Center, 222 Rosewood Drive, Danvers, MA 01923; Tel: 978-750-8400; online: <http://www.copyright.com/>.

Peer Review Policy

Each paper published in this volume was evaluated by two peer reviewers and at least one editor. The authors addressed all of the reviewers' comments to the satisfaction of both the technical editor(s) and the ASTM International Committee on Publications.

To make technical information available as quickly as possible, the peer-reviewed papers in this publication were prepared "camera-ready" as submitted by the authors.

The quality of the papers in this publication reflects not only the obvious efforts of the authors and the technical editor(s), but also the work of the peer reviewers. In keeping with long-standing publication practices, ASTM International maintains the anonymity of the peer reviewers. The ASTM International Committee on Publications acknowledges with appreciation their dedication and contribution of time and effort on behalf of ASTM International.

Foreword

The Symposium on Advances in Adhesives, Adhesion Science, and Testing was held in Washington, DC on October 4, 2004. The Symposium was sponsored by ASTM Committee D14 on Adhesives. The chairman was Dennis Damico. He also served as editor for this publication.

Contents

| | |
|--|------|
| Overview | viii |
| Adhesive Bonding and Performance Testing of Bonded Wood Products —C R. FRIHART | 1 |
| A New Low Cost Method for Measuring the Viscoelastic Behavior of Adhesives —D. J. MOONAY, R. G. MCGREGOR, AND R. A. MASTRIA, JR. | 13 |
| Method for Quantifying Percentage Wood Failure in Block-Shear Specimens by a Laser Scanning Profilometer —C. T. SCOTT, R. HERNANDEZ, C. FRIHART, R. GLEISNER, AND T. TICE | 25 |
| SED Method of Measuring Yield Strength of Adhesives and Other Materials —A. LENWARI, P. ALBRECHT, AND M. ALBRECHT | 35 |
| Characterizing Dynamic Fracture Behavior of Adhesive Joints Under Quasi-Static and Impact loading —J. C. SIMÓN, E. JOHNSON, AND D. A. DILLARD | 53 |
| Interfacial Diffusion of Fluids in Pressure Sensitive Adhesives —E. P. O'BRIEN, T. C. WARD .. | 72 |
| Advanced Methods of Coating Adhesion Testing —N. V. GITIS, J. XIAO, AND M. VINOGRADOV | 80 |
| Fracture Mechanics Applied to Adhesive Joints —G. E. WHEELER, B. S. MADSEN, AND K. L. DeVRIES | 85 |
| The Study of Bond Strength and Bond Durability of Reactive Powder Concrete —M-G LEE, C-T CHIU, AND Y-C WANG | 104 |
| Evaluation of Different Techniques for Adhesive Properties of Asphalt-Filler Systems at Interfacial Region —S-C HUANG, T. F. TURNER, A. T. PAULI, F. P. MIKNIS, J. F. BRANTHAVER, AND R. E. ROBERTSON | 114 |
| New Technique for Measuring Extended Viscosity Ranges—Gel Times, Pot Life, or Cure Monitoring—with Programmable Rotational Viscometers or Rheometers —D. F. MOONNAY | 129 |

Overview

This symposium focused on new adhesives particularly from the perspective of newer test methods emerging to better determine adhesive reliability. Areas of particular interest included:

- Test methods and specifications that improve the ability to determine long-term bond durability,
- Bonding and debonding of wood products
- Test methods that generate more meaningful material information on adhesive reliability
- Method of measuring viscoelastic behavior of adhesives
- Accurate method of measuring yield strength of adhesives and other materials,
- Characterizing fracture properties of adhesive joints under impact loading conditions,
- Fracture mechanics applied to adhesives joints,
- Coating adhesion testing,
- Diffusion of fluids in pressure sensitive adhesives.

Information presented is of value to design engineers and those with interest in advanced test methods for adhesive validation.

The symposium also had a global focus more than ever before in bringing speakers from the U.S., Taiwan, and Republic of China.

Dennis Damico
Lord Corporation
Erie, Pennsylvania
Symposium Chairman and Editor

*Charles R. Frihart*¹

Adhesive Bonding and Performance Testing of Bonded Wood Products

ABSTRACT: Despite the importance of durable wood bonds, the factors that lead to durability are not well understood, and the internal forces exerted upon the bondline are often overlooked. Durability requires that the bonded assembly resist dimensional changes of wood with fluctuation of wood moisture levels. Both bonding and bond breaking steps need to be understood at cellular and nanoscale, in addition to the larger spatial scales normally examined. With both internal and external forces being significant, interphase and bulk adhesive properties need to be better understood. Systematic studies of the bonding process, the forces upon the bondline, and the locus of failure using different types of adhesives and wood species should improve our ability to design wood adhesives. Modifications of wood surfaces, along with spectroscopic and microscopic analyses, are important tools to understand bond formation and failure.

KEYWORDS: wood, bond formation, bond failure, cellular, microscopy

Introduction

Wood adhesives date back several millennia, and research on wood-adhesive interactions has been ongoing for over 75 years [1]. The past century has seen tremendous advances in adhesive chemistry, comprehension of the adhesion process, and knowledge on aspects that lead to failure in durability testing. For many applications, the critical aspects of bond formation that lead to durability have been well defined. However, the critical chemical and physical properties that lead to durable bonds have not been as well defined for wood adhesives as they have for metal and plastic adhesives. This discussion is not intended to ignore the excellent work that has been done in this field but rather to define where more work needs to be done.

Why are we still unable to define the chemistry and physical properties that are necessary to lead to a successful adhesive bond for a specific application? In reality, wood has more complex chemical, structural, and mechanical properties than most other substrates. This paper is aimed at addressing some of these issues.

The chemistry of wood adhesives has been studied extensively, mainly related to the initial reaction and polymerization stages, and is known well enough to predict the results of alteration in the chemistry [2]. The preparation of wood surfaces also has been studied, and optimum conditions have been determined [3]. Numerous studies have been carried out on the durability of wood bonds using both natural and accelerated aging [4]. Among the less well understood areas are adhesive interactions with wood surfaces, wood-adhesive interphase physical and mechanical properties, and failure zone for many wood bonds. Although some excellent studies have been done in these areas, knowledge is still insufficient to predict the performance of a new adhesive or different wood species, resulting in mainly a trial and error process. A better

Manuscript received 28 September 2004; accepted for publication 27 January 2005; published July 2005. Presented at ASTM Symposium on Advances in Adhesives, Adhesion Science, and Testing on 4-6 October 2004 in Washington, DC.

¹ Project Leader, Wood Adhesives Science and Technology, USDA Forest Service, Forest Products Laboratory, One Gifford Pinchot Drive, Madison, WI 53726 USA.

2 ADVANCES IN ADHESIVES, ADHESION SCIENCE, AND TESTING

understanding in these areas can aid in solving current adhesive problems, developing new adhesives, and providing new uses for wood adhesives. In general, bonding of wood is not difficult for specimens that are not under high continuous load or at high or varying moisture levels. Some factors that lead to durability of wood bonds have been discussed [3–5], but the understanding diminishes rapidly as the spatial scale being examined decreases from millimeter to micrometer (cellular) to nanometer (cellulose, hemicellulose, lignin domains) [6].

Wood failure is often considered to be as important as the strength of the bond. Deep wood failure is easy to observe, but determining where and why failure takes place in the bondline has been difficult. This paper presents ideas on how a better understanding of the failure of wood bonds can be obtained.

Experimental

Wood for these tests was obtained from local suppliers, with the actual test specimens selected according to the protocol in ASTM D 905 [7]. Wood species used were aspen, hard maple, Sitka spruce, southern yellow pine, and white oak. The wood was selected and prepared according to this method, bonded using FPL-1A [8] at a spread rate of 0.34 kg/m² and clamped for a day at room temperature at a pressure sufficient to cause a light squeeze out.

Specimens for microscopy were obtained from the bonded specimens and from the samples after the D 905 tests. For transverse sections, samples were water-soaked for 2–24 h prior to microtoming. The sections were analyzed using a scanning electron microscope (JEOL 840 after gold plating the samples) or a Leitz Orthoplan epi-fluorescence microscope with a 150-W mercury lamp light source, an A2 UV filter cube, and a Nikon DS-5M digital camera, or a Carl Zeiss Axioskop epi-fluorescence microscope with a 100-W mercury lamp, a UV filter set, and CCD camera. Fluorescence microscopy was used to examine the failure surface.

Bonding

High bond strength and durability depend upon developing excellent adhesive-wood interaction and good dissipation of internal and external forces under end use conditions. Wood adhesion models have generally been based upon general adhesion models, which concentrate on surface interactions between the adhesive and the adherend. These general models work well for most adherends but need to be modified when wood is the substrate. Factors causing these modifications include adhesive penetration into the wood, high wood surface roughness, the multi-polymer composition of wood, and wood variability. These factors do not displace the importance of primary or secondary bonds between the wood and the adhesive used in normal adhesion theory but can be additional mechanisms that can either increase or decrease the durability of the interphase region. For understanding wood bond strength, Horioka used the analogy of links in a chain [5]; each domain is a separate link, and the weakest link is the site of failure. To use this analogy, one needs to understand what these links look like in a real bond. In Fig. 1, fluorescence microscopy is used to distinguish the adhesive from the wood. The striking feature in this photograph is how large the wood interphase region is compared with the interface, adhesive interphase, and bulk adhesive regions. Pictured is a relatively thick adhesive layer; often there may be no significant bulk adhesive layer. Although interface properties are important, this figure shows that adhesive penetration into the wood could play a dominant role.

Flow of the adhesive to fill the surface micro-roughness is important for all bonding, but adhesive penetration into the substrate is not a significant issue in most bonding applications.

However, good penetration into the wood is a very important aspect of wood bonding. Standards such as ASTM D 2559 require bond formation within the minimum and maximum of the recommended open and closed assembly times [9]. Sufficient penetration into the wood is considered important for good bond formation, but overpenetration produces a starved bondline that is the weak link. Overpenetration does not occur with non-porous substrates; thus, different factors need to be considered in formulating and using wood adhesives. A lower viscosity adhesive is normally better for the wetting and adhesion, but for wood the adhesive can be so thin as to overpenetrate into the wood.

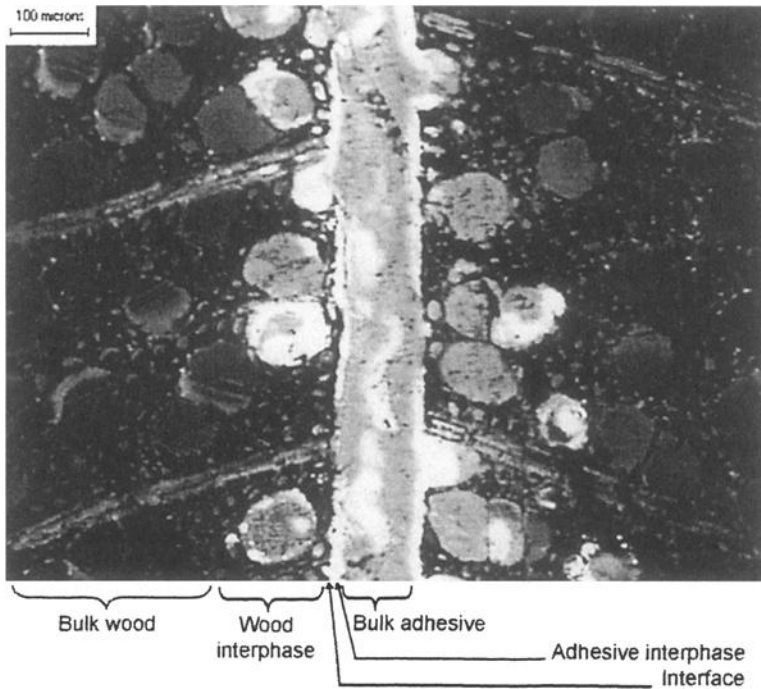


FIG. 1—Wood bondline of an epoxy adhesive using fluorescence microscopy to show regions of the bonded assembly.

Although penetration is a very important aspect in wood bonding, the relative importance between penetration into lumens and into cell walls is not normally discussed. For bonding, penetration into a lumen depends on the adhesive's contact angle on the wood surface and the bulk adhesive viscosity, whereas penetration into the cell walls depends upon molecular size of the adhesive components and may depend upon the water or solvent swelling of the wall structure. For performance testing, filling of the lumen is a mechanical interlock that provides additional mechanical strength, while penetration into the cell walls can change their mechanical strength and swelling ability [6,10]. The reduced swelling could have significant effect in reducing the stress concentration at the interface. In addition, penetration of adhesive into the wall changes a sharp wood-adhesive interaction into a more diffuse boundary layer. In Fig. 2, adhesive penetration into the micro-channels in the wood [11] could serve as a nano-mechanical

4 ADVANCES IN ADHESIVES, ADHESION SCIENCE, AND TESTING

interlock (interdigitation). Another model involves shallow adhesive penetration and crosslinking within the surface cell wall layer to form an adlayer. Deeper penetration and more crosslinking within the wall causes the formation of an interpenetrating polymer network [12], which of all these mechanisms, would most stabilize the wall towards dimensional changes. If the adhesive penetrates into the cell wall to form a bridge, then the role of primary and secondary chemical bonds at the adhesive-wood interface might be less important. Although numerous methods have shown that some adhesives penetrate the cell wall and change its physical properties [6], reports of data describing the effect on adhesive strength are very limited. It would be useful to determine if adhesives giving poor durability do not stabilize the cell wall, whereas those that have durability do provide stability to the cell wall.

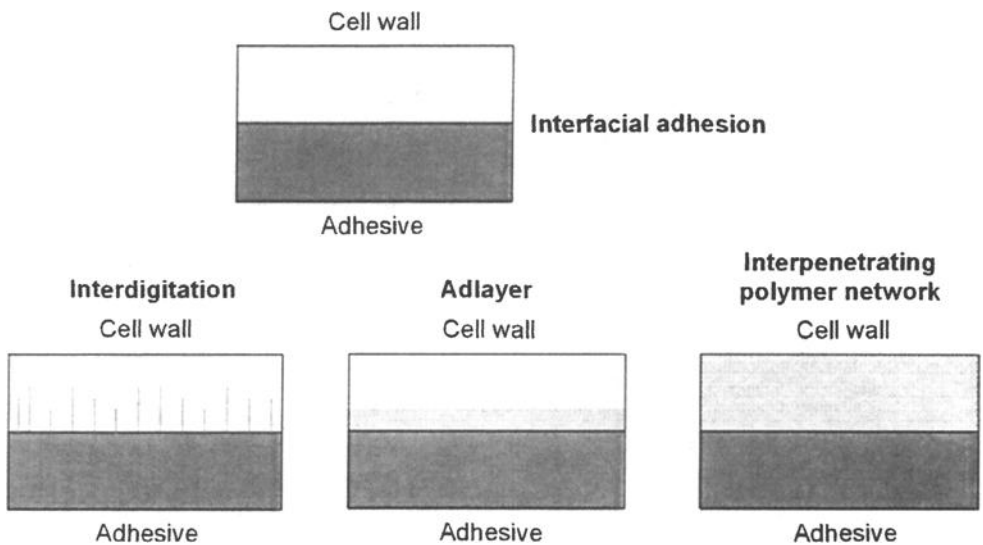


FIG. 2—Models to illustrate the difference between an interfacial bond and those involving adhesive penetration into the wood cell wall, including interdigitation, adlayer, and a fully interpenetrating polymer network.

Another difficulty in understanding wood bonding is that although much discussion focuses on primary and secondary bonds between the adhesive and the wood, the chemical composition of the surface layer is not clearly understood. Although cellulose is the main wood component, fracture is probably more likely in the hemicellulose and lignin layers because of their weaker mechanical strength. Prior work has indicated that hemicellulose is the main compound for hydrogen bonding on wood surfaces because of its greater accessibility [13]. On the other hand, lumen walls can be high in lignin content from the warty layer [14]. The planed wood surfaces in Figs. 3 and 4 do not show much evidence of cellulose fibrils on the surface but are more consistent with a material, like lignin, that can flow and create a smoother surface. Factors favoring lignin-rich over cellulose-rich surfaces include the following: it has been identified as the main component of the warty layers that exist on many lumen walls, it is the most likely to flow upon the friction and heat of planing, and it provides the lowest energy surface. Hemicellulose may also be present, but the cellulose is likely to be the least accessible.

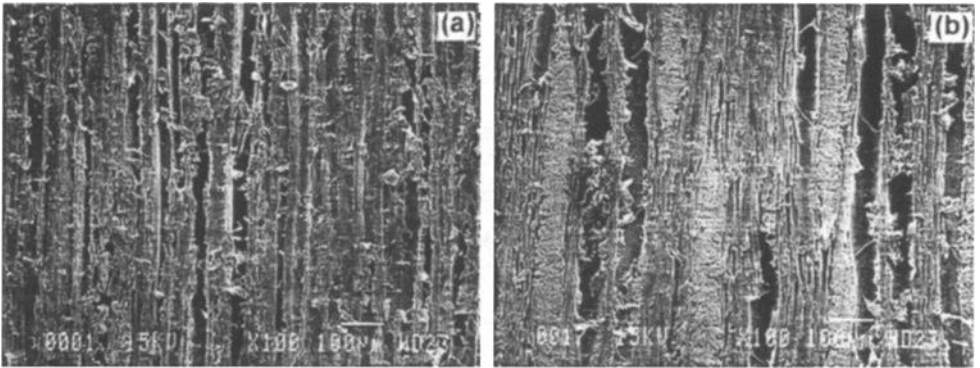


FIG. 3—Scanning electron micrographs of (a) the softwood southern yellow pine and (b) the hardwood hard maple to show the fragmented surface produced by planing.

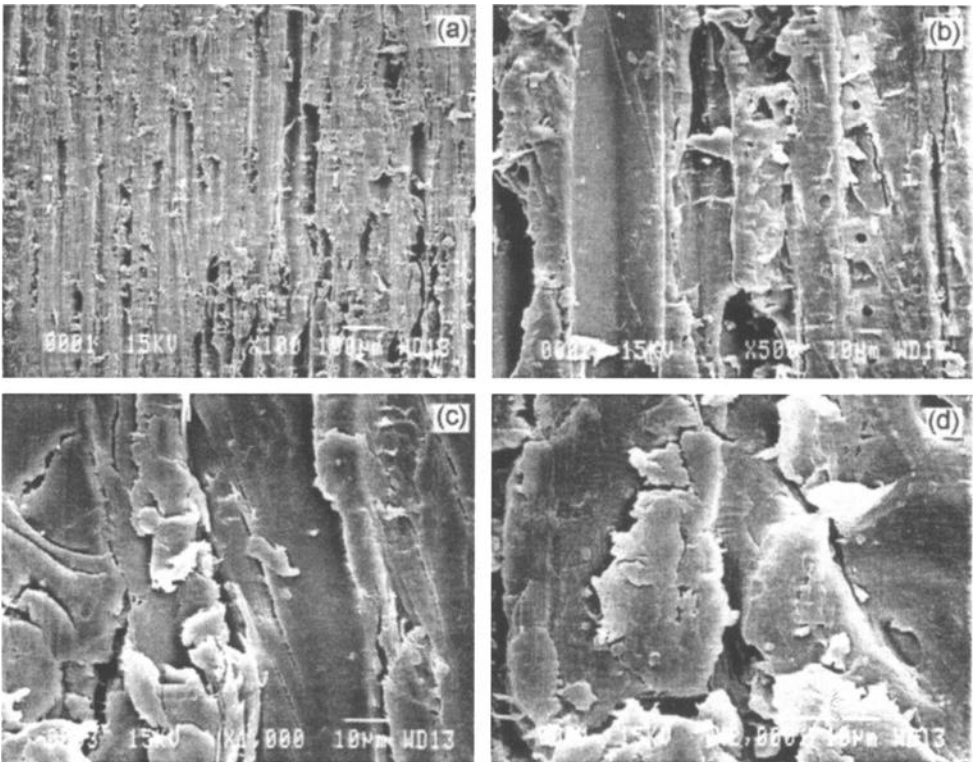


FIG. 4—Scanning electron micrographs of yellow poplar to show that the fragmented surface produced by planing is evidenced by examining under higher magnification.

Surface roughness is an important factor for all bonding applications because it often limits surface wetting. The surface roughness of wood, with its cellular structure, is orders of magnitude greater than that of surfaces present in most other adhesive applications. However, the surface is not the orderly structure normally pictured; rather it is much more fractured and irregular, as the examples of hard maple (hardwood) and southern yellow pine (softwood) in Fig. 3 illustrate. Even though sharp planer blades were used to prepare these surfaces, the surfaces are still very fractured and ragged. Obviously, fragments and covered ray ends on the wood surface can limit adhesive penetration into the wood and bonding to sound surfaces. The higher magnification of planed yellow poplar in Fig. 4 emphasizes the extensive shredding of surface cell walls. Although several articles have addressed the penetration issue [15,16,17], the effect of adhesive type and wood species on penetration is not well understood.

Understanding adhesive-wood cell interactions is more difficult because of the tremendous variability in wood cell types. With tracheid, parenchyma, and fiber cells, vessels, resin canals, and ray cells that vary in composition and structure in the earlywood, latewood, sapwood, and heartwood domains, there is a tremendous variety of bonding surfaces, each of which may interact differently with the adhesives. The most dramatic difference is often between wood species because of the large difference in cellular architecture. Bonding of different species often requires changes in adhesive formulation to control penetration into the wood. Although some work has been done on determining penetration into cell lumens and walls [6], this information is usually not related to the performance of the bonded assembly.

Many classes of adhesives are used in wood bonding because of different production and end-use conditions. Most adhesives can give acceptable wood bonds if the use conditions are not too strenuous or at high moisture levels. The interaction of a hot-melt adhesive with wood should be quite different from that of a water-borne adhesive, not only because of viscosity differences but also because of the lack of cell wall swelling by hot-melt adhesive. In addition, some adhesives penetrate and change the mechanical properties of cell walls [10,18], but it not known if all adhesives that penetrate cell walls change their mechanical properties.

Although many techniques have been used to examine how adhesives interact with wood [6], the observations generally have not been related to bond performance. Does penetration into lumens result in better strength, or is penetration into the cell walls more important, especially for durable exterior bonds?

Performance Testing

Adhesives are used to hold substrates together under the desired end use conditions. This means that a bond needs sufficient strength and durability to hold the substrates together under a defined set of conditions. Generally, strength and accelerated tests are used to establish the suitability of an adhesive for a specific application. The approval of an adhesive, especially for those applications that are more demanding upon the adhesive, are often quite specific for the bonding of a single wood species under specific conditions, as in ASTM D 2559 [9]. The durability of adhesives that pass these accelerated tests has been borne out by their performance in actual end use over many years. The question arises whether these accelerated aging tests are too conservative—some adhesives may not pass these tests but may actually be durable enough in the end use. The concern is that the tests involve rapid wetting and drying, not allowing stress to be dissipated through the stress relaxation of the wood. The validity of accelerated tests is always a difficult question, but for an accelerated test to be an accurate predictor, the mode of failure in both the accelerated test and end use must be the same. This implies that we need to

understand the forces exerted upon the bondline for both the accelerated tests and the end use conditions.

The question remains as to why some wood adhesive bonds are durable under exterior conditions and many are not. Most of the research has been on the adhesive chemistry, adhesive formulation, and testing durability; only limited resources have been applied toward understanding what contributes to durability. It is generally understood that for structural adhesives, the adhesive needs to have sufficient crosslinking to support creep resistance. However, why do only a few adhesives provide low delamination in the ASTM D 2559 test? The poor durability of urea-formaldehyde has been explained on the basis of depolymerization of the adhesive, but why does the addition of melamine to the urea-formaldehyde promote durability? Why is a phenol-formaldehyde adhesive more durable than an epoxy adhesive in wood bonding, given the durability of epoxies in metal bonding and coatings, cement coatings, and other applications?

For wood bonds, when failure is identified, it is usually divided only between wood and bondline failure. Bondline failure is often considered strictly a lack of adhesion because of the difficulty in determining the main failure location on the complex wood surfaces. Horioka has classified five locations for failure in going from the bulk wood to the bulk adhesive [5]. For epoxies, failure usually occurs in the bulk wood under dry conditions and often in the adhesive interphase region under wet conditions [19]. Why should there be significant failure in the epoxy interphase region under wet conditions? One explanation is that the epoxies are unable to withstand the strain during the expansion of the wood as it absorbs the water under soaking conditions, as in Fig. 5. Microscopic examination supports this concept in that the fracture lines are highly oriented in the longitudinal direction as expected from a swelling force (Fig. 6). Also supporting this concept is the increased wood failure in ASTM D 905 compressive shear tests when using epoxy-bonded acetylated wood with its low volume swelling compared with bonded unacetylated wood with its high swelling [20]. In another set of experiments, the effect of increased stress on the bondline from water soaking has been exhibited for FPL-1A epoxy bonding of several different wood species evaluated using ASTM D 905 tests. As expected, the percentage wood failure dramatically decreased in going from the dry tests to the vacuum-pressure water soaks in the shear test. Surprisingly, the percentage wood failure returned to its original values when the wet samples were allowed to dry in an 80°C, 65 % humidity room (Fig. 7). This indicates that increased bondline failure results from a combination of internal stress from the swelling of the wood and the applied load, but removal of the internal stresses upon drying causes recovery of much of the bondline strength. This cell wall stabilization model has also been used to explain the ability of hydroxymethylated resorcinol primer to reduce the delamination of epoxy adhesives in the D 2559 test [21].

Understanding where failure occurs has often been difficult with wood adhesives because of problems with visualization of colorless adhesives, such as epoxies. Fluorescence microscopy can be one way to learn where and why failure is occurring. This can be done by looking down onto the failure surface (Fig. 8) or in the cross-section (Fig. 9).

How to determine sufficient durability of wood bonds is still of great concern. ASTM D 2559 has been considered the ultimate test, but there has been little discussion of forces on the bondline during this test and how representative they are of those experienced in the actual application. The test involves cycles of rapid water soaking by vacuum-pressure soaks followed by rapid drying in a hot oven. Not surprisingly, this test causes considerable distortion and fracturing of the wood itself because the dimensional changes are so rapid that the wood does not

have a chance to stress relax. The bondline needs to deal not only with shear, tension, and compressive forces in the radial direction but also with the distortion of the wood and normal tension forces. Can these results be correlated to ASTM D 905 tests that involve shear tension forces from the wood swelling in the radial direction and compressive shear forces in the longitudinal direction as has been claimed [22]? How do these tests compare to laminated beam applications where bondlines are under tension at the bottom of the beam and compression at the top as the wood is more gradually swelling and shrinking? This is not to imply that ASTM D 2559 does not have utility, but we do not have the scientific understanding to know if it is excessively conservative (useful adhesives being unable to pass this test) or too liberal (adhesives not being under external forces during the swelling and shrinking).

Despite the success of many adhesives in a variety of applications, other challenges still exist with wood adhesives. How can we get equal performance out of a lower cost adhesive? As the wood supply changes from old growth wood to more juvenile wood, how do we develop the proper adhesives, and how do we address performance standards when the wood itself is weaker?

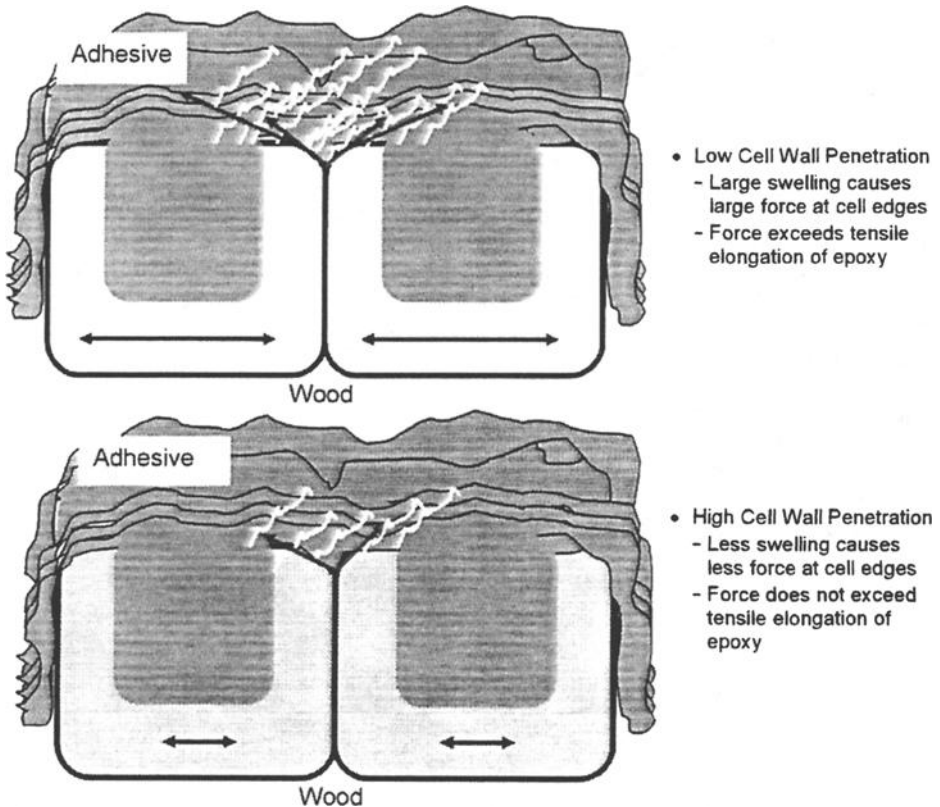


FIG. 5—Drawing to illustrate the difference in force upon the adhesive interphase region between cells with high and low swelling.

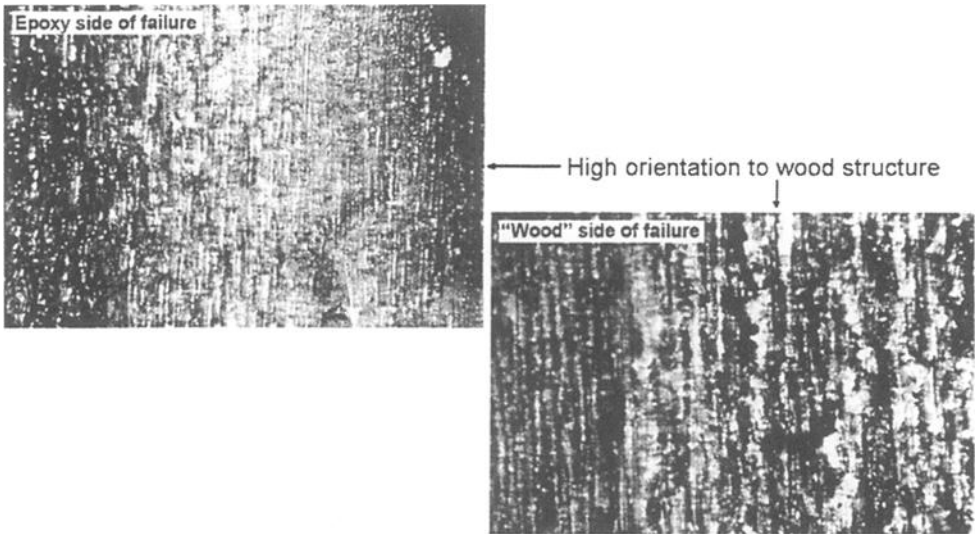


FIG. 6—Fracture surface produced under ASTM D 2559 to show the high orientation parallel to the wood orientation even though fracture is mainly in the epoxy interphase region.

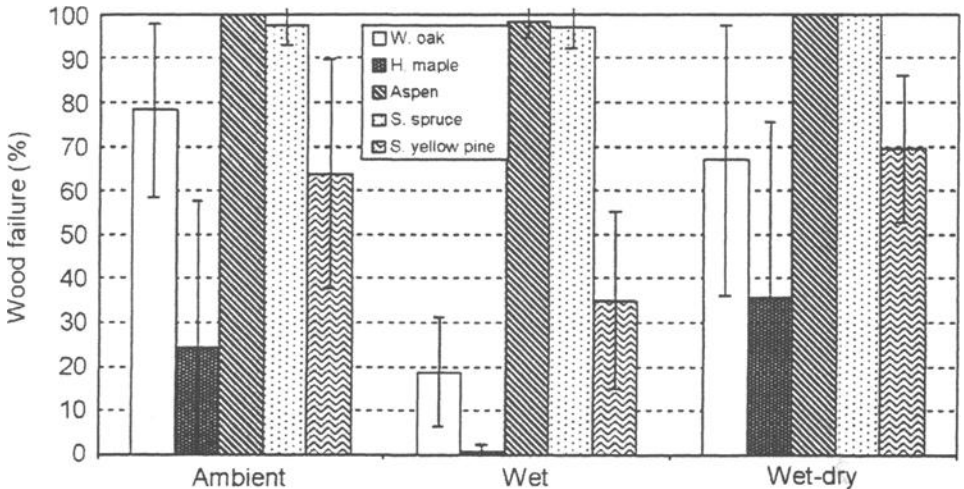


FIG. 7—Percentage wood failure of five wood species bonded with FPL 1-A epoxy using ASTM D 905 to show loss of bondline strength from vacuum-pressure water soak and recovery upon redrying.

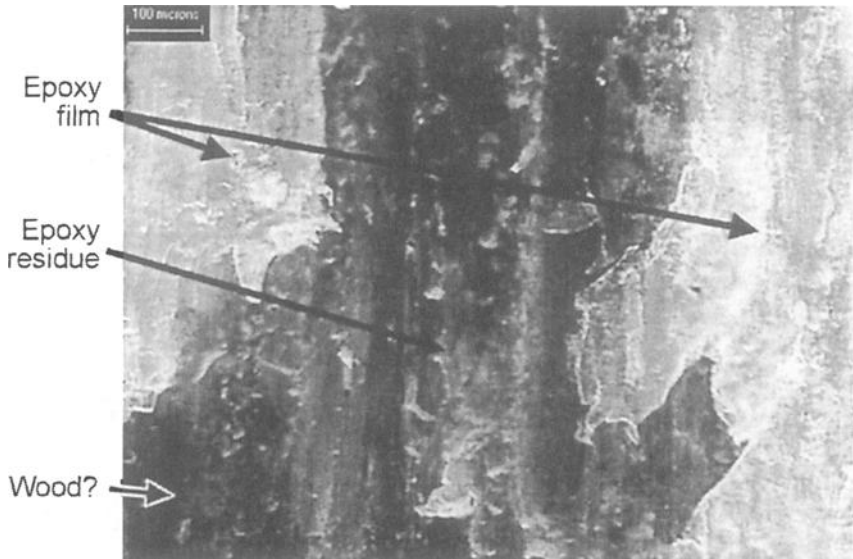


FIG. 8—Use of fluorescence microscopy to show the failure location of epoxy-bonded yellow poplar after vacuum-pressure water soak.

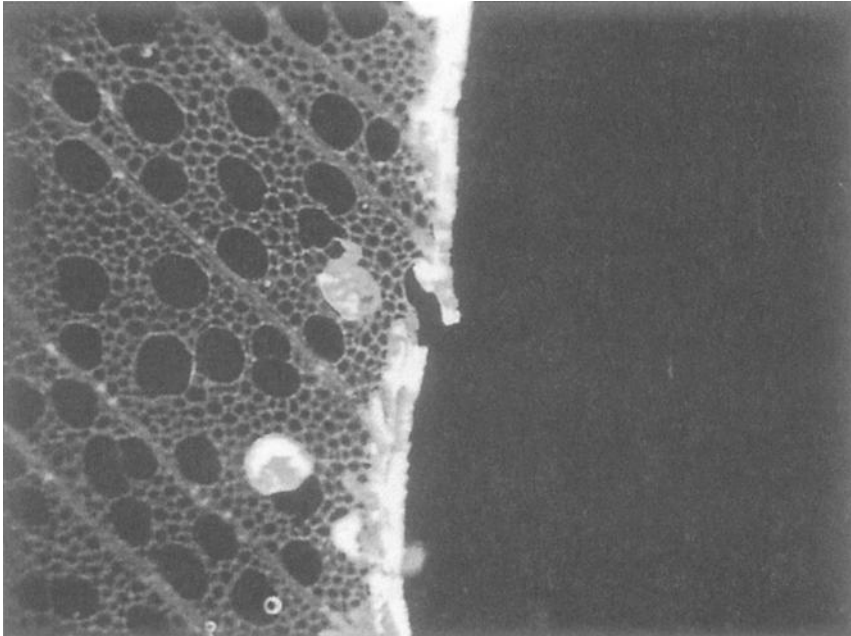


FIG. 9—Use of fluorescence microscopy on a cross-section to show failure of yellow poplar bonded with epoxy adhesive after vacuum-pressure water soak.

Conclusions

Adhesives provide good wood bonds for a wide variety of applications. Knowledge of adhesive chemistry, adhesive formulation, and adhesive-wood interactions has increased dramatically. Understanding the location and cause of bondline failure has lagged behind. To understand bonding and performance testing processes, more emphasis needs to be placed upon

- understanding the location of bondline failures using the Horioka model,
- determining the internal and external forces causing bondline failures,
- relating strength factors to the bonding process, and
- knowing the morphology and chemistry of the wood bonding surface better.

By applying existing and newly developed techniques to the study of specific adhesives, a much better knowledge of factors leading to durable bonds can be obtained. It is important to use analysis techniques in concert and to apply them to samples evaluated by the standard adhesive performance evaluation methods.

By using these processes, we have made progress toward understanding why normally durable adhesives, such as epoxies, are not as durable in bonds with wood. The stabilization of the surface cell wall toward expansion and contraction seems to play an important role in minimizing the stress concentration in the interphase region. Although this mechanism is not definitively proven, it is consistent with the data on unmodified wood, acetylated wood, and wood primed with hydroxymethylated resorcinol.

Acknowledgments

I thank Al Christiansen of the Forest Products Laboratory and Chip Frazier of the Wood Based Composite Center at Virginia Tech for their comments on wood adhesive bond formation and failure mechanisms. The experimental work reported in this paper was carried out by Rishawn Brandon, Jermal Chandler, and Daniel Yelle of the Forest Products Laboratory, with fluorescence microscopy assistance from Fred Kamke of the Wood Based Composite Center at Virginia Tech.

References

- [1] Frihart, C. R., "Adhesives Interaction with Wood," *Fundamentals of Composite Processing. Proceedings of a Workshop*, U.S. Department of Agriculture, Forest Service, Forest Products Laboratory, J. E. Winandy and F.A. Kamke, Eds., Madison, WI, 2004, pp. 29–38.
- [2] Pizzi, A. J. and Mittal, K., *Handbook of Adhesives Technology*, 2nd ed., Marcel Dekker, New York, 2003.
- [3] River, B. H., Vick C. B., and Gillespie, R. H., "Wood as an Adherend," *Treatise on Adhesion and Adhesives*, Vol. 7, Marcel Dekker, J. D. Minford, Ed., New York, 1991, 230 pp.
- [4] River, B. H., "Fracture of Adhesively-Bonded Wood Joints," *Handbook of Adhesive Technology*, Marcel Dekker, A. Pizzi and K.L. Mittal, Eds., New York, 2003, pp. 325–350.
- [5] Horioka, K. and Gamoh, M., "The Mechanism and Durability of Adhesion in Wood-Glue Bonds," *Proceedings of the Symposium, IUFRO-5 Meeting*, 1973, pp. 508–527.
- [6] Frihart, C. R., "Wood Structure and Adhesive Strength," *Characterization of the Cellulosic Cell Wall - The Proceedings of the SWST International Workshop on the Assessment and Impact of the Cellulosic Cell Wall*, Blackwell Publishing, L. H. Goom and D. Stokke, Eds.,

- Oxford, UK, 2005.
- [7] ASTM Standard D 905-04, "Standard Test Method for Strength Properties of Adhesive Bonds in Shear by Compression Loading," *Annual Book of ASTM Standards*, ASTM International, West Conshohocken, PA, 2004.
- [8] Vick, C. B., Richter, K. H., and River, B. H., "Hydroxymethylated Coupling Agent and Method for Bonding Wood," U. S. Patent 5,543, 487, 1996.
- [9] ASTM Standard D 2559-00, "Standard Specification for Structural Laminated Wood Products for Use under Exterior (Wet Use) Exposure Conditions," *Annual Book of ASTM Standards*, ASTM International, West Conshohocken, PA, 2000.
- [10] Gindl, W. and Gupta, H. S., "Cell-Wall Hardness and Young's Modulus of Melamine-Modified Spruce Wood by Nano-Indentation," *Composites Part A: Applied Science and Manufacturing*, Vol. 33, 2002, pp. 1141-1145.
- [11] Tarkow, H., Feist, W. C., and Sutherland, C., "Interpenetration of Wood and Polymeric Materials. II: Penetration Versus Molecular Size," *Forest Prod. J.*, Vol. 16, No. 10, 1966, pp. 61-65.
- [12] Frazier, C. E. and Ni, J., "On the Occurrence of Interpenetration in the Wood-Isocyanate Adhesive Interphase," *Int. J. Adhesion and Adhesives*, Vol. 18, 1998, pp. 81-87.
- [13] Salehuddin, A., "Unifying Physico-Chemical Theory for Cellulose and Wood and Its Application for Gluing," Ph.D. Thesis, North Carolina State University at Raleigh, 1970.
- [14] Baird, W. M., et al. "Development and Composition of the Warty Layer in Balsam Fir," *Wood and Fiber Science*, Vol. 6, No. 3, 1974, pp. 211-222.
- [15] Johnson, S. E. and Kamke, F. A., "Quantitative Analysis of Gross Adhesive Penetration in Wood Using Fluorescence Microscopy," *J. Adhesion*, Vol. 40, 1992, pp. 47-61.
- [16] Kitazawa, G., "A Study of Adhesion in the Glue Lines of Twenty-Two Woods of the United States," M.S. Thesis, The New York State College of Forestry at Syracuse University, 1946.
- [17] Nearn, W. T., "Application of the Ultrastructure Concept in Industrial Wood Products Research," *Wood Science*, Vol. 6, No. 3, 1974, pp. 285-293.
- [18] Gindl, W., Muller, U., and Teischinger, A., "Transverse Compression Strength and Fracture of Spruce Wood Modified by Melamine-Formaldehyde Impregnation of Cell Walls," *Wood and Fiber Science*, Vol. 35, No. 2, 2003, pp. 239-246.
- [19] Frihart, C. R., "Durable Wood Bonding with Epoxy Adhesives," *Proceedings 26th Annual Meeting of the Adhesion Society*, The Adhesion Society, Blacksburg, VA, 2003, pp. 476-478.
- [20] Frihart, C. R., Brandon, R., and Ibach, R. E., "Selectivity of Bonding for Modified Wood," *Proceedings 27th Annual Meeting of The Adhesion Society, Inc.*, The Adhesion Society, Inc., Blacksburg, VA, 2004, pp. 329-331.
- [21] Christiansen, A. W., "Exploring Adhesive-Wood Bond Durability by Studying the Effects of Chemical Structure and Reactivity Changes to HMR Primer," *Biographies and Abstracts of the Forest Products Society 58th Annual Meeting*, Forest Products Society, Madison, WI, 2004, p. 37, <http://www.forestprod.org/confpast.html>.
- [22] Marcinko, J. J., Parker, A. A., and DiPietrantonio, B., "Block Shear Analysis, Viscoelastic Behavior, and Structural Adhesive Development," *Biographies and Abstracts of the Forest Products Society 57th Annual Meeting*, Forest Products Society, Madison, WI, 2003, p.21, <http://www.forestprod.org/confpast.html>.

David J. Moonay, Ph.D.,¹ Robert G. McGregor,² and Robert A. Mastria, Jr.³

A New Low Cost Method For Measuring the Viscoelastic Behavior of Adhesives

ABSTRACT: A rotational benchtop Rheometer with vane spindles can be used to measure the static yield stress behavior of materials. By running at different rotational speeds, the Rheometer data can be equated with the viscoelastic information determined by an oscillating rheometer. The rotational Rheometer offers a less expensive method suitable for Quality Control needs.

KEYWORDS: yield stress, viscoelastic, rotational rheometer

Introduction

A standard rotational benchtop Rheometer (see Fig. 1) is a relatively inexpensive instrument that can be used with Vane Spindle geometry (see Fig. 2) to determine the yield stress of viscoelastic materials. The instrument is similar to a standard rotational viscometer in the sense that the torque response is based on the degree of a spring windup. Therefore, deviations from an ideal elastic response may be attributed to viscous dissipation. The ratio of energy dissipated to the energy stored by the calibrated spring in the instrument can be used to calculate a phase angle and other viscoelastic properties in the material. Such viscoelastic properties are currently determined by significantly more expensive instrumentation.

Based upon work done within the food industry [1], a similar line of investigation into adhesive materials could produce similar results. In brief, measurements were made with air-bearing oscillating rheometers over a frequency range of 0.001–0.01 Hz to characterize the viscoelastic properties of ketchup, mayonnaise, and other food-related materials at room temperature. A Brookfield YR-1 Rheometer was used to collect data for the same materials over a similar frequency range. Frequency, in the case of the YR-1 Rheometer, is determined by the rotational speed at which the YR-1 motor is rotated. By considering the energy stored and lost through the spring, a phase angle is calculated. This information, coupled with a "Brookfield complex modulus" or "B*" determined from the linear region of the failure curve, is used to compute values that may correlate with the conventional storage and loss moduli [1]. We designate the storage and loss moduli calculated by our method as "B'" and "B", respectively.

Results from the food testing show that the Brookfield YR-1 Rheometer may provide correlation with an oscillating rheometer [1]. Therefore, we suggest that a standard benchtop Rheometer with vane spindle may be used for reliable collection of fundamental viscoelastic data of adhesive materials as well.

Manuscript received 1 October 2004; accepted for publication 11 March 2005; published October 2005.

Presented at ASTM Symposium on Advances in Adhesives, Adhesion Science, and Testing on 4-6 October 2004 in Washington, DC.

¹ Sales Engineering - Rheology Laboratory Supervisor, Brookfield Engineering Laboratories, Inc., 11 Commerce Boulevard, Middleboro, MA 02346.

² National Sales and Marketing Manager - Brookfield Engineering Laboratories, Inc., 11 Commerce Boulevard, Middleboro, MA 02346.

³ Brookfield 2004 Summer Intern; Undergraduate Student, University of Massachusetts at Amherst.



FIG. 1—*Rheometer with vane spindle for measuring yield stress (Brookfield YR-1).*

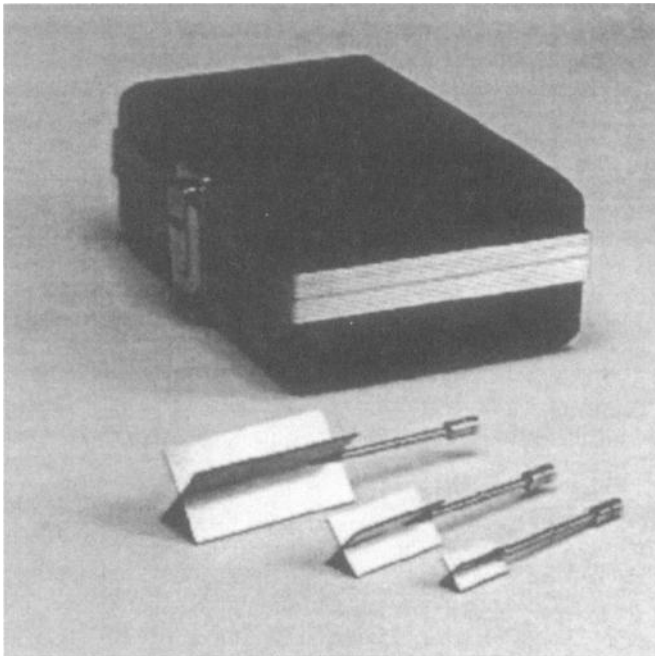


FIG. 2—*Set of vane spindles (Brookfield).*

Yield Stress⁴

The yield stress is an important physical property used to characterize the behavior of liquids and semi-solid materials, such as pastes. The associated parameters are the yield stress and yield strain. The yield stress is the critical shear stress, applied to the sample, at which the material begins to flow as a liquid. The yield strain is the deformation, resulting from the applied stress, at which the flow starts [2,3].

Many materials are designed to have a yield stress value, so that the behavior of the product satisfies a specific customer need. Ketchup, for example, must flow out of a bottle when shaken or squeezed, but then solidify on the targeted food, such as french fries. Shaking or squeezing the bottle stresses the ketchup so that it flows; after the ketchup settles on the fries, its structure rebuilds so that the ketchup “sits” in place rather than flowing off the fries like water. Puddings have yield stress values as well. The “body” of the pudding appeals to consumers - it is solid at rest, yet it’s easily spooned out of its cup, and it is easy to eat. Thus, the yield behavior of selected foods contributes to the food texture that we like.

Many water-based paints have low yield stresses. Latex house paints, for example, are easily stirred or poured. Brushing or spraying provides enough stress so that the paint flows easily and smoothly over a painted wall. However, a thin layer of applied paint (if a good one!), allowed to rest undisturbed on the surface, regains its structure quickly so that there is neither unsightly “dripping” afterwards nor rippled brush marks. The smooth appearance of the painted surface is very appealing to the homeowner.

Adhesives can vary from low viscosity to high viscosity, depending on formulation and application. Thicker adhesives used for floor tiling are stiff when first put onto a trowel but spread easily over the floor. This ease of application is important to the user, although the quality of the adhesive is possibly judged more by its “stiffness,” which relates to yield stress value.

The Brookfield YR-1 Rheometer⁴

The operating principle of the YR-1 Rheometer is to drive a spindle through a calibrated spiral spring connected to a motor drive shaft (see Fig. 3). The vane spindle is immersed in the test material. The resistance of the material to movement is measured by observing increasing torque values as the YR-1 motor rotates. The amount of shaft rotation is measured by the deflection of the calibrated spiral spring inside the instrument. Spring deflection is measured with a rotary transducer.

If the vane spindle did not move at all, the data would look like the graph in Fig. 4. The data often look like the graph in Fig. 5 because there is usually some deformation of the test material due to the increasing force imparted by the vane spindle. The maximum torque value is the yield stress. The straight line in Fig. 5 is a repeat of what was shown in Fig. 4. An algorithm in the YR-1 firmware converts the maximum torque value into a yield stress value.

The shear stress measurement range of the YR-1 (in Pascals) is determined by the size and shape of the vane spindle and the full scale torque range of the calibrated spring.

There are four basic spring torque series offered by Brookfield, as shown in Table 1.

⁴ Much of the information in this section is taken from the Brookfield YR-1 Operating Instructions Manual, Brookfield Engineering Laboratories, Inc., Middleboro, MA 02346.

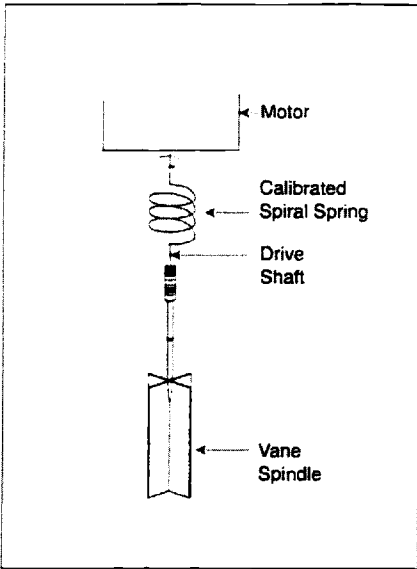


FIG. 3—Principle of operation for Brookfield YR-1 Rheometer.

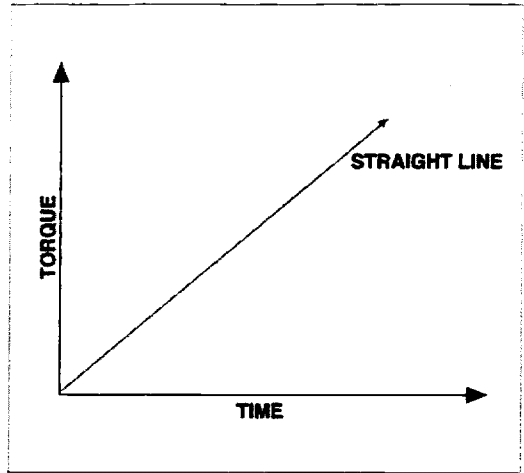


FIG. 4—Torque versus time graph for test with YR-1 Rheometer where there is no spindle movement.

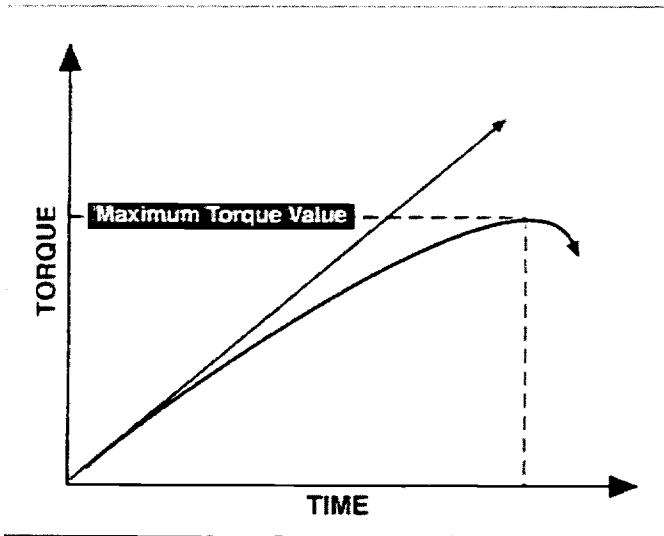


FIG. 5—Typical graph for test with YR-1 Rheometer.

TABLE 1—Torque measurement ranges for Brookfield YR-1 Rheometer.

| Model | Dyne-cm | Milli-Newton - m |
|-----------|---------|------------------|
| 1/4RVYR-1 | 1,796 | 0.1796 |
| RVYR-1 | 7,187 | 0.7187 |
| HBYR-1 | 57,496 | 5.7496 |
| 5XHBYR-1 | 287,480 | 28.7480 |

The shear stress measurement range for the three standard vane spindles shown in Fig. 2 at each spring torque is shown in Table 2.

TABLE 2—Shear stress ranges for Brookfield YR-1 Rheometer.

| Spindle | Torque Range | Shear Stress Range (Pa) |
|---------|--------------|-------------------------|
| V-71 | 1/4RV | 125-1.25 |
| V-72 | 1/4RV | .5-5 |
| V-73 | 1/4RV | 2.5-25 |
| V-71 | RV | .5-5 |
| V-72 | RV | 2-20 |
| V-73 | RV | 10-100 |
| V-71 | 1HB | 4-40 |
| V-72 | 1HB | 16-160 |
| V-73 | 1HB | 80-800 |
| V-71 | 5XHB | 20-200 |
| V-72 | 5XHB | 80-800 |
| V-73 | 5XHB | 400-4000 |

EZ-Yield™ Software For The YR-1 Rheometer⁵

Brookfield EZ-Yield™ Software is a 32-bit Windows program supplied with every YR-1 Yield Rheometer. EZ-Yield™ allows the user to easily create a yield test program and download it to one of ten memory locations in the YR-1 Rheometer. These programs are retained in memory so that the YR-1 can be disconnected from the PC and used in remote locations (e.g., in a Q.C. laboratory, the production floor, etc.). EZ-Yield collects all of the data from a yield test, in addition to the final Yield Stress value. These data can be saved, printed, and graphed using the software.

Figure 6 shows the main screen in EZ-Yield, which is used to create test programs. Brief descriptions of each parameter follow.

The program number is the number of the memory slot in the YR-1 Rheometer to which the test parameters will be loaded. There are ten slots, numbered from 0-9.

A program name, such as "Adhesive 1," is decided by the user and is loaded into the memory slot in the YR-1 Rheometer with the test parameters.

The spindle entry is a two-digit code representing the vane spindle number used for the test. Each vane spindle has two immersion marks as shown in Fig. 7. Normally, the spindle is inserted so that the sample reaches this mark. If the sample container is too small, the secondary immersion mark may be used.

Pre-shear (RPM) is an optional procedure for shearing of sample before measuring its yield properties. It is particularly useful if the user wants to eliminate previous shear history (e.g., bumping, transferring) of the sample before testing and to observe the structural rebuilding of the sample.

⁵ Much of the information in this section is taken from the Brookfield YR-1 Operating Instructions Manual, Brookfield Engineering Laboratories, Inc., Middleboro, MA 02346.

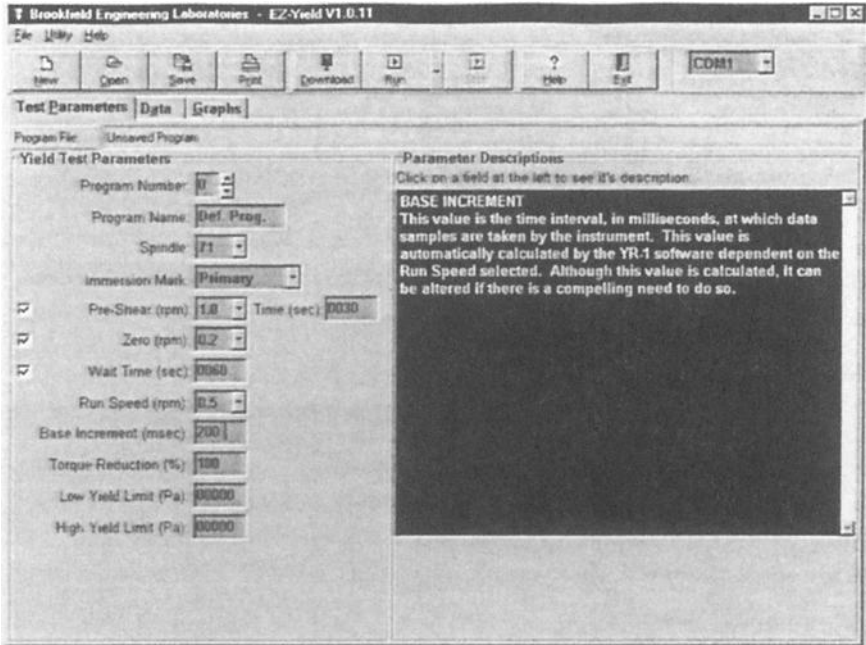


FIG. 6—Main screen for test parameters in EZ-Yield software.

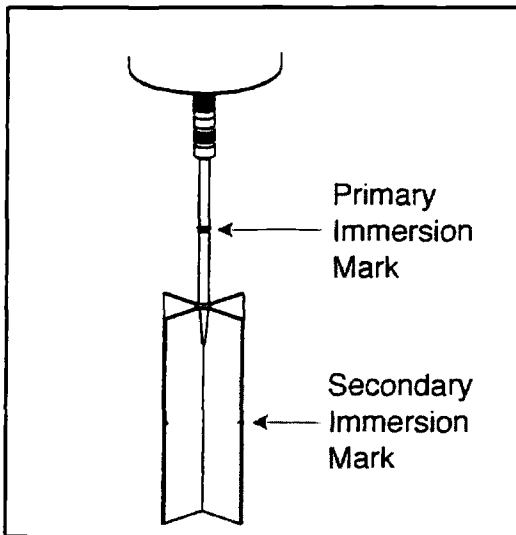


FIG. 7—Vane spindle immersion marks.

An optional, but highly recommended, torque zero step can be included in the test parameters. This may be necessary because the spindle sometimes twists a small amount during insertion into the sample. Zeroing is an essential step after pre-shearing.

An optional Wait Time can be included in the test parameters. This is the time the sample is allowed to rest between the completion of zeroing and the start of the yield measurement.

Run Speed is the motor speed for the YR-1 at which the material is tested. Choices range from 0.01–5.0 rpm. It is common for materials to appear stiffer when tested at higher speeds. That is, the slope of the torque-versus-time or stress-versus-strain curve increases with increasing speed. This is because the material structure has less time in which to react to dissipate the applied stress. Increasing the speed will, in most cases, increase the yield stress measured by the instrument. Most yield tests are conducted at relatively low speeds (<1 rpm) to minimize any inertial effects when using vane spindles.

Base Increment is the amount of time in milliseconds between data points used for taking torque (stress) readings. The software automatically calculates base increment values. Smaller base increment values are used during faster speed tests to ensure that data are taken fast enough to properly determine the yield stress value. Larger base increment values are used during slower speed tests because these tests are expected to take longer; the longer time interval between data points helps prevent typical data files from becoming very large. However, the user may still wish to set this value to suit the required need after some familiarity is gained with the material being tested.

Torque Reduction is the reduction in torque, occurring at the defined yield point, based on comparison to a rigid (solid) sample. That is, the material yields or begins to break down and, as a result, the measured incremental torque begins to decrease. A value of 100 % for this parameter causes the test to stop as soon as there are no torque increases during a base time increment. Some users may wish to see a drop in torque after the yield point. Setting this parameter to values greater than 100 % allows data to be collected after the yield point by the EZ-Yield™ software so the decrease in torque may be more easily visualized.

Low and high yield limits can be used as a Quality Control tool. If the resulting yield stress from a test falls outside these limits, an appropriate message is displayed and printed with the results.

Experimental Method

The test equipment included:

- Brookfield YR-1 Rheometer, HB Torque Range
- V-72 Vane Spindle
- EZ-Yield Software

Two materials were found to be suitable candidates for adhesives testing:

- DAP Gel Formula Contact Cement
- Henry Premium Multipurpose Carpet and Sheet Vinyl Adhesive

The test procedure involved using a Brookfield HB YR-1 yield rheometer with a V-72 vane spindle at the secondary immersion mark. The materials were tested in the container they came

in at speeds of 0.05 and 0.5 rpm. After a test was run, the can was rotated and the spindle immersed in fresh, untested material. Four separate test runs were made in each sample at 0.05 rpm and then again at 0.5 rpm. The materials were thoroughly stirred, as recommended by instructions on each container, before they were tested. Samples were tested at room temperature, approximately 22°C. A typical test run at 0.05 rpm, for the DAP Cement, took approximately 3–3.5 min. One 0.5 rpm run took approximately 1 min. Each Henry adhesive test run typically took about 2.5 min at 0.05 rpm and 30 s at 0.5 rpm.

The data were collected by Brookfield EZ-Yield software as shown in Figs. 8 and 9. The test parameters were as follows: Spindle – 72, Immersion – Secondary, Zero Speed – 0.1 rpm, Wait Time – 30 s, Run Speeds – 0.05/0.5 rpm. The tests were carried out to either 105 % or 100 % torque reduction. Those tests carried out to 105 % torque reduction were trimmed down to include only those data points leading to and including the peak value of measured shear stress. The test data were exported as a Microsoft® Excel™ spreadsheet. The data from the spreadsheet were then copied into a template developed by David Moonay to calculate the viscoelastic properties of the material.

Data Analysis

The ratio of energy dissipated to energy stored during the YR-1 test was calculated and used to determine a phase angle δ_B . Dissipated (A'') and stored (A') energies as shown in Fig. 10 were determined by calculating areas underneath the curve generated during the YR-1 test run.

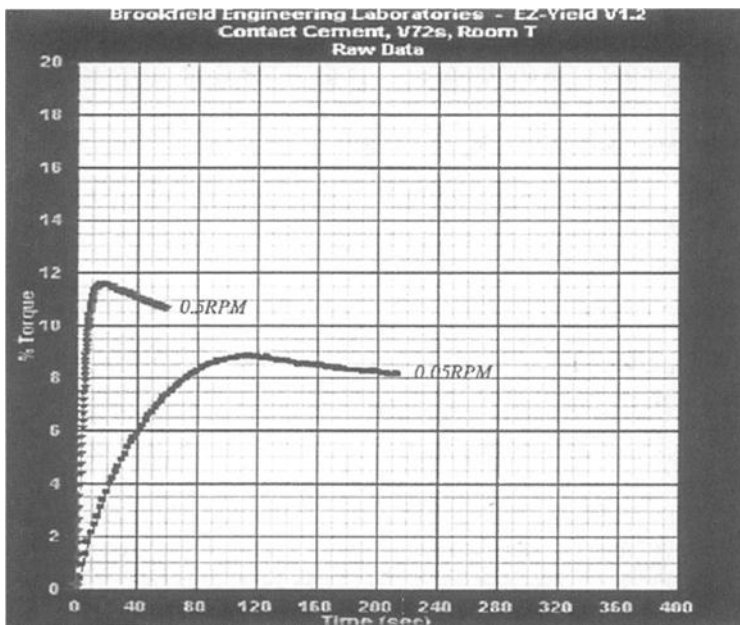


FIG. 8—Torque versus time data using Brookfield YR-1 Rheometer to test DAP gel formula contact cement.

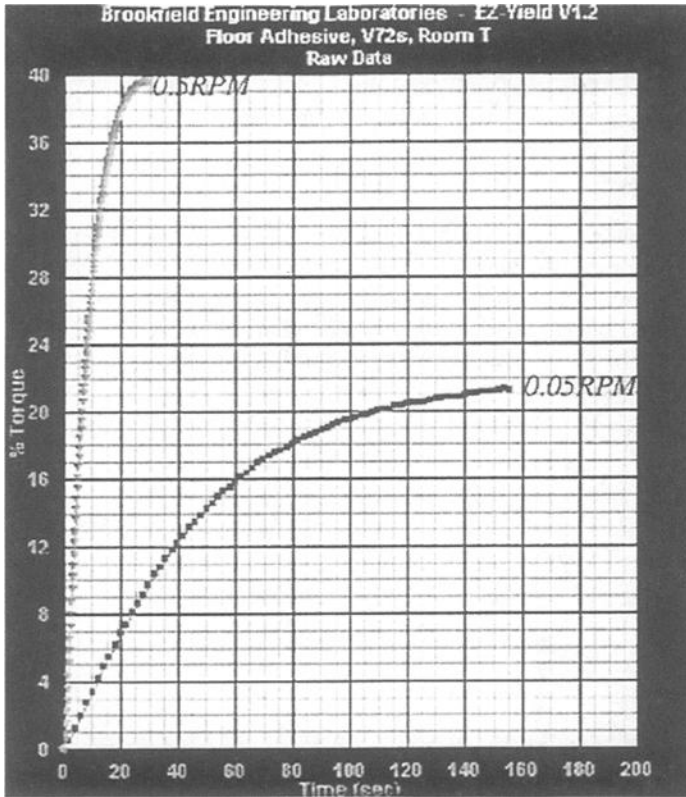


FIG. 9—Torque versus time data using Brookfield YR-1 Rheometer to test Henry premium multi-purpose carpet and sheet vinyl adhesive.

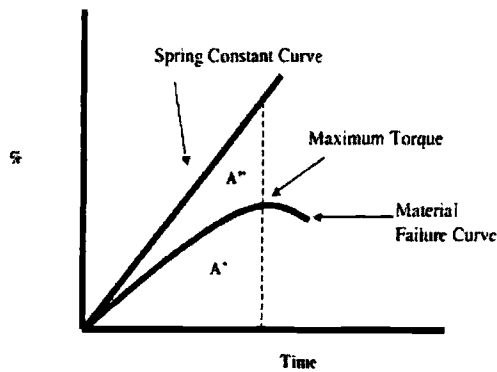


FIG. 10—Illustration of dissipated and stored energies from a YR-1 test using areas A'' and A' , respectively, in the graph.

The spring calibration line was linearly fit. The area A' and A'' were calculated by integrating the spring line and the viscoelastic material's data separately. Both the "Trapezoidal Rule" and "Simpson's Rule" methods were used [4]. Areas calculated by the two methods for given parameters typically agreed to better than 1 %.

The following equation was used to determine phase angle:

$$\delta_B = \tan^{-1}(A''/A')$$

The determination of "Brookfield Complex Modulus" (B^*), "Brookfield Storage Modulus" (B'), and "Brookfield Loss Modulus (B'')" proceeded as follows: Torque (%) and Time (s) values from the YR-1 data were converted to Stress (Pa) and Apparent strain (γ_A) values, respectively, using Brookfield's EZ-Yield software. B^* was determined as the slope from the linear region of the failure curve in Fig. 11; B^* was calculated by selecting the seven points that had the highest changes in torque and performing a linear regression using those points according to the theory of experimental work conducted at North Carolina State University [1]. B' and B'' were subsequently calculated using the following equations:

$$B' = B^* \cos \delta_B$$

$$B'' = B^* \sin \delta_B$$

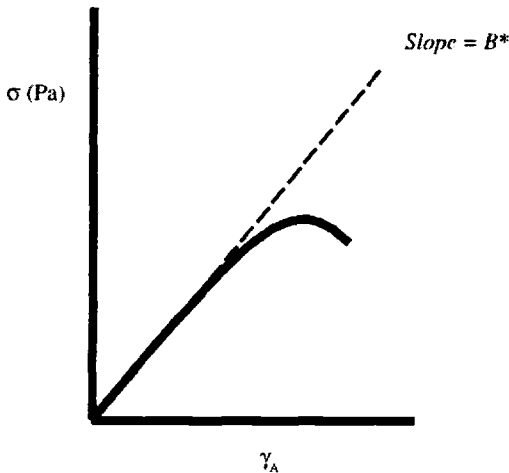


FIG. 11—Graphical illustration of method for determining "Brookfield Complex Modulus," B^* .

Results and Discussion

The results of the calculations performed on the data for the contact cement and floor adhesive are displayed below in Tables 3 and 4.

In both cases, B^* increases noticeably between the low speed test and the higher speed test. The conclusion is that this method can produce information that gives a quick, decisive indication of the viscoelastic response of the two different adhesives.

TABLE 3—Results of DAP contact cement tests.

| Contact Cement V 72 secondary | Tested in Can Stirred before test | | | Test Performed 8/26/04 | |
|----------------------------------|--------------------------------------|-----------|------------|---------------------------|----------------------|
| 0.05 rpm | B* | B' | B'' | Frequency (Hz) | Delta (Trap.) |
| Trial 1 | 198.97 | 57.06 | 190.62 | 0.0008333 | 1.280 |
| Trial 2 | 188.38 | 58.84 | 178.96 | 0.0008333 | 1.253 |
| Trial 3 | 189.17 | 53.58 | 181.42 | 0.0008333 | 1.284 |
| Trial 4 | 208.88 | 66.10 | 198.14 | 0.0008333 | 1.249 |
| Average | 196.35 | 58.90 | 187.29 | | 1.267 |
| 0.5 rpm | B* | B' | B'' | Frequency (Hz) | Delta (Trap.) |
| Trial 1 | 218.42 | 53.25 | 211.83 | 0.0083333 | 1.325 |
| Trial 2 | 265.95 | 78.66 | 254.06 | 0.0083333 | 1.271 |
| Trial 3 | 277.12 | 75.43 | 266.65 | 0.0083333 | 1.295 |
| Trial 4 | 215.59 | 39.29 | 211.98 | 0.0083333 | 1.388 |
| Average | 244.27 | 61.66 | 236.13 | | 1.320 |

TABLE 4—Results of Henry adhesive tests.

| | | | | | |
|----------------|-----------|-----------|------------|-----------------------|----------------------|
| 0.05 rpm | B* | B' | B'' | Frequency (Hz) | Delta (Trap.) |
| Trial 1 | 937.16 | 643.20 | 681.59 | 0.0008333 | 0.814 |
| Trial 2 | 1049.50 | 649.77 | 824.17 | 0.0008333 | 0.903 |
| Trial 3 | 989.65 | 613.31 | 776.70 | 0.0008333 | 0.902 |
| Trial 4 | 968.02 | 652.12 | 715.40 | 0.0008333 | 0.832 |
| Average | 986.08 | 639.60 | 749.46 | 0.0008333 | 0.863 |
| 0.5 rpm | B* | B' | B'' | Frequency (Hz) | Delta (Trap.) |
| Trial 1 | 1343.16 | 874.86 | 1019.17 | 0.0083333 | 0.861 |
| Trial 2 | 1251.33 | 774.69 | 982.69 | 0.0083333 | 0.903 |
| Trial 3 | 1252.66 | 845.13 | 924.61 | 0.0083333 | 0.830 |
| Trial 4 | 1244.74 | 791.69 | 960.52 | 0.0083333 | 0.881 |
| Average | 1272.97 | 821.59 | 971.75 | 0.0083333 | 0.869 |

Conclusion

The purpose of this work was to determine if useful viscoelastic information could be determined for Quality Control/Quality Assurance by using data obtained from a standard rotational Rheometer with vane spindle geometry. The difference between the purely elastic spring response of the Brookfield YR-1 Rheometer and the sample's measured behavior does, in fact, provide information regarding the sample's viscoelastic nature. Our work is based upon preliminary theoretical and experimental work of Dr. Christopher Daubert's group at North Carolina State University, where they are investigating these ideas and methods for studying viscoelastic properties of important foods. Since analogies apply across different families of material, we believe that our work may assist various groups within the adhesives industry who cannot afford the expensive and sophisticated rheometers generally used to determine viscoelastic responses.

References

- [1] Papageorge Barrangou, L., Zhang, J., Powell, J., and Gayo, J., "Use of a Brookfield YR-1 Rheometer for Characterization of Viscoelastic Properties," poster paper presented at the *International Food Technology meeting*, Summer 2003.
- [2] *Brookfield YR-1 Rheometer Operating Instructions Manual*. Brookfield Engineering Labs. Inc., Middleboro, MA, 2002.
- [3] Moonay, D. J., "Yield Testing to Ensure Product Consistency," *American Laboratory: News Edition*, June, 2003.
- [4] Billo, J. E., "Excel[®] for Chemists: A Comprehensive Guide," 2nd ed., Wiley-VCH: New York, 2001.

C. T. Scott,¹ R. Hernandez,¹ C. Frihart,¹ R. Gleisner,¹ and T. Tice¹

Method for Quantifying Percentage Wood Failure in Block-Shear Specimens by a Laser Scanning Profilometer

ABSTRACT: A new method for quantifying percentage wood failure of an adhesively bonded block-shear specimen has been developed. This method incorporates a laser displacement gage with an automated two-axis positioning system that functions as a highly sensitive profilometer. The failed specimen is continuously scanned across its width to obtain a surface failure profile. The laser is then moved incrementally along the length of the specimen and repeatedly scanned to obtain a three-dimensional digital profile of the surface. This digital profile can then be reconstructed and analyzed with appropriate software. Special algorithms are used to quantify percentage wood failure and degree of wood failure (depth of wood failure) and to recognize various surface anomalies, such as bondline voids. This paper presents exploratory data on several different types of wood failures and correlates these measurements to the visual inspections of skilled evaluators. The device is very sensitive to most observed failures, particularly those with deep wood failure. However, shallow failures close to the bondline can be problematic. The algorithms allow a "roughness" tolerance to be specified to characterize these surfaces. This new method will be useful for automating measurement of wood failure in block-shear specimens with good precision and repeatability.

KEYWORDS: laser, profilometer, adhesion, block-shear, wood failure

Introduction

Quantifying percentage wood failure of an adhesively bonded block-shear specimen is a challenging process. It requires a highly trained observer to make a visual estimate of total wood failure on the shear cross-section with an estimate of shallow and deep wood failure to the nearest 5 %, as specified in ASTM D 5266 [1]. Generally, wood failure estimators do not have difficulty with very high or very low percentages of wood failure. However, difficulty occurs in the middle "pass-fail" range (30–80 % wood failure), where accuracy is most critical, depending on the adhesive requirements. Visual estimates of wood failure within this range can be interpreted very differently among several observers [2]. The development of new techniques to automate this process would greatly improve and expedite these determinations.

Recently, researchers have developed an image analysis technique to estimate percentage wood failure on block-shear specimens [3]. This technique utilizes a digital camera to capture an image of the specimen surface. The percentage of wood failure is calculated using image analysis software that can differentiate between contrasting regions of exposed adhesive and wood fibers. This technique is useful when this contrast is apparent (which can be improved by the addition of dyes or colorants). However, it is not possible to discriminate between shallow and deep wood failure.

Manuscript received 4 October 2004; accepted for publication 23 February 2005; published September 2005.
Presented at ASTM Symposium on Advances in Adhesives, Adhesion Science, and Testing on 4-6 October 2004 in Washington, DC.

¹ General Engineer, Research Engineer, Project Leader, Physical Science Technician, and Student, respectively, USDA Forest Service, Forest Products Laboratory, One Gifford Pinchot Drive, Madison, WI 53726, USA.

Our goal was to investigate the viability of utilizing an automated laser-scanning profilometer to quantify both percentage wood failure in the shear plane and depth of wood failure about and below the shear plane. Laser displacement gages are sensitive to very small displacements and may be useful in detecting surface irregularities such as those found on failed block-shear specimens. This paper presents a method whereby a laser displacement gage is incorporated into a two-axis positioning system and maneuvered to scan the surface of a failed block-shear specimen. We attempted to evaluate the accuracy of this method by comparing our results with failure estimates made by skilled evaluators. We also attempted to identify specimen characteristics that require a more complex analysis approach.

Experimental

Five previously tested block-shear specimens were selected for this analysis (Figs. 1–3). These specimens were produced from hard maple blocks (25-mm × 25-mm bonded area) according to the provisions of ASTM D 905 [4]. They represented a diverse range of wood failures and contained several unique surface features that could pose some difficulty in visual grading. All specimens had undergone a durability treatment (vacuum-pressure water soak) and were tested wet. After reconditioning, the specimens were visually graded by five observers according to the guidelines of ASTM D 5266. The results were then tabulated.

A laser profilometer was designed to probe the surface of the failed specimen (Fig. 4). This device incorporates a high-resolution laser displacement gage with an automated two-axis positioning system. A NAIS-ANL 2300 Laser with a LM200 Analog Sensor was used to measure surface topography. This laser has a spot size of about 25 μm . To calibrate the laser sensor, twelve gage blocks spanning a range of 2.54 mm were used. These included a series of six gage blocks, in a sequence of 25.4 μm steps, to verify laser sensitivity at the finest resolution anticipated for surface irregularities (each step roughly corresponds to the diameter of a typical wood fiber). Additionally, the surface of a single gage block was scanned to determine the signal resolution of the data acquisition system (about 13 μm).

After calibration, a block-shear specimen was positioned in the profilometer. Two stepper motors, controlled by timed relays, were used to maneuver the specimen under the laser. Specimen position was measured by two linear variable differential transformers (LVDTs), one placed on each axis. A data acquisition system was configured to capture sensor outputs at the rate of 30 Hz. Initially, the specimen was scanned across the non-bonded portion of the adherend (Fig. 5). About 1000 sensor readings were acquired for each profile (or about one reading per 25 μm). The specimen was then advanced 1 mm lengthwise and again scanned across its width. This process was repeated up to 25 times to define a precise beam grid (Fig. 5) for scanning all specimens.

To determine adhesive failure, it was necessary to apply appropriate algorithms to the data. For quantitative analysis data were imported to a spreadsheet, smoothed to remove noise from the LVDTs, and then sorted to remove edge effects. Because there was considerable warp in all specimens due to the durability test, a parabolic function was fit to this distortion and subtracted from the raw data to produce a “flat” bondline. The data were again sorted (in ascending order) to produce a cumulative frequency distribution of surface irregularities (wood failure). Conceptually, a thickness tolerance could then be specified to define the bondline region as well as a depth tolerance for shallow wood failure. The relative population of data within these regions represented the percentage of adhesive, shallow, and deep wood failure.

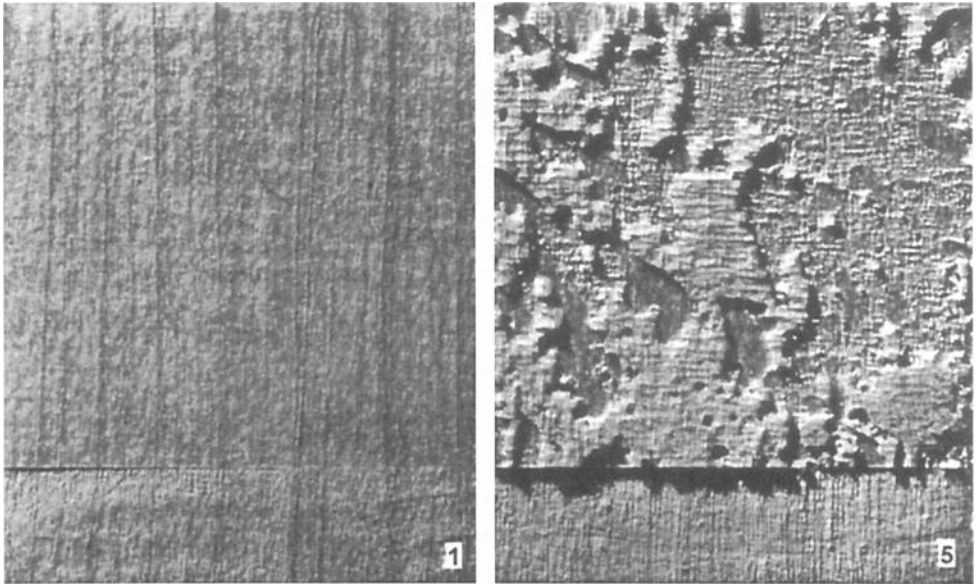


FIG. 1—Specimens 1 and 5 showing different degrees of adhesive failure. Specimen 5 appears also to have large bondline voids.

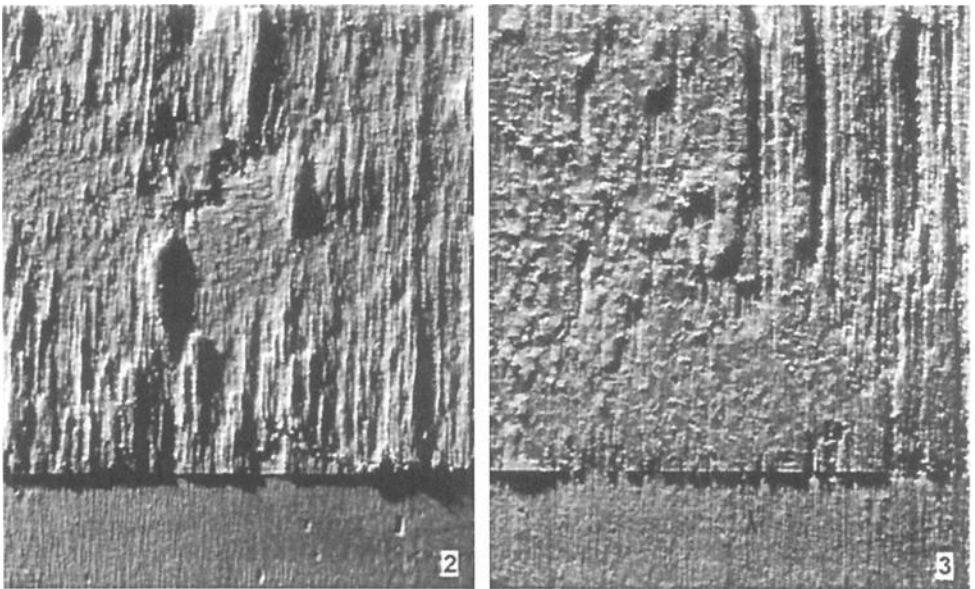


FIG. 2—Specimens 2 and 3 show mixed levels of bondline, shallow, and deep wood failure.

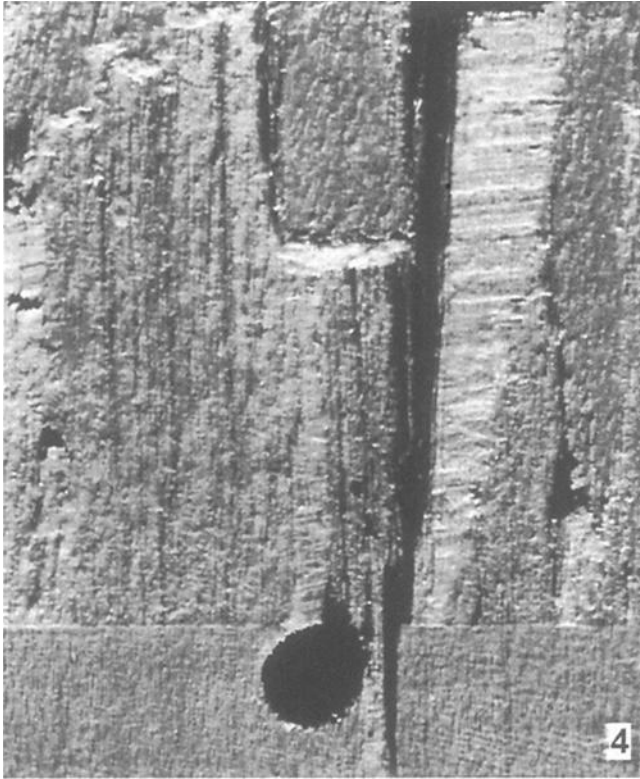


FIG. 3—*Specimen 4 shows severe wood failure extending well beyond the bondline.*

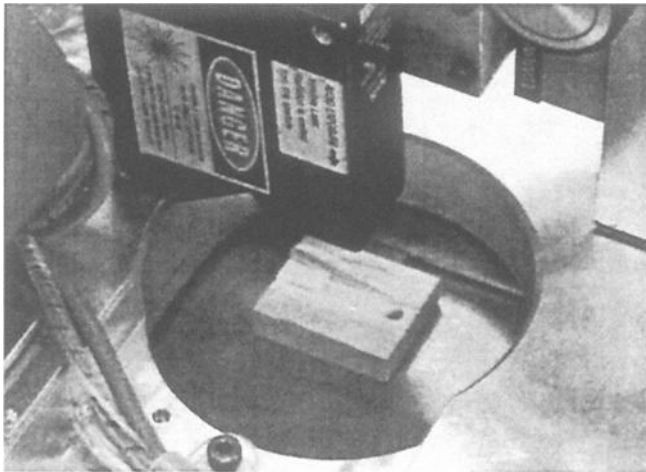


FIG. 4—*Laser beam probing the surface of specimen 4.*

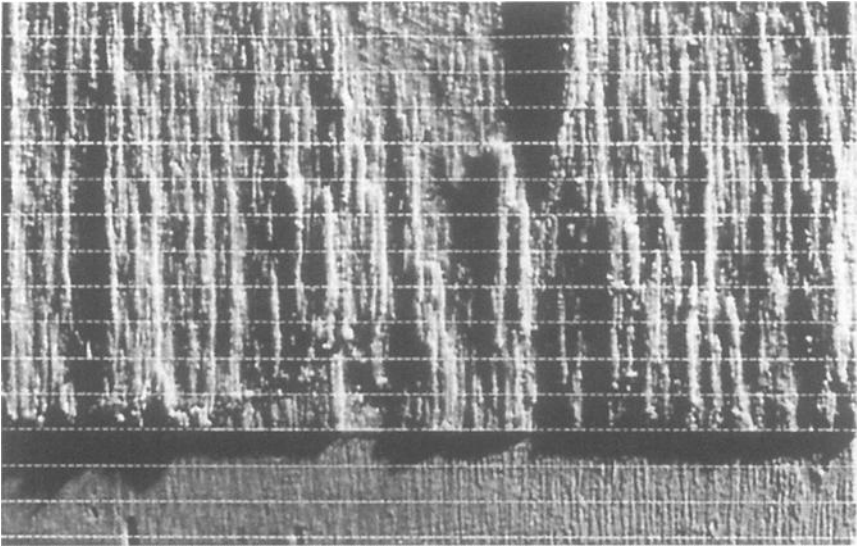


FIG. 5—Location of the beam grid used to recreate the surface of specimen 2.

Results and Discussion

The laser scanning profilometer seemed to function adequately for our purposes. The reflectivity of the failure surface was sufficient to give excellent resolution. However, one of the principal challenges of this technique was determining how concentrated the beam grid pattern would need to be to adequately recreate the failure surface. Because the laser spot size is about $25\ \mu\text{m}$ and the distance selected for incremental advancement was 1 mm, only 2.5 % of the surface area was actually scanned. Therefore, to qualitatively validate this procedure, it was possible to convert the digital coordinates into a three-dimensional contour plot and reproduce a profile of the failure surface (Figs. 6 and 7). For this purpose, averaging every five data points smoothed the surface for better visual appeal. The virtual re-creations could then be compared to the actual specimen (compare Figs. 6 and 7 to Fig. 5). In this case, the re-creation was deemed acceptable.

Unfortunately, an unexpected complication quickly became apparent that potentially compromised the objectivity of this method. This complication was the presence of considerable warp (cup and bow) developed in each specimen after a vacuum-pressure soak. In most cases, the magnitude of cup (distortion across the width) was significantly greater than the surface irregularities (Fig. 8). It was reasonable to assume that the cupping would remain constant along the full length of the specimen, so a parabolic function was fit to this distortion and subtracted from the raw data to produce a “flat” bondline for the whole surface (Fig. 9). Once flattened, the data could then be sorted by distance to the bondline to produce a frequency distribution (Fig. 10). A negative displacement corresponds to wood fragments removed from the adherend. A positive displacement corresponds to wood fragments on the surface that were removed from the opposite adherend. This flattening technique worked well for all specimens except number 5, which had significant cup and bow.

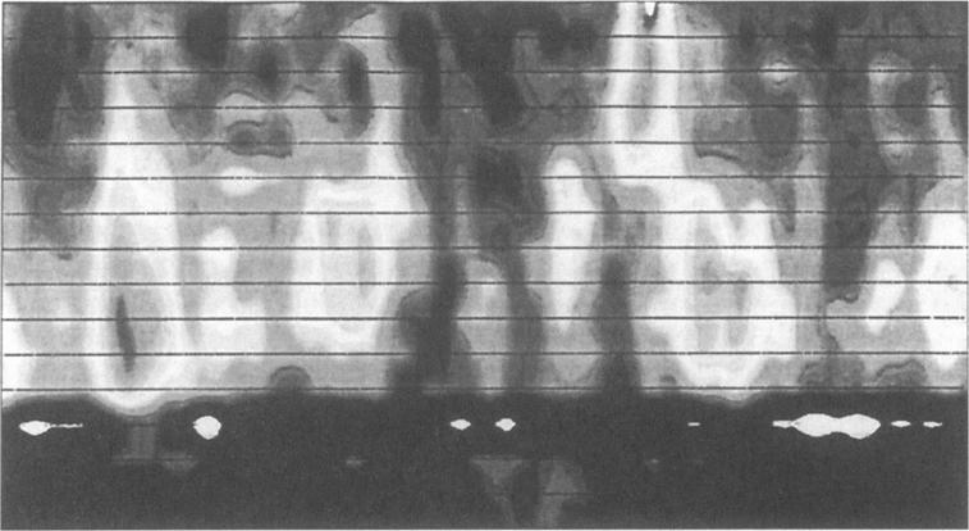


FIG. 6—Two-dimensional digital contour plot of Specimen 2.

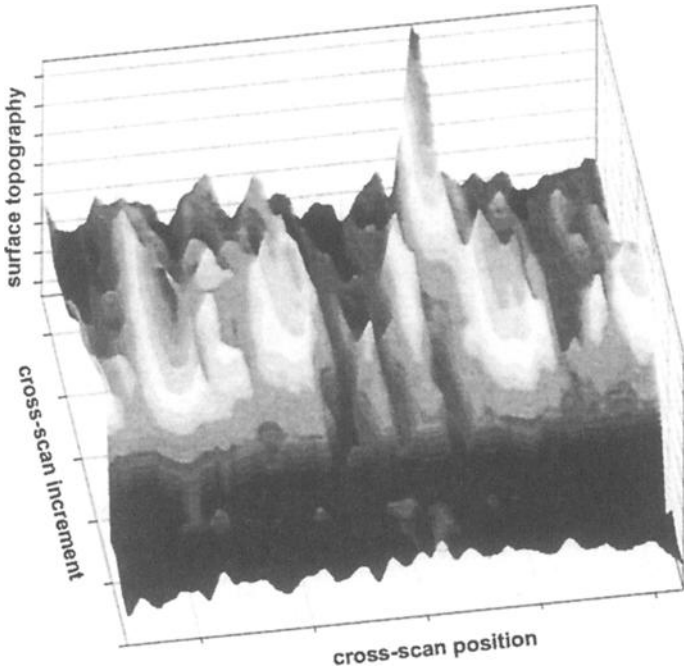


FIG. 7—Three-dimensional digital contour plot of Specimen 2.

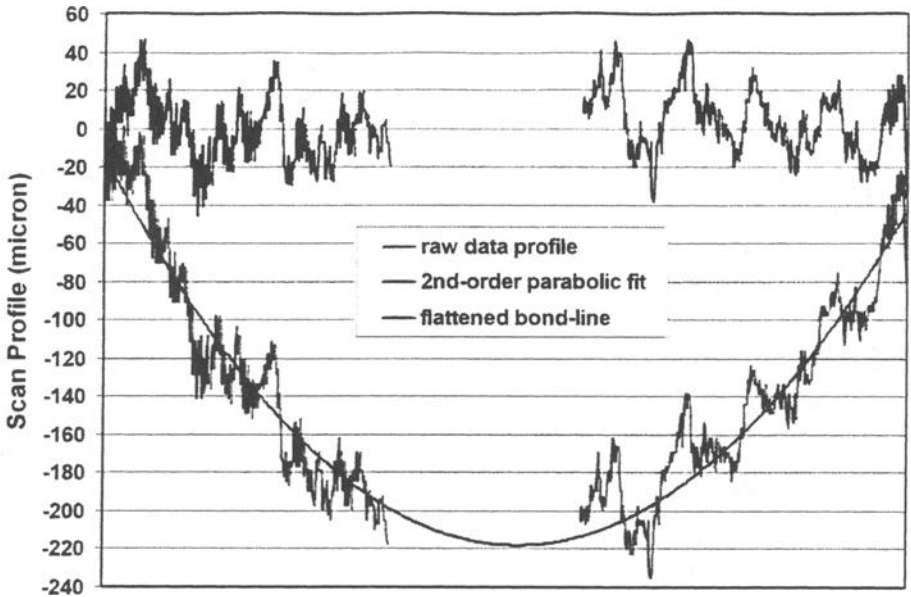


FIG. 8—Typical single-scan profile for Specimen 4 before and after flattening. The gap in the data represents the hole visible on the cut surface (see Fig. 4).

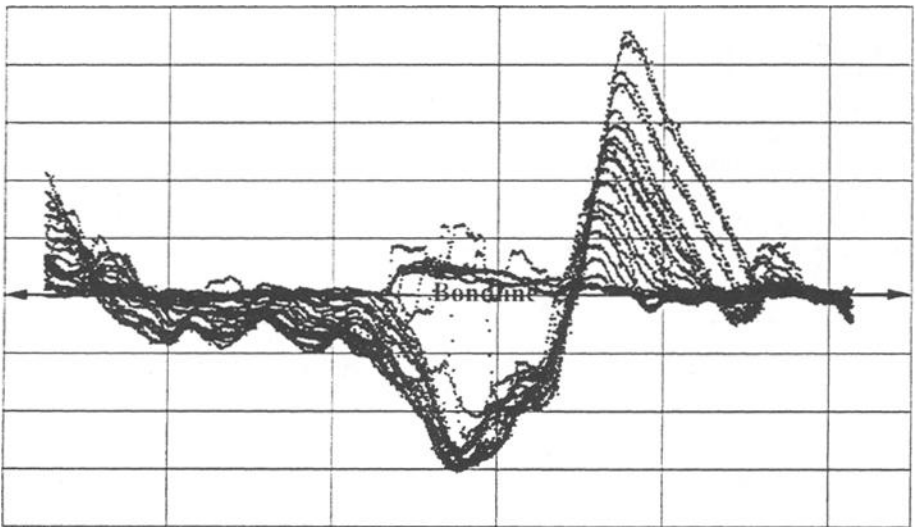


FIG. 9—An end-view representation of multiple laser-scan profiles across the surface of Specimen 4 corrected for warping of the adherend. Note: each division on the vertical scale is 500 μm .

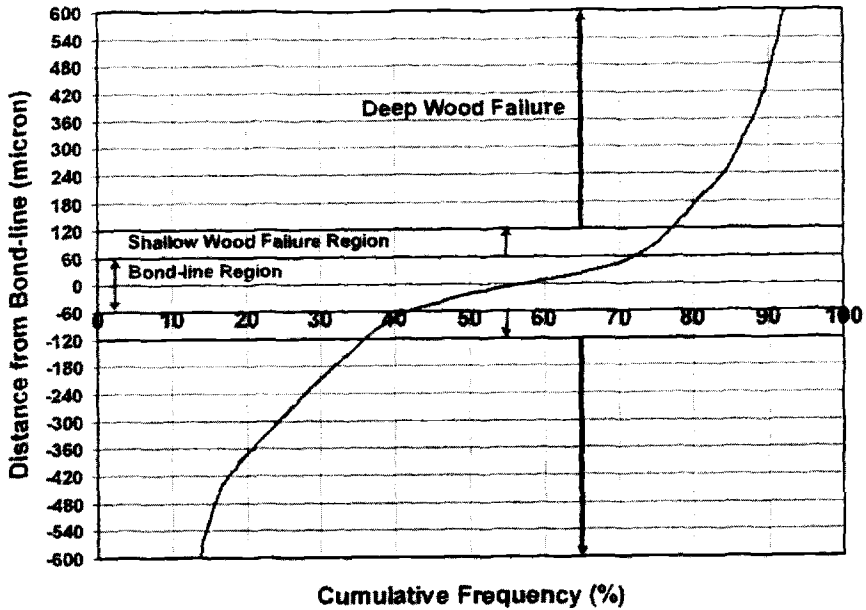


FIG. 10—Cumulative frequency distribution of wood failure for Specimen 4 denoting the bondline tolerance and the shallow wood failure tolerance.

At this point in the analysis, it was possible to define a tolerance for bondline thickness, whereby all points within a prescribed tolerance would be considered adhesive failure, and all points outside this tolerance would be considered wood failure. Furthermore, a second tolerance could be specified to distinguish “shallow” wood failure from “deep” wood failure (Fig. 10). For the specimens evaluated in this study, two tolerances ($\pm 40 \mu\text{m}$ and $\pm 60 \mu\text{m}$) were selected for both the bondline thickness and the depth of shallow wood failure. A typical bondline thickness for block-shear specimens is about $80 \mu\text{m}$, and the thickness of a small fiber bundle is $40\text{--}60 \mu\text{m}$ (or 2–5 fiber diameters). Table 1 summarizes the results from this analysis as well as the visual grading values obtained from the trained observers.

TABLE 1—Percentage wood failure determined by ASTM D method and by laser-scan method.

| Specimen number | Percentage wood failure determined by each reviewer | | | | | Percentage wood failure determined by laser-scan method | |
|-----------------|---|----|----|----|-----|---|-------------------------------|
| | A | B | C | D | E | Tolerance $\pm 40\mu\text{m}$ | Tolerance $\pm 60\mu\text{m}$ |
| | | | | | | Total (shallow/deep) | Total (shallow/deep) |
| 01 | 0 | 0 | 0 | 0 | 0 | 12 (12/0) | 2 (2/0) |
| 02 | 75 | 65 | 75 | 80 | 10 | 44 (24/20) | 30 (21/9) |
| 03 | 70 | 40 | 30 | 45 | 95 | 52 (23/29) | 37 (16/21) |
| 04 | 60 | 90 | 80 | 90 | 100 | 77 (13/64) | 70 (11/59) |
| 05 | 0 | 0 | 0 | 5 | 85 | 38 (25/13) | 22 (18/4) |

Specimen 1 (Fig. 1) was an obvious adhesive failure. All observers rated this at 0 % wood failure. The laser-scan instrument, however, detected a very small degree of shallow wood failure (12 %) at the 40 μm -tolerance levels. Upon closer (microscopic) examination, it was found that there were very narrow ridges of raised radial cells running lengthwise along the specimen, which may have been detected by the laser. No deep wood failure was indicated at either tolerance level.

Specimen 2 (Fig. 2) is an example of a more problematic failure surface to characterize visually. The visual observations were fairly consistent (≈ 75 %), except for E (10 %). However, the laser-scan instrument indicated far less wood failure (44 %) at the 40 μm -tolerance levels. Upon closer examination, the failure surface contained tall, narrow ridges of wood fragments that pulled out of the opposing adherend with regions of exposed adhesive in-between. The laser-scan instrument was sensitive enough to detect these narrow adhesive regions, which may not have been readily apparent in visual observations.

Specimen 3 (Fig. 2) was also a problematic surface to evaluate visually even though the regions of adhesive and wood failure were more obvious than those of specimen 2. Despite this, the visual determinations of wood failure still varied widely (30–95 %). The laser-scan instrument indicated 52 % wood failure at the 40 μm -tolerance levels and 37 % wood failure at the 60 μm -tolerance levels.

Specimen 4 (Figs. 3, 4, and 9) had very obvious and severe wood failure. All observers recognized this severity, and yet the visual ratings still varied considerably (60–100 %). The laser-scan ratings were more consistent (77 % at the 40 μm -tolerance level and 70 % at the 60 μm -tolerance level) and seemed to effectively differentiate shallow wood failure (≈ 10 %) from deep wood failure (≈ 60 %). However, the laser-scan method may have slightly overestimated adhesive and shallow wood failure because every transitional failure through the bondline would include a few data points that were within the bondline and shallow wood tolerance ranges.

Specimen 5 (Fig. 1) was selected for analysis because like specimen 1, it too is an obvious adhesive failure. However, unlike specimen 1, it contained several unique surface features that made it difficult to analyze. Among these were thick adhesive fragments, bondline voids (probably from air bubbles), and shallow (a few fibers) wood failure. Four of the observers declared near complete adhesive failure. However, one observer viewed it very differently (85 % wood failure). In this case, the profilometer analysis did not agree well with visual observations. This was due to considerable warp (cup and bow), which severely compromised the analysis.

Conclusions

The laser-scanning device described above appeared to accurately measure the surface failure topography of a variety of failed block-shear specimens. The laser selected was sensitive to very small displacements and appeared to adequately resolve a variety of surface irregularities. Also, the incremental scan pattern or “beam grid” used to map the failure surface was sufficient to reconstruct a digital contour of that surface.

Ideally, this method would be fairly simple to implement on flat specimens. However, all the specimens tested contained significant degrees of warp due to the effects of a vacuum-pressure exposure test. In many specimens, the magnitude of this distortion was several times that of the surface irregularities. Therefore, it was necessary to “flatten” the bondline by fitting a parabolic function to the “cup” and then subtract the fit from the raw data. Next, the data were sorted in ascending order to produce a cumulative distribution for all measured surface displacements. A thickness tolerance could then be specified to define the bondline region as well as a depth

tolerance for shallow wood failure. The relative population of data within these regions represented the percentage of adhesive, shallow, and deep wood failure.

Specimen 5 was particularly problematic because it contained significant distortion (both cup and bow). This specimen had obvious regions of bondline voids that should have been readily detected by the laser-scanning method, but were instead obscured by the specimen distortion. For this specimen, fitting a parabolic function to a single scan and subtracting it from all the scans was not sufficient to reproduce a flat bondline. Rather, to improve the analysis, it may have been useful to initially fit a bi-quadratic function to the data to completely remove all surface distortion, and then apply the relevant tolerance to better resolve these surface features.

When compared with round-robin evaluations, we found that the laser-scanning method fell within the range of observations for visual estimates of percent wood failure, although some of these estimates varied widely. Additionally, the laser-scanning method could discriminate between regions of bondline and shallow wood failure that were not easily distinguished in visual observations. Furthermore, by prescribing a thickness tolerance to the frequency distribution of surface irregularities, it was then possible to quantify the degree of shallow and deep wood failure. This feature of the laser-scanning method is particularly useful for analyzing the more problematic mixed-mode failures that are critical for determining adhesive performance in bonded wood joints.

References

- [1] ASTM Standard D 5266, "Standard Practice for Estimating the Percentage of Wood Failure in Adhesive Bonded Joints," ASTM International, West Conshohocken, PA, June 1999.
- [2] "Wood Failure Round Robin Report," CSA/A370/SC05.3, Canadian Standards Association, Mississauga, Ontario, August 2002.
- [3] Zink, A. G. and Kartunova, E., "Wood Failure in Plywood Shear Samples Measured with Image Analysis," *Forest Prod. J.*, Vol. 48, No. 4, April 1998, pp. 69–74.
- [4] ASTM Standard D 905, "Standard Test Method for Strength Properties of Adhesive Bonds in Shear by Compression Loading," ASTM International, West Conshohocken, PA, October 2003.

Akhrawat Lenwari,¹ Pedro Albrecht,² and Mark Albrecht³

SED Method of Measuring Yield Strength of Adhesives and Other Materials

ABSTRACT: The strain energy density (SED) method of determining the yield strength of adhesives and other materials that is based on the fundamental principles of mechanics is described in this paper. The results from two sets of tests are reported. In the first set, the yield strength of multiple specimens made of the adhesive FM 300K was determined in the dry/cold, moderate, and humid/hot environments; the strain rates were $10^{-2}/s$, $10^{-4}/s$, and $10^{-6}/s$. In the second set, single specimens of five other adhesives were tested in the dry/cold and humid/hot environments; the strain rate was $10^{-4}/s$. Fifty-three out of the 60 specimens have yield strengths calculated with the SED method that are equal to or lower than the values obtained with the 0.2 % offset method suggested in the ASTM specifications. The SED method is most valuable when the stress-strain curve of the material exhibits a gradual transition from elastic to the inelastic behavior typical of polymers, aluminum, and some very high strength steels. To ensure the safety of bonded structures, the yield strength of adhesives should be determined with the SED method, which is based on the fundamental principles of mechanics, instead of on an arbitrary estimate of strain offset. Although applied in this paper to stress-strain curves of adhesives, the SED method may also discern the onset of yielding and instability in columns and beams. To ensure that the yield strength of adhesives for bonding load-bearing structures is not systematically overestimated, the authors recommend using the SED method in lieu of the 0.2 % offset method.

KEYWORDS: Yield strength, adhesives, metallic materials, strain energy density, environment, relative humidity, temperature, strain rate

Introduction

Some common terms used by engineers in ascribing elastic-plastic properties of materials are the proportional limit, the elastic limit, and the yield strength. 1) The proportional limit is the point at which the stress and strain first depart from being proportional, i.e., the point where the stress-strain curve is no longer "straight." It is noted that for many materials the early segment of the stress-strain curve is not straight, so the term proportional limit is not clearly defined. 2) The elastic limit is the point on the stress-strain curve where the material is no longer elastic. Determining the elastic limit in an experiment is often difficult, requiring loading and unloading, as well as accurate measurements of the permanent deformation. 3) The yield strength, which is the parameter used in the design of structures, is defined as the stress at which the deformation of the material changes from elastic to plastic. Engineers sometimes use the proportional limit, the elastic limit, and the yield strength somewhat interchangeably, although the three terms have distinctly different definitions. Because their values are relatively close to each other, engineers

Manuscript received 25 August 2004; accepted for publication 6 May 2005; published November 2005. Presented at ASTM Symposium on Advances in Adhesives, Adhesion Science, and Testing on 4-6 October 2004 in Washington, DC.

¹ Post-Doctoral Researcher, Department of Civil and Environmental Engineering, University of Maryland, College Park, MD 20742. E-mail: akhrawat@umd.edu.

² Professor Emeritus, 4201 Woodberry Street, University Park, MD 20782. E-mail: pedroalb@eng.umd.edu.

³ PAA Consultant Inc., 4201 Woodberry Street, University Park, MD 20782.

Copyright © 2005 by ASTM International, 100 Barr Harbor Drive, PO Box C700, West Conshohocken, PA 19428-2959.

see the three terms as referring to the stress where permanent damage in the material starts to occur: i.e., exceeding this stress is likely to damage the structure.

The strain energy density (SED) method of determining the yield strength of materials described in this paper has two distinct advantages over, for example, the offset method. First, it is more reliable, and secondly, it is more related to the atomic/molecular mechanisms associated with the actual damage.

Structural Steels

Stress-strain curves for carbon and high-strength steels (250 to 485 MPa yield strength) and some quenched and tempered steels (690 MPa yield strength) exhibit a discontinuous yield plateau from which the upper and lower yield strengths can easily be determined. However, some quenched and tempered steels have stress-strain curves that exhibit a continuous transition from the elastic to the plastic region. In this case, the yield strength is commonly determined by the offset method: the yield strength is reached when the stress-strain curve intersects a line having a slope equal to the modulus of elasticity and constructed such that it is offset from the linear portion of the stress-strain curve by an amount equal to the specified strain, usually 0.2 %. Note 26 in the Standard Test Methods for Tension Testing of Metallic Materials, ASTM Designation E 8, states that “a verified strain range of 0.2 % to 2.0 % is appropriate for determining the yield strength for many metals,” thus implying that a 0.2 % offset is reasonable for metals.

Adhesives

Unlike those of most structural steels, the stress-strain curves of 27 adhesives reported by Albrecht et al. [1–3] exhibited, without exception, a continuous transition from the elastic to the plastic region. None of the adhesives had the discontinued yield plateau that is characteristic of most structural steels. Because adhesives do not have upper and lower yield strengths, previous investigators determined the yield strength with the offset method. The *Standard Method for Tensile Properties of Plastics*, ASTM Designation D 638, mentions a 0.1 % offset yield strength. The *Standard Test Method for Tensile Properties of Thin Plastic Sheeting*, ASTM Designation D 882, refers the reader to ASTM D 638.

Considering that the stress-strain curves for most metallic materials are not significantly affected by temperature and strain rate, the common choice of the 0.2 % offset yield strength may be acceptable. But stress-strain curves for adhesives vary greatly with relative humidity (RH), ambient temperature, strain rate, and adhesive type. Thus, an alternative method is needed for determining the yield strength of adhesives and other materials that exhibit a continuous transition from the elastic to the inelastic regions. The method should be based on the fundamental principles of mechanics of materials.

Evidence of Plasticity

Lüder lines, also called shear bands, are visible evidence of yielding in materials, including metals and adhesives [4–6]. The bands are inclined at an angle of 55° with respect to the tensile stress [4]. Figure 1 shows a Lüder line in a tensile specimen made of *High-Strength Low-Alloy Structural Steel with 345 MPa Minimum Yield Point to 100-mm Thick*; ASTM designation A588. The specimen is 6-mm thick by 50-mm wide and has a 200-mm gage length.

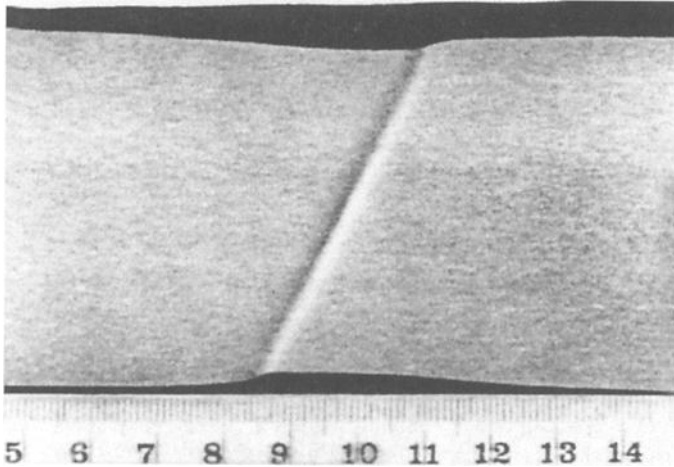


FIG. 1—Lüder line in tensile specimen of ASTM A588 structural steel.

Albrecht et al. [1] tested specimens made of collagen, which has a protein structure consisting of long-chained, water-bridge molecules. Collagen serves as the chief tensile-bearing material for all mammals and fish [7]. Used as an adhesive (e.g., “rabbit skin glue”) in the past, collagen still has a commercial value. Collagen can be refined to gelatin for use in photographic emulsions, medicine capsules, and in many food and beauty products. Being hydrophilic and being easily cast into thin films, collagen is a valuable material for studying the effect of moisture on adhesives. According to Gordon [8]: “Collagen exists in various forms, but it may consist of twisted strings or ropes of protein molecules, and its resistance to extension is basically due to the need to stretch the bonds between the atoms in the molecules; that is to say, it is a Hookean material like nylon or steel.”

Figure 2 shows Lüder lines in a tensile specimen made of collagen that was 0.25-mm thick by 6-mm wide; the gage length was 127-mm. Furthermore, Bauwens [5] reported Lüder lines in thin specimens of polyvinyl chloride. In all three materials cited above, the Lüder lines were inclined at an angle consistent with Nadai’s theoretical model [4].

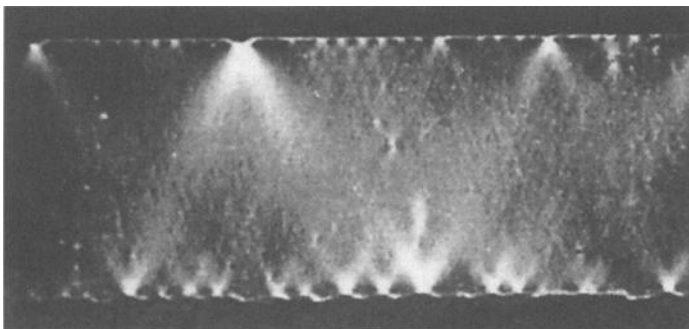


FIG. 2—Lüder lines in tensile specimen of collagen.

Objective

This paper presents a method of determining the yield strength of materials that is based on the fundamental principles of mechanics of materials instead of on an estimate of offset strain. The method infers the yield strength from a significant change in the dissipated strain energy density. This herein named Strain Energy Density (SED) method is intended for materials that exhibit a continuous transition from elastic to inelastic behavior. While the SED method was demonstrated for adhesives in this paper, the authors believe that this method is applicable to most materials that exhibit stress-strain curves with a gradual transition from the elastic to the inelastic behavior.

Experiment Design

Automated Testing System

With the advent of electronics and computers, automated material testing is progressing fast. Today, computer-controlled equipment can be built in-house, as was done for the present study. As a result of these advancements, tests of thin bulk adhesive specimens can be performed with high precision and reproducibility. The testing system consists of tensiometers, an environmental chamber, a switch and balance unit, a strain indicator, a loading system, a data acquisition (DAQ) board, and a desktop computer [2,3]. A tensiometer is a small, low-load, displacement-controlled, screw-driven tensile testing device. Up to six tensiometers can be placed in an environmental chamber in which relative humidity (RH) and temperature are controlled. A stepper motor, controlled via the parallel (printer) port of the computer, turns the threaded loading rod that pulls the movable grip holding the specimen. The switch and balance unit receives the signals from the strain gages mounted on the load cell of the tensiometer. The strain indicator conditions and amplifies the signals, which are converted to applied load and specimen elongation. The PC reads the output from the load cell through a DAQ board connected to the strain indicator's analog output. The conditioned signals are sampled at a specified rate and stored on the hard disk.

Adhesives

FM 300K was the principal adhesive tested in the present study. This hot-cured, modified epoxy adhesive, manufactured by Cytec Engineered Materials (formerly Cytec Fiberite) is available in sheets with three different moisture-resistant polyester carriers. The manufacturer recommended the tight-knit, tricot, polyester carrier for ease of controlling bondline thickness and for its good blend of structural and handling properties during lay-up. According to the manufacturer, FM 300K has superior metal-to-metal peel strength, can be used at service temperatures of -55 to $+150^{\circ}\text{C}$, and resists moisture and corrosion in high humidity environments with little reduction in mechanical properties. Its glass transition temperature varies from 150°C in a dry environment to 123°C when fully saturated. Standard weight and nominal film thickness before curing are $3.9 \pm 0.25 \text{ N/m}^2$ and 0.33 mm , respectively.

For comparison with FM 300K, specimens of the following five adhesives were tested: 3M 3559 made by 3M Co.; and four adhesives Adh 14, Adh 96, Adh 98, and Adh II-3H made by Martin Marietta. FM 300K was intended for possible application in highway bridges; the others were intended for use on military bridges. For more information on the properties of the latter

four adhesives. the reader is referred to Martin Marietta Technologies, Inc., Baltimore, MD; and the U.S. Army Research, Development and Engineering Center, Fort Belvoir, VA.

Curing

Films of adhesive FM 300K, 200-mm long by 150-mm wide, were placed between two aluminum plates, 300-mm long by 230-mm wide and 16-mm thick. Both film surfaces were covered with Mylar sheets to prevent the adhesive from bonding to the aluminum plates. Narrow metal shim strips 0.32-mm thick were placed along the four edges to control the thickness of the cured film. The assembly was clamped and placed in a precision laboratory oven. The temperature was uniformly raised over a period of 60 minutes to the target curing temperature of 177°C. After one hour of curing at that temperature, the assembly was removed from the oven, cooled for three hours at an ambient temperature, and then disassembled.

Cutting

The specimens were cut from a central area of a film about 25 mm away from all four edges. Each cut was made by running a heavy-duty carpet blade about 10 times at medium hand pressure along a rigid, machined aluminum bar. This cutting method resulted in specimens with straight and parallel edges. Utmost care was exercised in cutting the specimens to prevent nicks and tears at the edges that could cause a specimen to fail prematurely. After cutting, the specimen edges were sanded with 3M 326U Aluminum Oxide Resin Paper 220 to remove cracks and scratches and to straighten the edges. Several specimens were clamped between two machined plates for ease of sanding.

Dimensions

The thickness of the specimen was measured with a digital micrometer; its width was measured with a 50× traveling microscope. The digital micrometer and the traveling microscope were accurate to ±0.0025 mm. These measurements were made at five cross-sections spaced 30 mm apart and centered about the midpoint of the 127-mm gage length between the two grips. The cross-sectional area is the product of thickness and width. The smallest of the five areas was used to calculate the stress for the stress-strain curves. Table 1 lists the mean and coefficient of variation of the thickness, width, and area of three randomly selected specimens.

After a specimen was installed in the tensiometer and the grips were tightened, its gage length between grips was measured with a caliper accurate to 0.05 mm. The gage length was subsequently used to calculate the strain.

TABLE 1—*Typical dimensions of FM 300K adhesive specimens.*

| Specimen I.D. | Width | | Thickness | | Area | |
|------------------|--------------|-----------|--------------|-----------|----------------------------|-----------|
| | Mean (mm) | CV (%) | Mean (mm) | CV (%) | Mean (mm ²) | CV (%) |
| 11-5 | 5.95 | 0.69 | 0.322 | 2.58 | 1.916 | 2.81 |
| 12-11 | 5.90 | 0.38 | 0.330 | 3.69 | 1.951 | 3.90 |
| 13-15 | 5.83 | 0.90 | 0.327 | 3.08 | 1.908 | 3.31 |

Conditioning

Relative humidity (RH) is defined as the partial pressure of water divided by the vapor pressure of water at the ambient temperature. Highway bridges in service are exposed to 30 to 100 % RH and -40 to 50°C . RH and temperature greatly affect the mechanical properties of polymeric materials. To properly account for these environmental effects, the moisture content in the specimen must be in equilibrium with the RH of the air in the chamber. Likewise, the specimen's temperature must be the same as the temperature inside the chamber. Equilibrating the RH takes a long time, but equilibrating the temperature only takes a short time. According to ASTM D 882 and the *ASTM Practice for Conditioning Plastics and Electrical Insulation Materials for Testing*, ASTM Designation D 618, the specimens should be conditioned to the environment for 40 or more hours prior to testing.

The required moisture conditioning time depends on the specimen thickness and the diffusion coefficient of the material and the environment. It took 48 h to equilibrate the moisture content of a 0.3-mm-thick FM 300K specimen exposed to the 50°C and 90 % RH hot/humid environment inside an environmental chamber. Still, all specimens were conditioned for two weeks prior to testing [2,3].

In another example, Ishida [9] and Ishida and Allen [10] reported that about 100 days were needed to condition their disk-shaped epoxy specimen that had a 50-mm diameter and a 3.2-mm thickness.

Test Matrix

Two experiments were designed. First, to rationally evaluate the effects of environment and strain rate on the yield strength, the specimens were arranged in a two-way factorial experiment design with three levels of environment, three levels of strain rate, and replicate specimens per cell:

- Adhesive: FM 300K
- Environments: 15 % RH/ -15°C (dry/cold), 50 % RH/ 30°C (moderate), and 85 % RH/ 50°C (humid/hot)
- Strain rates: $10^{-2}/\text{s}$, $10^{-4}/\text{s}$, and $10^{-6}/\text{s}$
- Number of specimens: 50 distributed over the cells as shown in Tables 2 to 4. The specimen I.D. consists of the sheet number followed by the number of the specimen cut from that sheet.

In the second experiment, the effect of adhesive type on yield strength was determined:

- Adhesives: FM 300K, 3M 3559, Adh 14, Adh 96, Adh 98, and II-3H
- Environments: 15 % RH/ -15°C (dry/cold) and 85 % RH/ 50°C (humid/hot)
- Strain rate: $10^{-4}/\text{s}$
- Number of specimens: 1 per adhesive and environment

Figures 3 and 4 show the stress-strain curves of adhesive FM 300K in three environments tested at $10^{-2}/\text{s}$ and $10^{-4}/\text{s}$ strain rates, respectively.

Figure 5 shows the stress-strain curves of six adhesives in two environments tested at a $10^{-4}/\text{s}$ strain rate. The adhesives are identified as follows (1) 3M 3559; (2) Adh14; (3) Adh 96; (4) Adh 98; (5) Adh II-3H; and (6) FM 300K.

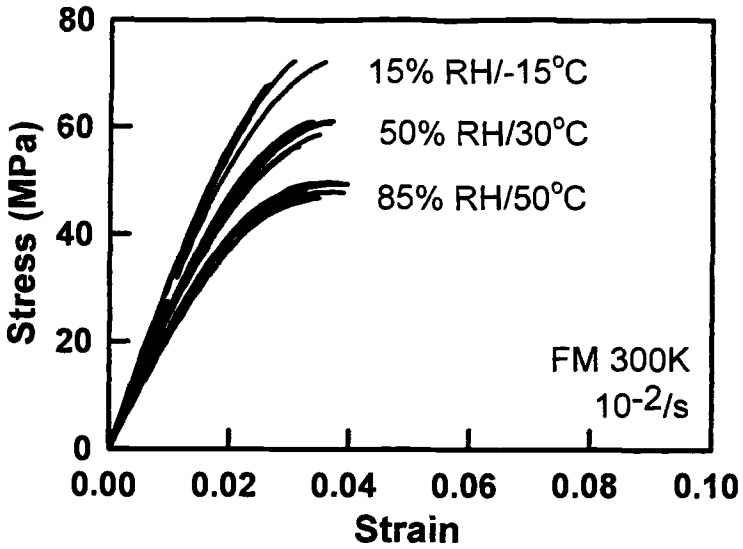


FIG. 3—Stress-strain curves of FM 300K in three environments and $10^{-2}/s$ strain rate.

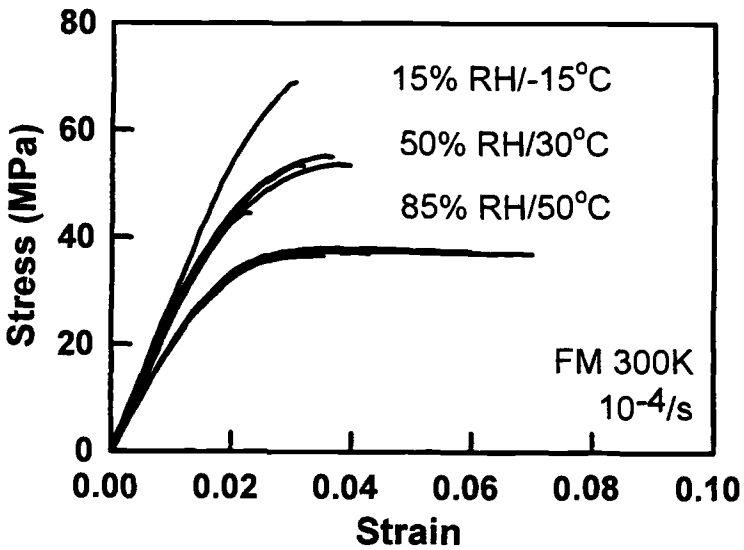


FIG. 4—Stress-strain curves of FM 300K in three environments and $10^{-4}/s$ strain rate.

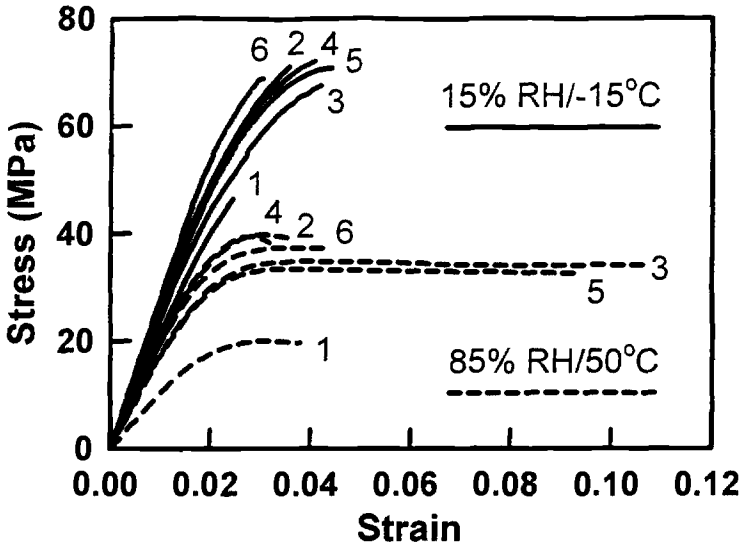


FIG. 5—Stress-strain curves of different adhesives in two environments and 10^{-4} /s strain rate.

Yield Strength

Strain Energy Density (SED) Method

The method consists of testing a tensile specimen at a constant strain rate, recording the load and the displacement at equal increments of displacement, and plotting the stress-strain curve (Fig. 6). Each vertical bar in the figure represents an increment of strain energy density (SED). However, to improve the accuracy of finding the yield point, the authors retained only the SED corresponding to the shaded triangular areas atop each bar as the indicator of elastic and inelastic behaviors:

$$\Delta u = \frac{1}{2} \Delta \sigma \cdot \Delta \epsilon = \frac{1}{2} (\sigma_{i+1} - \sigma_i) (\epsilon_{i+1} - \epsilon_i) \tag{1}$$

where Δu = SED, $\Delta \sigma$ = stress increment, and $\Delta \epsilon$ = strain increment. It is emphasized that the strain increments must be constant during the entire test. The adhesive behaves elastically for as long as Δu is linear and inelastically when Δu deviates from a linear trend. The yield strength is taken as the stress at the point where the value of the SED increment deviates from a linear trend.

As an example, the test procedure is described below for the FM 300K specimen 11-12, which was tested in an environment of 15 % RH/-15°C and at a strain rate of 10^{-4} /s:

1. Performed a tensile test in accordance with the ASTM Standards D 638 for plastics, D 882 for thin plastic sheeting, and E 8 for metals. The specimen should be tested in an environment and at a strain rate that are similar to those of the structure in service.
2. Tested the specimen in displacement control, ensuring that the increments remain constant.
3. Plotted the stress-strain curve (Fig. 7).

4. For all 50 displacement increments, calculated the strain energy density, Δu , with Eq 1 and plotted the values as a function of strain (Fig. 8). A visual inspection of the data suggested that the transition between the elastic and inelastic regions occurred between the 30th and 40th data points. The points to the left of the 30th data point fell along a straight line— Δu linear, elastic region—with little scatter. Those to the right of the 40th data point fell on a descending curve— Δu decreasing, inelastic region—with a larger scatter, as shown in the insert of Fig. 8.
5. Fitted a straight line through the data points in the elastic region, calculated the standard deviation, and drew the lower and upper confidence limits at three standard deviations from the mean line.
6. The yield strength is at the first data point that fell below the lower confidence limit. For this specimen, the onset of yielding occurred at the 33rd data point for which $\sigma_y = 51.3$ MPa and $\epsilon_y = 0.0189$ (Table 3).
7. Calculated the elastic modulus by fitting a straight line through the data points in the elastic region.
8. Given the yield strength from step 6 and the elastic modulus from step 7, calculated with Eq 2 the value of the SED offset strain, 0.06 % (Table 3).

$$\text{SED offset strain (\%)} = \left(\epsilon_y - \frac{\sigma_y}{E} \right) 100 \quad (2)$$

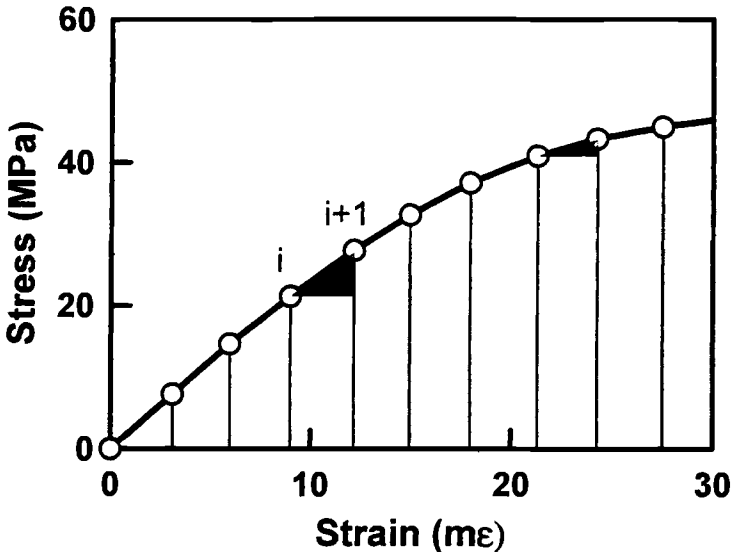


FIG. 6—Definition of SED in present study.

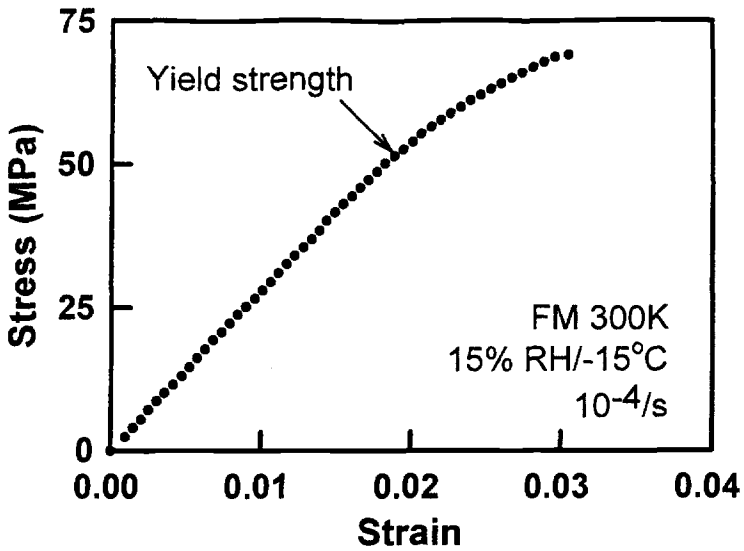


FIG. 7—Stress-strain curve at 15 % RH, -15°C and $10^{-4}/s$ strain rate.

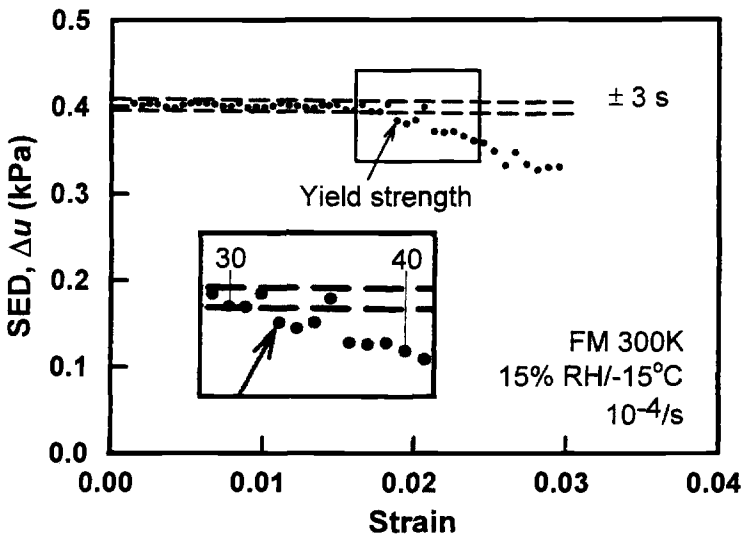


FIG. 8—Yield strength at 15 % RH, -15°C and $10^{-4}/s$ strain rate.

Effect of Environment and Strain Rate

Tables 2–4 show the effect of the dry/cold, moderate, and humid/hot environments on the tensile properties of the adhesive FM 300K tested at the $10^{-2}/s$, $10^{-4}/s$, and $10^{-6}/s$ strain rates, respectively. The values of the yield strength, the yield strain, and the offset obtained with the SED method and the corresponding values from the 0.2 % offset method are shown. The tensile strength, rupture strain, and elastic modulus are provided for information. On average, the time to rupture of the specimens tested at the $10^{-2}/s$, $10^{-4}/s$, and $10^{-6}/s$ strain rates were 4 seconds, 6 minutes, and 15 hours, respectively. The data are listed in ascending order of yield strength. The tensile properties listed in parentheses at the bottom of each cell are averages for replicate specimens. For ease of comparison, these averages are summarized in Table 5.

All but four of the fifty specimens have yield strengths and offset strains calculated with the SED method that are equal to or lower than the values from the 0.2 % offset method. In the three environments (dry/cold, moderate, and humid/hot) the average yield strengths are:

- At $10^{-2}/s$ strain rate (Table 2): 43.3, 45.7, and 29.8 MPa for the SED method versus 56.4, 41.3, and 36.1 MPa for the 0.2 % offset method.
- At $10^{-4}/s$ strain rate (Table 3): 48.3, 35.4, and 25.2 MPa for the SED method versus 56.9, 39.3, and 28.5 MPa for the 0.2 % offset method.
- At $10^{-6}/s$ strain rate (Table 4): 39.4, 30.0, and 23.5 MPa for the SED method versus 47.7, 35.2, and 25.7 MPa for the 0.2 % offset method.

TABLE 2—*Tensile properties of FM 300K adhesive at $10^{-2}/s$ strain rate.*

| Specimen I.D. | Strain Energy Density Method | | | 0.2 % Offset Method | | Tensile Strength (MPa) | Rupture Strain | Elastic Modulus (MPa) |
|-------------------------------------|------------------------------|--------------|------------|----------------------|--------------|------------------------|----------------|-----------------------|
| | Yield Strength (MPa) | Yield Strain | Offset (%) | Yield Strength (MPa) | Yield Strain | | | |
| Dry/cold environment: 15 % RH/–15°C | | | | | | | | |
| 11-4 | 40.0 | 0.0128 | 0.05 | 53.9 | 0.0185 | 76.6 | 0.0346 | 3,240 |
| 2-1 | 40.7 | 0.0145 | 0.01 | 57.1 | 0.0224 | 72.2 | 0.0357 | 2,830 |
| 12-4 | 41.6 | 0.0137 | 0.05 | 56.7 | 0.0200 | 67.8 | 0.0265 | 3,160 |
| 12-20 | 44.9 | 0.0169 | 0.02 | 57.2 | 0.0232 | 66.5 | 0.0293 | 2,690 |
| 1-7 | 49.5 | 0.0168 | 0.10 | 57.2 | 0.0202 | 66.4 | 0.0251 | 3,130 |
| Average | (43.3) ^a | (0.0149) | (0.05) | (56.4) | (0.0209) | (69.9) | (0.0302) | (3.010) |
| Moderate environment: 50 % RH/30°C | | | | | | | | |
| 11-17 | 42.1 | 0.0175 | 0.14 | 46.2 | 0.0197 | 61.0 | 0.0371 | 2,610 |
| 12-16 ^b | 44.8 | 0.0202 | 0.29 | 39.0 | 0.0168 | 58.6 | 0.0349 | 2,590 |
| 13-4 ^b | 45.6 | 0.0211 | 0.33 | 37.9 | 0.0164 | 56.3 | 0.0314 | 2,560 |
| 13-12 ^b | 47.5 | 0.0211 | 0.31 | 40.8 | 0.0172 | 50.5 | 0.0238 | 2,640 |
| 11-13 ^b | 48.3 | 0.0214 | 0.29 | 42.5 | 0.0181 | 60.7 | 0.0367 | 2,610 |
| Average | (45.7) | (0.0201) | (0.27) | (41.3) | (0.0176) | (57.4) | (0.0328) | (2.600) |
| Humid/hot environment: 85 % RH/50°C | | | | | | | | |
| 6-5 | 26.7 | 0.0123 | 0.04 | 36.2 | 0.0179 | 47.8 | 0.0326 | 2,240 |
| 10-9 | 28.1 | 0.0139 | 0.06 | 35.3 | 0.0186 | 47.8 | 0.0389 | 2,120 |
| 5-3 | 29.9 | 0.0150 | 0.10 | 34.3 | 0.0179 | 46.8 | 0.0349 | 2,130 |
| 9-2 | 29.9 | 0.0139 | 0.08 | 36.0 | 0.0172 | 49.5 | 0.0344 | 2,290 |
| 11-2 | 31.1 | 0.0147 | 0.07 | 37.1 | 0.0184 | 49.3 | 0.0395 | 2,220 |
| 8-7 | 33.1 | 0.0156 | 0.11 | 37.8 | 0.0184 | 49.6 | 0.0380 | 2,290 |
| Average | (29.8) | (0.0142) | (0.08) | (36.1) | (0.0181) | (48.5) | (0.0364) | (2.220) |

^a The tensile properties listed in parentheses are averages for replicate specimens.

^b All but four specimens have yield strengths and offset strains calculated with the SED method that are equal to or lower than the values from the 0.2 % offset method.

TABLE 3—Tensile properties of FM 300K adhesive at 10⁻⁴/s strain rate.

| Specimen I.D. | Strain Energy Density Method | | | 0.2 % Offset Method | | Tensile Strength (MPa) | Rupture Strain | Elastic Modulus (MPa) |
|-------------------------------------|------------------------------|--------------|------------|----------------------|--------------|------------------------|----------------|-----------------------|
| | Yield Strength (MPa) | Yield Strain | Offset (%) | Yield Strength (MPa) | Yield Strain | | | |
| Dry/cold environment: 15 % RH/-15°C | | | | | | | | |
| 13-6 | 44.4 | 0.0162 | 0.03 | 54.3 | 0.0212 | 62.6 | 0.0267 | 2.790 |
| 12-7 | 49.2 | 0.0178 | 0.08 | 56.7 | 0.0214 | 65.3 | 0.0277 | 2.900 |
| 11-12 | 51.3 | 0.0189 | 0.06 | 59.8 | 0.0232 | 68.9 | 0.0304 | 2.800 |
| Average | (48.3) ^a | (0.0176) | (0.06) | (56.9) | (0.0219) | (65.6) | (0.0283) | (2.830) |
| Moderate environment: 50 % RH/30°C | | | | | | | | |
| 11-21 | 31.7 | 0.0129 | 0.07 | 38.5 | 0.0164 | 53.7 | 0.0320 | 2.590 |
| 12-1 | 32.3 | 0.0128 | 0.09 | 36.5 | 0.0152 | 44.5 | 0.0230 | 2.720 |
| 13-5 | 33.8 | 0.0144 | 0.12 | 35.9 | 0.0155 | 53.7 | 0.0397 | 2.570 |
| 11-15 | 35.8 | 0.0148 | 0.11 | 38.9 | 0.0165 | 55.3 | 0.0366 | 2.610 |
| 12-10 | 38.0 | 0.0159 | 0.16 | 40.0 | 0.0170 | 53.9 | 0.0320 | 2.650 |
| 13-11 | 40.5 | 0.0179 | 0.10 | 46.0 | 0.0213 | 51.1 | 0.0269 | 2.390 |
| Average | (35.4) | (0.0148) | (0.11) | (39.3) | (0.0170) | (52.0) | (0.0317) | (2.590) |
| Humid/hot environment: 85 % RH/50°C | | | | | | | | |
| 12-12 | 22.3 | 0.0116 | 0.04 | 28.1 | 0.0158 | 38.0 | 0.0491 | 2.000 |
| 12-6 | 22.4 | 0.0116 | 0.05 | 27.5 | 0.0152 | 37.4 | 0.0429 | 2.020 |
| 11-1 | 25.3 | 0.0135 | 0.10 | 28.8 | 0.0162 | 36.6 | 0.0354 | 2.020 |
| 13-7 | 26.5 | 0.0147 | 0.11 | 28.0 | 0.0160 | 37.4 | 0.0700 | 1.950 |
| 11-16 | 27.1 | 0.0144 | 0.09 | 30.3 | 0.0170 | 37.9 | 0.0580 | 2.010 |
| 13-13 | 27.5 | 0.0151 | 0.14 | 28.3 | 0.0157 | 37.9 | 0.0597 | 2.010 |
| Average | (25.2) | (0.0135) | (0.09) | (28.5) | (0.0160) | (37.5) | (0.0525) | (2.000) |

^aThe tensile properties in parentheses are averages for replicate specimens.

TABLE 4—Tensile properties of FM 300K adhesive at 10⁻⁶/s strain rate.

| Specimen I.D. | Strain Energy Density Method | | | 0.2 % Offset Method | | Tensile Strength (MPa) | Rupture Strain | Elastic Modulus (MPa) |
|-------------------------------------|------------------------------|--------------|------------|----------------------|--------------|------------------------|----------------|-----------------------|
| | Yield Strength (MPa) | Yield Strain | Offset (%) | Yield Strength (MPa) | Yield Strain | | | |
| Dry/cold environment: 15 % RH/-15°C | | | | | | | | |
| 4-3 | 33.0 | 0.0121 | 0.02 | 46.3 | 0.0187 | 61.3 | 0.0308 | 2.780 |
| 1-8 | 38.5 | 0.0136 | 0.08 | 47.0 | 0.0177 | 59.5 | 0.0259 | 2.990 |
| 3-1 | 39.3 | 0.0149 | 0.05 | 48.5 | 0.0198 | 57.0 | 0.0271 | 2.720 |
| 2-8 | 42.4 | 0.0161 | 0.08 | 49.1 | 0.0198 | 63.4 | 0.0327 | 2.770 |
| 1-10 | 43.7 | 0.0163 | 0.15 | 47.4 | 0.0181 | 61.5 | 0.0281 | 2.940 |
| Average | (39.4) ^a | (0.0146) | (0.07) | (47.7) | (0.0188) | (60.5) | (0.0289) | (2.840) |
| Moderate environment: 50 % RH/30°C | | | | | | | | |
| 11-11 | 26.7 | 0.0116 | 0.05 | 35.5 | 0.0167 | 46.9 | 0.0356 | 2.400 |
| 12-21 | 28.3 | 0.0113 | 0.05 | 36.7 | 0.0159 | 47.1 | 0.0297 | 2.620 |
| 13-14 | 28.9 | 0.0137 | 0.08 | 35.1 | 0.0177 | 45.2 | 0.0369 | 2.250 |
| 2-2 | 29.9 | 0.0143 | 0.11 | 33.3 | 0.0167 | 43.8 | 0.0358 | 2.270 |
| 2-3 | 30.7 | 0.0142 | 0.10 | 35.2 | 0.0172 | 46.5 | 0.0391 | 2.330 |
| 13-15 | 31.3 | 0.0142 | 0.11 | 34.9 | 0.0167 | 46.2 | 0.0378 | 2.380 |
| 11-18 | 31.3 | 0.0142 | 0.12 | 35.0 | 0.0166 | 44.8 | 0.0294 | 2.410 |
| 12-18 | 33.3 | 0.0147 | 0.14 | 36.1 | 0.0165 | 46.2 | 0.0323 | 2.510 |
| Average | (30.0) | (0.0135) | (0.09) | (35.2) | (0.0167) | (45.8) | (0.0346) | (2.400) |
| Humid/hot environment: 85 % RH/50°C | | | | | | | | |
| 2-7 | 21.6 | 0.0122 | 0.07 | 25.5 | 0.0155 | 32.0 | 0.0650 | 1.880 |
| 9-8 | 22.0 | 0.0123 | 0.06 | 26.4 | 0.0162 | 32.7 | 0.0684 | 1.880 |
| 7-9 | 22.6 | 0.0149 | 0.14 | 24.0 | 0.0162 | 32.6 | 0.1023 | 1.670 |
| 6-8 | 23.5 | 0.0132 | 0.08 | 26.4 | 0.0158 | 31.7 | 0.0873 | 1.900 |
| 10-10 | 24.8 | 0.0149 | 0.16 | 25.5 | 0.0156 | 30.6 | 0.0517 | 1.870 |
| 1-2 | 26.7 | 0.0156 | 0.20 | 26.7 | 0.0156 | 32.9 | 0.0278 | 1.940 |
| Average | (23.5) | (0.0139) | (0.12) | (25.7) | (0.0158) | (32.1) | (0.0671) | (1.860) |

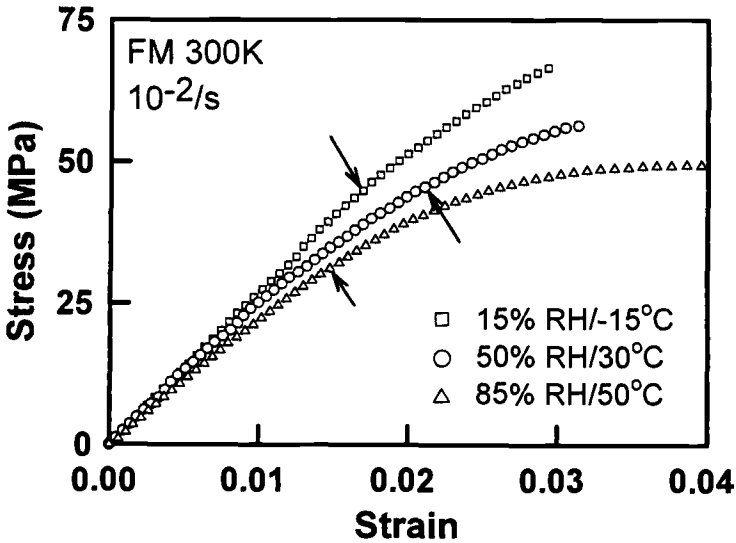
^aThe tensile properties in parentheses are averages for replicate specimens.

TABLE 5—Summary of average tensile properties of FM 300K adhesive.

| Environment | Strain Energy Density Method | | | 0.2 % Offset Method | | Tensile Strength (MPa) | Rupture Strain | Elastic Modulus (MPa) |
|-------------|------------------------------|--------------|------------|----------------------|--------------|------------------------|----------------|-----------------------|
| | Yield Strength (MPa) | Yield Strain | Offset (%) | Yield Strength (MPa) | Yield Strain | | | |
| | $10^{-2}/s$ strain rate | | | | | | | |
| Dry/cold | 43.3 | 0.0149 | 0.05 | 56.4 | 0.0209 | 69.9 | 0.0302 | 3.010 |
| Moderate | 45.7 | 0.0201 | 0.27 | 41.3 | 0.0176 | 57.4 | 0.0328 | 2.600 |
| Humid/hot | 29.8 | 0.0142 | 0.08 | 36.1 | 0.0181 | 48.5 | 0.0364 | 2.220 |
| | $10^{-4}/s$ strain rate | | | | | | | |
| Dry/cold | 48.3 | 0.0176 | 0.06 | 56.9 | 0.0219 | 65.6 | 0.0283 | 2.830 |
| Moderate | 35.4 | 0.0148 | 0.11 | 39.3 | 0.0170 | 52.0 | 0.0317 | 2.590 |
| Humid/hot | 25.2 | 0.0135 | 0.09 | 28.5 | 0.0160 | 37.5 | 0.0525 | 2.000 |
| | $10^{-6}/s$ strain rate | | | | | | | |
| Dry/cold | 39.4 | 0.0146 | 0.07 | 47.7 | 0.0188 | 60.5 | 0.0289 | 2.840 |
| Moderate | 30.0 | 0.0135 | 0.09 | 35.2 | 0.0167 | 45.8 | 0.0346 | 2.400 |
| Humid/hot | 23.5 | 0.0139 | 0.12 | 25.7 | 0.0158 | 32.1 | 0.0671 | 1.860 |

For all combinations of environment and strain rate but one, the 0.2 % offset method overestimates the yield strength by the SED method. Given the large variety of stress-strain curves for adhesives subjected to different environments and strain rates, a single offset value cannot be expected to accurately predict the yield strength.

Figures 9–11 show the effect of environment on the stress-strain curves at $10^{-2}/s$, $10^{-4}/s$, and $10^{-6}/s$ strain rates, respectively. The arrows point to the yield strength calculated with the SED method.

FIG. 9—Effect of three environments at $10^{-2}/s$ strain rate.

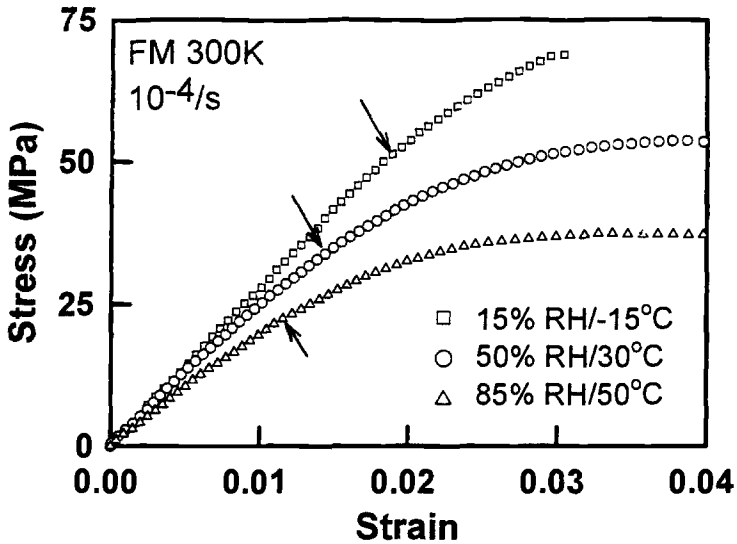


FIG. 10—Effect of three environments at $10^{-4}/s$ strain rate.

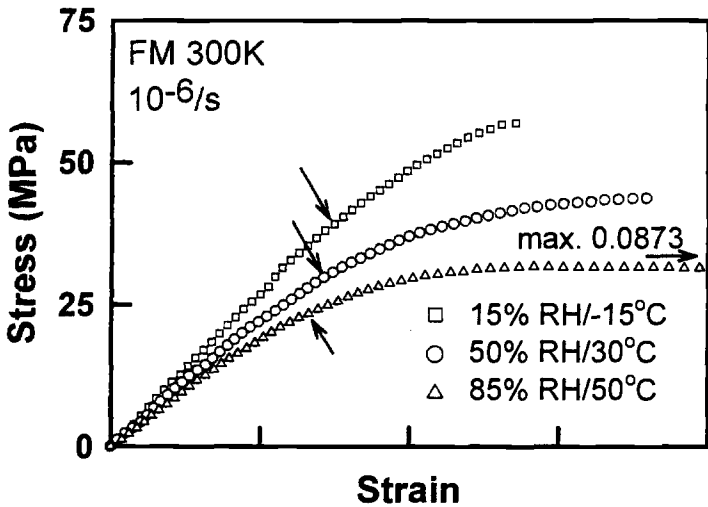


FIG. 11—Effect of three environments at $10^{-6}/s$ strain rate.

Figure 12 shows the effect of strain rate on the stress-strain curves in the moderate environment. Reducing the strain rate gave the adhesive more time to stress relax, thus lowering the yield strength. At $10^{-2}/s$, $10^{-4}/s$, and $10^{-6}/s$ strain rates, the average yield strengths are 45.7, 35.4, and 30.0 MPa, respectively, in the moderate environment and 29.8, 25.2, and 23.5 MPa, respectively, in the humid/hot environment.

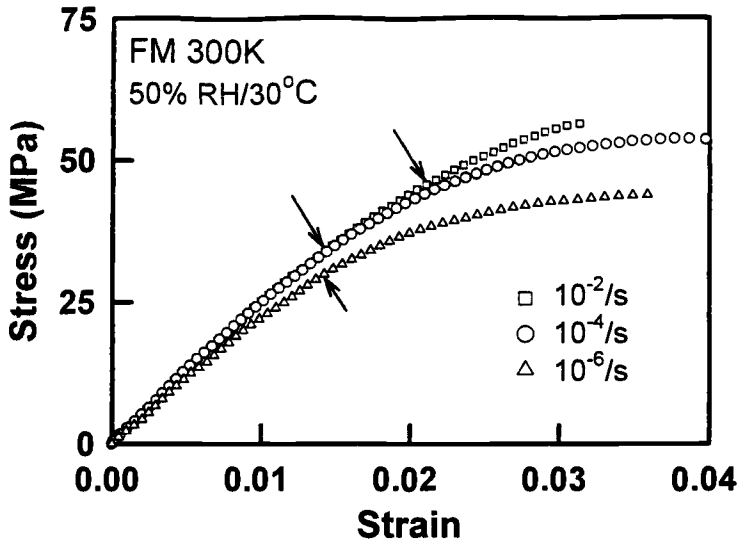


FIG. 12—Effect of three strain rates at 50 % RH and 30°C.

Effect of Adhesive Type

Table 6 shows the tensile properties of six adhesives in the dry/cold and humid/hot environments. All adhesives were tested at a $10^{-4}/s$ strain rate. On average, the time to rupture was 6 min in the dry/cold environment and 9 min in the humid/hot environment. The tensile properties of adhesive FM 300K are averages for replicate specimens (Table 5). For the other adhesives, only one specimen was tested per environment. Nine of the twelve specimens have yield strengths and offset strains calculated with the SED method that are equal to or lower than the values from the 0.2 % offset method.

Conclusions

The following conclusions are drawn from the results of the present work:

- In tensile tests of specimens loaded in equal displacement increments, the yield strength is reached when the value of the SED falls below the lower confidence limit of the data in the linear region.
- The SED method is based on the fundamental principles of mechanics, while the offset method is based on an assumed value of strain offset.
- In 53 out of the 60 specimens tested in the present study, the yield strengths calculated with the SED method are equal to or lower than the values from the 0.2 % offset method.
- The method is also applicable to other materials that exhibit a barely discernable transition from elastic to inelastic behavior such as aluminum and high-strength steel. This expectation was verified with specimens made of 2024-T4 aluminum, 6061-T651 aluminum, and ASTM A709 HPS 690W Cu-Ni steel.

- Other applications of the SED method could include determining the onset of instability in columns and beams from records of load-displacement and moment-curvature such as: buckling, web local buckling, flange local buckling, and lateral-torsional buckling.
- The yield strength, which is the most important material property used in designing structures, should be calculated with the SED method.

TABLE 6—Tensile properties of six adhesives at 10^{-4} /s strain rate.

| Adhesive | Strain Energy Density Method | | | 0.2 % Offset Method | | Tensile Strength (MPa) | Rupture Strain | Elastic Modulus (MPa) |
|---|------------------------------|--------------|------------|----------------------|--------------|------------------------|----------------|-----------------------|
| | Yield Strength (MPa) | Yield Strain | Offset (%) | Yield Strength (MPa) | Yield Strain | | | |
| Dry/cold environment: 15 % RH/-15°C; strain rate 10^{-4} /s | | | | | | | | |
| 3M 3559 | 40.9 | 0.0206 | 0.13 | 43.2 | 0.0221 | 46.4 | 0.0245 | 2,120 |
| Adh 96 | 44.5 | 0.0201 | 0.20 | 44.5 | 0.0201 | 67.5 | 0.0420 | 2,460 |
| Adh 98 | 47.2 | 0.0190 | 0.10 | 53.7 | 0.0224 | 72.0 | 0.0407 | 2,620 |
| FM 300K | 48.3 | 0.0176 | 0.05 | 56.9 | 0.0219 | 65.6 | 0.0283 | 2,830 |
| II-3H ^a | 52.2 | 0.0225 | 0.22 | 49.6 | 0.0210 | 70.7 | 0.0441 | 2,570 |
| Adh 14 ^a | 62.3 | 0.0278 | 0.47 | 47.6 | 0.0193 | 71.1 | 0.0356 | 2,700 |
| Humid/hot environment: 85 % RH/50°C; strain rate 10^{-4} /s | | | | | | | | |
| 3M 3559 | 16.8 | 0.0187 | 0.20 | 16.8 | 0.0178 | 20.0 | 0.0379 | 1,000 |
| Adh 96 | 22.6 | 0.0134 | 0.05 | 26.7 | 0.0169 | 34.9 | 0.1065 | 1,750 |
| Adh 98 | 29.7 | 0.0157 | 0.11 | 31.6 | 0.0171 | 39.4 | 0.0318 | 2,030 |
| FM 300K | 25.2 | 0.0135 | 0.09 | 28.5 | 0.0160 | 37.5 | 0.0525 | 2,000 |
| II-3H ^a | 29.5 | 0.0206 | 0.30 | 27.5 | 0.0181 | 33.3 | 0.0926 | 1,680 |
| Adh 14 | 31.1 | 0.0172 | 0.14 | 32.0 | 0.0179 | 39.8 | 0.0368 | 1,970 |

^a All but three specimens have yield strengths and offset strains calculated with the SED method that are equal to or lower than the values from the 0.2 % offset method.

Acknowledgments

The first author acknowledges the financial support from the Thailand Research Fund.

References

- [1] Albrecht, P., Mecklenburg, M. F., and Evans, B. M., "Screening of Structural Adhesives for Application to Steel Bridges," Report No. FHWA/RD-84/037, NTIS Report No. PB86 142601, Federal Highway Administration, McLean, VA, 1985.
- [2] Albrecht, P., You, J. M., Albrecht, M., and Eley, K., "Tensile Properties of FM 300K Adhesive," Final Report, Department of Civil Engineering, University of Maryland, College Park, MD, 1998.
- [3] Albrecht, P., You, J., and Albrecht, M., and Eley, K., "Tension Testing of Thin Bulk Adhesive Specimens," *Limitations of Test Methods for Plastics, ASTM STP 1369*, J. S. Peraro, Ed., ASTM International, West Conshohocken, PA, 2000, pp. 72-92.
- [4] Nadai, A., *Theory of Flow and Fracture of Solids*, McGraw-Hill, New York, 1950.
- [5] Bauwens, J. C., "Yield Condition and Propagation of Lüder Lines in Tension-Torsion Experiments on Polyvinyl Chloride," *Journal of Polymer Science*, Vol. 8, 1970, pp. 893-901.
- [6] Sultan, J. N. and McGarry, F. J., "Effect of Rubber Particle Size on Deformation Mechanisms

- in Glassy Epoxy," *Polymer Engineering and Science*, Vol. 13, No. 1, 1973, pp. 29–34.
- [7] Veis, A., *The Macromolecular Chemistry of Gelatin*. Academic Press, New York, 1964.
- [8] Gordon, J. E., *Structures: Or Why Things Don't Fall Down*. Da Capo Press, subsidiary of Plenum Publishing Corporation, New York, 1978.
- [9] Ishida, H., "Development of Polybenzoxazines: A New Class of High Performance, Ring-Opening Phenolic Resins with Superb Balance of Physical and Mechanical Properties," *Proceedings, International Composites Expo '98*, Nashville, TN, 1998, pp.1/14-B-8/14-B.
- [10] Ishida, H., and Allen, D. J., "Physical and Mechanical Characterization of Near-Zero Shrinkage Polybenzoxazines," *Journal of Polymer Science: Part B: Polymer Physics*. Vol. 34, 1996, pp. 1019–1030.
- [11] Sih, G. C., Michopoulos, J. G., and Chou, S. C., *Hygrothermoelasticity*, Martinus Nijhoff Publishers, Dordrecht, Netherlands, 1986.

Appendix

The reason why the authors chose to determine the yield strength with an energy method in lieu of a simple method based on geometry alone was the desire to find a master stress-strain curve for a specific adhesive. Figures 13 and 14 show two master stress-strain curves for the adhesive FM 300K, one for the effect of environment and the other for the combined effects of environment and strain rate. The advantage of using the master curve is that the stress-strain curve under any environments and strain rates could be predicted. Were this feasible, knowing the yield strength for one combination of RH, temperature, and strain rate, the yield strength for another combination could be obtained using the principles of hygrothermoelasticity [11].

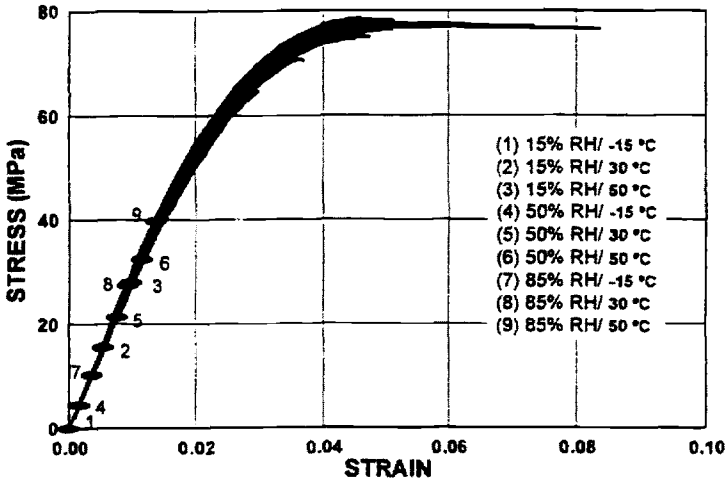


FIG. 13—Master stress-strain curve (effect of environment).

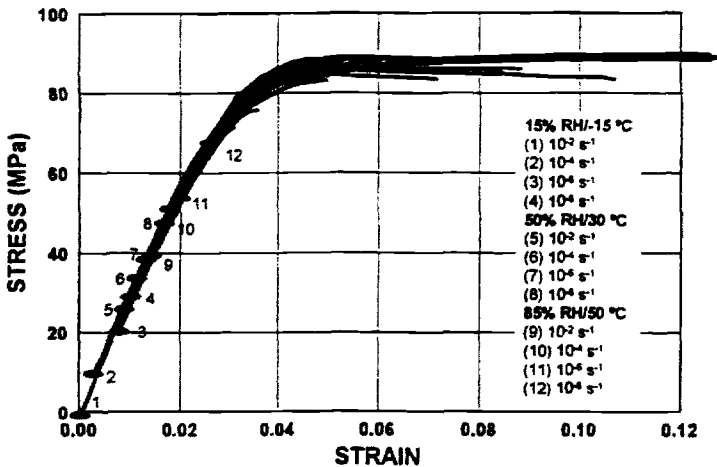


FIG. 14—Master stress-strain curve (combined effects of environment and strain rate).

Joshua C. Simón,¹ Eric Johnson,² and David A. Dillard³

Characterizing Dynamic Fracture Behavior of Adhesive Joints under Quasi-Static and Impact Loading

ABSTRACT: An experimental evaluation of the dynamic fracture properties of an automotive epoxy is presented. Pronounced stick-slip behavior was observed in both quasi-static and impact tests of aluminum and composite adherends bonded with this adhesive. An experimental technique for conducting low speed impact of adhesively bonded automotive composite joints is presented. Based on the use of a modified drop tower, mode I, II, and mixed mode values for critical energy release rate were determined to create a fracture envelope for the composite/epoxy system. Because load measurements are erratic and unreliable at higher test rates, displacement-based relationships were used to quantify these energy release rates. Displacement data were collected with an imaging system that utilizes edge detection to determine displacement profiles, end displacements, and opening displacements where applicable. Because of the resolution of the image-based approach being used, determining crack length experimentally is difficult. As a result, numerical methods based on edge detection algorithms were developed to objectively determine the crack length based on the available experimental data in mode I, II, and mixed mode I/II configurations.

KEYWORDS: fracture, impact, mode I, mode II, mixed-mode I/II, adhesive joint, composite, falling wedge test, fracture failure envelope, stick-slip, unstable crack growth, epoxy

Introduction

Modern structural design is based heavily on failure criteria to determine appropriate design envelopes. The older strength approach has been widely used for many materials and includes such criteria as the maximum shear stress and distortional energy theories [1]. Fracture mechanics based design criteria are becoming increasingly popular in transportation, infrastructure, microelectronic, and biomedical applications. Fracture mechanics is making important inroads into designing with adhesive joints, where many failures in bonded structures are due to crack growth within the adhesive layer.

The fracture-based approach derives from continuum fracture mechanics theory, which claims the strength of most real solids is governed by flaws within the material [2]. To help predict this type of behavior, many test methods have been developed to determine fracture properties of adhesives. These tests are used to characterize the mode I, II, and III fracture properties of many types of material systems. In this study, the focus will be on the mode I and II characteristics of bonded joints for automotive applications.

The goal of this research was to study the fracture properties of adhesively bonded composite structures in mode I, II, and mixed-mode I/II loading to create fracture envelopes for these modes to be used in design. The main emphasis was dynamic loading of these structures, in order

Manuscript received 12 October 2004; accepted for publication 27 December 2004; published July 2005. Presented at ASTM Symposium on Advances in Adhesives, Adhesion Science, and Testing on 4-6 October 2004 in Washington, DC.

¹ Mechanical Engineering, Virginia Tech, Blacksburg, VA 24061.

² Professor Emeritus of Aerospace and Ocean Engineering, Virginia Tech, Blacksburg, VA 24061.

³ Professor of Engineering Science and Mechanics, Virginia Tech, Blacksburg, VA 24061.

to obtain information relevant for crash-worthiness, but quasi-static testing was also conducted to provide a means of comparison with dynamic data. Because of the pronounced stick-slip nature of the fracture events even under quasi-static loading, useful insights into dynamic crack propagation were also obtained from these slower tests. In addition to the composite adherends, aluminum adherends were also used as a baseline for comparison in some cases.

The prescribed loading modes were accomplished using double cantilever beam (DCB) (mode I), end-loaded split (ELS) (mode II), and single leg bend (SLB) (mixed-mode I/II) geometries. A screw-driven load frame was used for quasi-static loading, and a modified drop tower and high-speed video camera were used to collect dynamic data. Edge detection algorithms were developed to objectively determine the debond location and energy release rate for the dynamic tests.

Specimen Preparation and Test Setup

Materials

At the request of the sponsor, the adherends chosen for the testing were comprised of MTM49/CF0501 woven fiber sheets (T300B-40B) manufactured by Advanced Composites Group (Tulsa, OK). This material is orthotropic and is a plain weave balanced fabric. Pacific Composites Inc. (San Clemente, CA) then fabricated this material into composite panels of the desired lay-up with 42 % resin content. Panels of 12 and 36 ply composites were produced, with thicknesses of approximately 2.8 and 8.5 mm, respectively. The panels consisted of woven plies oriented at (0/90) and (45/-45) angles in an alternating fashion. Aluminum adherends were also used as control adherends to provide a means of comparison for the mode I composite data. These adherends measured $25 \times 6.4 \times 254$ mm. The adhesive used was PL731SI, a two-part epoxy system produced by Sovereign Specialty Adhesives Inc. (Chicago, IL). The resin and hardener were mixed at a 4:1 ratio, and an elevated temperature cure was used at the recommendation of the supplier.

All specimens were constructed in a bonded-beam configuration. Aluminum adherends were used in both the static and dynamic DCB configurations, and the composite adherends were used in the static and dynamic DCB and dynamic ELS and SLB configurations. Aluminum (6061) adherends were P2 etched to provide an adequate bonding surface and a bondline of either 0.8 mm or 0.5 mm was used. Because they were shipped in panel form, the composite adherends were bonded in 300×300 mm sheets. Each surface was abraded and then cleaned with acetone prior to bonding. The bondline was again set using either 0.8 mm or 0.5 mm wire at the center and 20 mm from both ends of the composite panels. Initially, this wire was only placed at the ends of the panels, but this resulted in inconsistent bondlines due to deformation at the center of the composite panels. Once the bondline thickness was set, a thermocouple was added to the center of the specimen to monitor the bondline temperature profile.

The adhesive was then applied to the center of the panel, and an upper panel was pressed on, forcing the adhesive toward the panel's edge. Originally, the sandwiched panels were then clamped using large c-clamps at all four corners. Aluminum plates were also added when bonding the thinner 12 ply panels to prevent bowing from the applied force. Significant bondline thickness variations were found using this method. As a result, a 400 mm platen press was utilized to provide a more consistent clamping force of approximately 20 kN.

Both the aluminum and composite specimens were cured using the same heating process. In each case, the specimens or panels were placed in an oven or between platens set at 210°C to

provide a steep heating gradient as recommended by the manufacturer to improve adhesive toughness. A temperature of 210°C was chosen because it was the upper limit of the temperature range of the available equipment, and it is similar to temperatures experienced during the paint bake process. Once the cure temperature of 127°C was reached at the bondline, the specimens were removed from heat and allowed to cool at room temperature. This procedure allowed the specimens to remain within 10°C of the cure temperature for at least 5 min (depending on the adherend type and thickness) to ensure full curing. Once cured, the sides of the aluminum specimens were ground on a sanding wheel to remove adhesive spew, and composite specimens were cut into 25 × 254 mm strips using a Felker (Olathe, KS) 41AR saw with a diamond blade and water cooling.

The precracking process is slightly different between the aluminum and composite specimens. In both cases, a hardened stainless steel wedge was used to drive the crack into the specimen until it reached 50–55 mm in length for the DCB specimens and 98–100 mm for the ELS and SLB geometries to meet the length criterion for such configurations. Aluminum specimens were precracked at room temperature, but due to the unstable crack growth, a C-clamp was placed at 50 mm to force the crack to arrest. When using the same method for precracking the bonded composite specimens, however, subsequent testing resulted in interlaminar failures within composite adherends. By serendipity, cracks extending from precracks created in hot specimens were found to remain within the adhesive layer, whereas precracking of cold specimens invariably led to fractures propagating within the composite adherends. Composite specimens were heated in an oven at 200°C for 10 min prior to precracking. Precracks were again induced using the stainless wedge, but in this case the C-clamp was not necessary as the crack grew stably due to the elevated temperature of the adhesive layer. The reason for the ability to induce desired cohesive fractures within the adhesive layer in heated specimens is still not understood, although differences in residual stress or crosslinking are possible. Of particular interest is the fact that if cracks did propagate into the composite adherends, the observed fracture energies were less than a third of those found for cohesive cracks within the adhesive layer.

Once DCB specimens were precracked, size 8–32 holes were drilled and tapped for end blocks in the case of both the aluminum and the composite adherends. A paper ruler was then attached to static DCB specimens for crack length measurement, and Wite-Out® (Milford, CT) typewriter correction fluid was applied to dynamic specimens to provide contrast to aid in edge detection. Due to the test setup, SLB specimens were trimmed after precracking such that one adherend was approximately 45 mm longer than the other. Correction fluid was also applied to ELS and SLB specimens, again for edge detection purposes, but because of the loading method, no end blocks were required for these geometries.

Test Setup

Static Double-Cantilever Beam—Static double-cantilever beam testing was conducted using ASTM D 3433. An Instron 4500 series test frame (Canton, MA) with a 5 kN load cell was used for this testing. All data were collected using custom software written with the National Instruments' LabVIEW™ software (Austin, TX). Specimens were loaded into the test frame, and a constant opening displacement rate of 1 mm/min was applied.

Crack length was measured visually using the paper ruler that was bonded to the specimen during the preparation phase. Load and opening displacement were collected using the Instron's built-in data acquisition system. Upon crack propagation, the load was allowed to plateau before

the crack length was recorded. The only deviation from the ASTM method was that specimens were not intentionally unloaded between crack propagation events. Instead, the large crack propagation during the stick-slip behavior effectively reduced the load to a small fraction of the original level, as will be discussed in further detail in the results section.

Dynamic Testing—All dynamic tests were conducted using a Dynatup drop tower (Canton, MA) and Kodak Ecta Pro EM model 1012 high speed imaging system (San Diego, CA). Each geometry uses a custom mounting system that provides the desired loading for each configuration. Load was applied in each case by either polycarbonate wedges or a round-tipped steel tup mounted to the weighted sled on the drop tower, which rides on linear bearings to reduce frictional effects. The sled was dropped from a height of approximately 0.7 m, reaching a velocity of 3.7 m/s before striking the specimen.

The Kodak Ecta Pro uses a 192×239 pixel NMOS array with a spectral response of 400–1000 nm. This system is capable of 256 levels of grey and can store up to 4800 images. Full frame images can be recorded at rates of up to 1000 frames per second, and split frame recording can be done at up to 12 000 frames per second. For dynamic DCB and ELS tests, the record rate was set at 2000 frames per second with an exposure of 1/2000 second to capture as many images as possible, while maintaining an adequate image frame.

Dynamic DCB—Dynamic DCB specimens were mounted vertically in the drop tower and tested in a “falling wedge” configuration as shown in Fig. 1. This “falling wedge” method was originally developed by Xu et al. [3]. Load was applied to the specimen end by two polycarbonate wedges attached to the drop tower sled. These wedges strike ball bearing rollers mounted on pins through the loading blocks, spreading the beams apart and creating mode I loading, as shown in the schematic in Fig. 1.

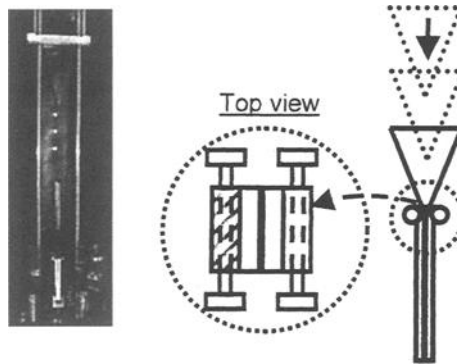


FIG. 1—Dynamic DCB test configuration.

As previously mentioned, all DCB test data were collected visually using the high speed imaging system set at 2000 frames/s. No load or displacement measurements were physically made on the specimen. There were two main reasons this was done for the case of mode I loading. First, as mentioned by Blackman et al., meaningful load measurement is not possible at high test rates due to wave propagation within test specimens as well as vibration of the adherends [3]. This creates resonances in the load train, causing excessive noise that inhibits

collection of meaningful load values. Also, because of the high test rates, crack length cannot be measured in the manner used for static DCB testing due to the rate of crack growth. The displacement profile and opening displacement are deduced from the image data, and all other parameters such as crack length, crack velocity, and energy release rate are calculated in the analysis.

Dynamic ELS—End-loaded split specimens were also tested in the drop tower, but were mounted horizontally in a custom clamping fixture as shown in Fig. 2. This fixture consists of a side grooved Palmgren vise (Chicago, IL) mounted to a custom pedestal. The pedestal is constructed of 50×50 mm steel box tubing welded to 6.4 mm steel plates and is clamped to the drop tower base using 100 mm C-clamps. In this case, a hemispherically-tipped steel tup is attached to the drop tower sled and travels downward, striking the end of the specimen as shown in the schematic in Fig. 2.

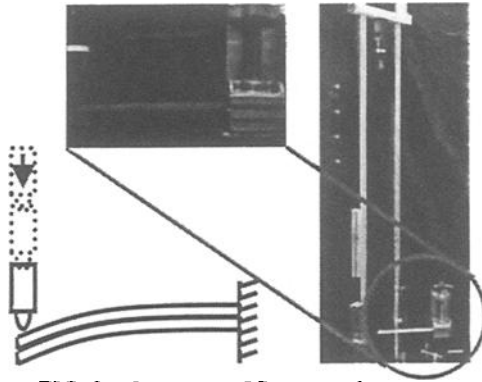


FIG. 2—*Dynamic ELS test configuration.*

Here, the imaging system is used to collect the displacement profile and end displacement of the specimens. Again, as with the case of the DCB geometry, all other parameters such as crack length and energy release rate are calculated during the analysis phase. Due to the fact that the adherends remain in contact with one another, the crack length must be calculated from adherend deflection profiles, since the crack is not apparent in the collected images. Other means to improve crack detection based on shearing at the debond are being investigated for future work.

Dynamic SLB—The single leg bend specimens were also mounted horizontally in the drop tower using the aforementioned fixture, and load was applied using the hemispherically-tipped tup. The difference between the SLB geometry and the ELS geometry is that one adherend is shorter (45 mm) than the other, so the load is only applied to the lower adherend. This results in a mixed mode loading situation that is globally equivalent to 57 % mode I and 43 % mode II. The tup strikes the longer adherend, as shown in the schematic in Fig. 3, which is mounted on the bottom side, creating both opening and shear loading.

Data collection in this case included the displacement profile as well as the opening displacement, which were both used in determining the crack length. As previously mentioned, the precrack length criterion was 0.55–0.6 times the fixed length to preserve stable crack growth.

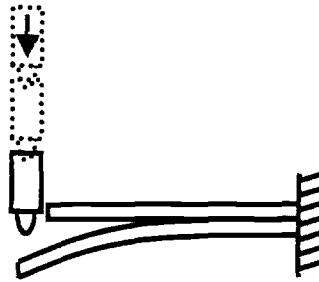


FIG. 3—Dynamic SLB test configuration.

Analysis

Static DCB Analysis

As previously mentioned, static DCB tests were conducted using the ASTM standard D 3433 procedure on an Instron 4500 series test frame. A corrected beam theory approach from Blackman et al. was used to analyze these data and gather mode I energy release rate values [4]. This method uses the measured load and opening displacement to calculate the energy release rate at each measured crack length [5]. The equation for the static mode I energy release rate is:

$$G_{Ic} = \frac{3P\Delta}{2B(a + \chi)} \frac{F}{N} \quad (1)$$

where F and N are correction factors for large deflections and stiffening of the beams due to the loading end blocks. Δ is the measured opening displacement, P is the applied load, B is the specimen width, and χ is a length correction factor for the compliance. The correction factor for the compliance is necessary because this method is based on simple beam theory for a perfectly cantilevered beam and thus underestimates the compliance because the beam is not perfectly built in at the root of the crack tip.

Dynamic DCB Analysis

All dynamic DCB test data were collected using the high-speed imaging system and then outputted as an image for every moment in time recorded. National Instruments LabVIEW software was used to gather opening displacement data from these images. An edge detection code written by Brown was used to scan the images and to find the x and y coordinates along each beam, as shown in Fig. 4 [6]. This code collects data every 10 pixels (~ 4 mm) along an image and calculates the opening displacement, δ , as the difference between the y coordinates of the upper and lower beams (y_1 and y_2) at numerous points along the specimen. Half the beam thickness is subtracted from this value to give the opening displacement at each point along the sample.

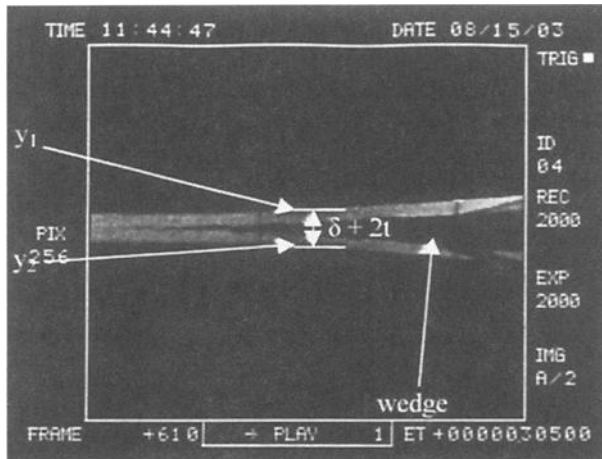


FIG. 4—Parameters collected with edge detection program.

The edge detection data for all images were then imported into an analysis program that scales the displacements from pixels to meters. A nonlinear fit was then applied to the data from each image (each instant in time) in the form of:

$$\delta = \frac{2P}{3E_f I} (-(a-x)^3 + 3a(a-x)^2) \text{UnitStep}[x-a] \quad (2)$$

where δ is the opening displacement at a given x , P is the calculated load, E_f is the modulus of elasticity of the adherend material, I is the moment of inertia of the adherends, a is the crack length, and x is the position along the beam [6]. The crack length can then be extracted and used to calculate the energy release rate using an equation developed by Blackman et al.[7]:

$$G_I = \frac{9\Delta^2 E_f I}{4Ba^4} F \quad (3)$$

where Δ is the opening displacement at the load application point, B is the specimen width, and F is a correction factor for large deflection.

This analysis method was successfully used by Brown, and as a result very few issues had to be resolved to obtain acceptable results for the chosen adhesive/composite system. The unstable crack growth encountered with the chosen system created problems with the analysis resolution, specifically with the nonlinear fit used to determine the crack length. This analysis resolution, if set too high, led to extremely long analysis times, however, if set too low, test data were not properly fitted, leading to incorrect crack length predictions. Issues were also encountered with the stiffer specimens (36 ply composite and aluminum adherend), as less deflection was required for crack propagation, resulting in less data per test run, as well as more sensitivity to noise in the test data. This increased debonding rate as a result of the relative stiffness of the aluminum and 36 ply adherends exceeded the capability of the imaging system in some cases, resulting in lost data, specifically at crack initiation. This issue could be resolved by using an imaging system with a higher sampling rate or by using more flexible adherends.

Dynamic ELS Analysis

End-loaded split data were collected using the high-speed imaging system and were imported into an analysis program and scaled in the same fashion as the dynamic DCB data. An analysis method using a least squares fit between two equations based on beam theory that describe both the cracked and uncracked portions of the beam. Under these mode II loading conditions, however, the debond would propagate into one adherend, precluding the use of fracture data beyond the initial debond. Because of this, the debond tip locating algorithms were not needed, but have been discussed elsewhere in detail [8]. The energy release rate can be calculated using an equation developed by Blackman et al. [9]:

$$G_{II} = \frac{9\Delta^2 h^3 E_f (a + \chi_{11} h)^2}{[3(a + \chi_{11} h)^3 + (L + 2\chi_1 h)^3]^2} \frac{F}{N^2} \quad (6)$$

where Δ is the opening displacement, h is the beam thickness of the adherends, a is the crack length, E_f is the modulus of elasticity of the adhesive, L is the fixed length of the specimen, χ_1 and χ_{11} are correction factors for deflection and end-rotation of the crack tip, and F and N are correction factors for large deflections and stiffening of the beams due to the loading end blocks.

Dynamic SLB Analysis

A numerical algorithm was developed to objectively detect the crack length in the SLB specimen as well. Because the debond propagated to the interface, however, only data from the initial, known debond were used. Once the crack length was determined, the mixed-mode energy release rates were calculated using equations developed by Blackman et al. [8]:

$$G_I = \frac{12\Delta^2 h^3 E(a + \chi_1 h)^2}{[7(a + \chi_1 h)^3 + (L + 2\chi_1 h)^3]^2} \frac{F}{N^2} \quad (7)$$

$$G_{II} = \frac{9\Delta^2 h^3 E(a + \chi_{11} h)^2}{[7(a + \chi_{11} h)^3 + (L + 2\chi_1 h)^3]^2} \frac{F}{N^2} \quad (8)$$

where all parameters are as previously defined.

Results*Static DCB*

Testing on this project began with static DCB experiments on aluminum adherends. Initial testing resulted in very few data points per specimen due to unstable crack growth within the adhesive layer. Specimens were loaded until the point of crack initiation, at which time the crack would rapidly grow 40–60 mm before arresting. Issues with specimen quality resulting from inconsistent curing were also discovered. In an attempt to reduce the crack jump distance, the bondline thickness was changed from 0.8 mm to 0.5 mm. The curing process was also more closely monitored to ensure consistent curing. After these changes, three to four data points could be collected on each test specimen. It is unclear which change resulted in the increase in data points; the reduction in bond thickness was an attempt to restrict the plastic zone size and possibly the crack jump distance, but as later calculations show, it is unclear whether the plastic zone is being restricted by the 0.5 mm bondline.

Figure 5 shows the initiation energy release rates for three batches of aluminum DCB specimens with a bondline thickness of 0.5 mm. resulting in an average initiation value of the strain energy release rate of approximately 1800 J/m² and a standard deviation of approximately 110 J/m². These values were calculated by inputting load, crack length, and opening displacement values prior to crack initiation into the corrected beam theory equations previously presented. The lines shown in the figure are simply to guide the eye by connecting data points within a single test. Due to previous issues with batch-to-batch variation between test samples, three batches were tested to ensure that the final method chosen for specimen preparation reduced the variation in results. The data from these tests are sufficiently more consistent than previously collected results on samples with large bondline and cure temperature variations, leading to the conclusion that the current preparation methods are satisfactory.

The arrest values for the static DCB tests with aluminum adherends are shown in Figure 6. These values were calculated by inputting load, crack length, and opening displacement values collected following crack arrest into the corrected beam theory equations previously presented.

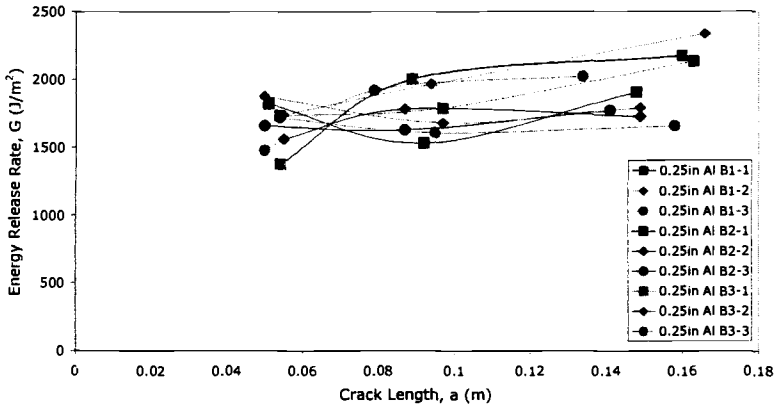


FIG. 5—Initiation SERR, static DCB on aluminum with 1 mm/min test rate.

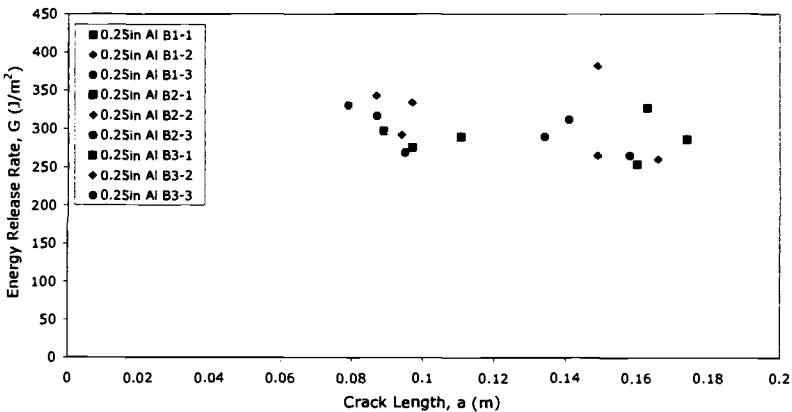


FIG. 6—Arrest SERR, static DCB on aluminum with 1 mm/min test rate.

The most notable aspect of these arrest results is the fact that the arrest values are only approximately 17 % of the initiation values as a result of the unstable crack growth. These low values are most likely due to the extreme time dependence of the chosen adhesive, along with artifacts associated with kinetic energy effects due to the rapid crack growth. Crack jump distances as great as 150 mm were observed in static DCB testing, although 40–60 mm jumps were more common. These are comparable to stick-slip results collected by Blackman et al.[7], who show jumps of up to 100 mm.

This effect of the unstable propagation can be seen in the load versus opening displacement traces collected during testing as well. One such trace is shown in Fig. 7. As the figure shows, as much as a 75 % drop in load was experienced upon crack propagation due to about 60 mm of rapid growth upon initiation.

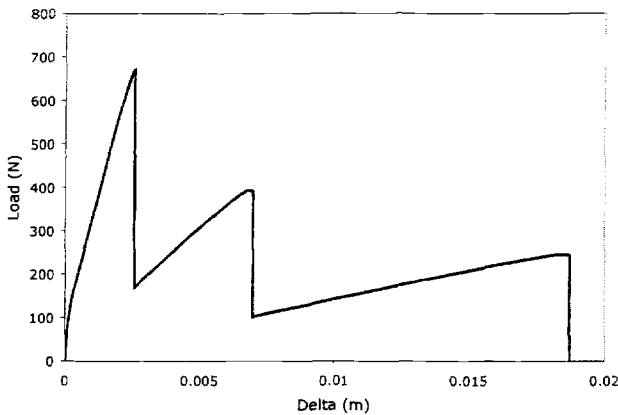


FIG. 7—Load versus time trace, static DCB on aluminum with 1 mm/min test rate.

Because of the dynamic effects resulting from the rapid propagation, the arrest values were considered to be less significant, as has been discussed in the literature. On the other hand, the initiation energy release rates are believed to be insufficient to fully characterize the behavior of the chosen adhesive, as their use could result in non-conservative designs. As a result, an average critical energy release rate based on energy methods was developed to better describe the energy absorbed during rapid crack propagation. Figure 8 shows the load versus opening displacement data from the first propagation event for the test shown in Fig. 7. Using the energies depicted by regions 1 and 2 in Fig. 8, which assumes rapid crack growth occurs at a fixed displacement, an energy balance can be characterized by the equation:

$$U_2 - U_1 = G_c(\dot{a}) \cdot \Delta A + T_{residual} + \text{dissipated energy} \tag{9}$$

where U_1 and U_2 represent the stored energy at locations 1 and 2, respectively; $G_c(\dot{a})$ is the rate dependent critical energy release rate; ΔA is the area difference; $T_{residual}$ is the residual kinetic energy; and the dissipated energy may include energy going into noise and heating the surrounding air. This equation can then be expressed in the form of an inequality for the average energy release rate associated with the debond event:

$$G_{c,av} \leq \frac{U_2 - U_1}{A_2 - A_1} \tag{10}$$

where A_1 and A_2 are the bond areas corresponding to the initial and final crack, and the inequality takes into account the ignored kinetic energy, noise, and other effects. For the example shown, the average energy release rate was determined to be approximately 400 J/m^2 , much lower than the peak value of 1720 J/m^2 , but above the arrest value of 270 J/m^2 . Although the utility of this effective fracture energy has not been demonstrated, it is thought to be more realistic than the initiation value for debond propagation, and less sensitive to kinetic nuances than the arrest value.

Static DCB tests were also conducted using 12 and 36 ply adherends bonded with the same adhesive. Initially, precracks immediately grew into the composite adherends rather than within the adhesive layer. Results from these tests, which indicate the interlaminar energy release rate of the composite material, are shown in Fig. 9. The average energy release rate of the composite material was approximately 550 J/m^2 , 1250 J/m^2 lower than the initiation energy release rate of the adhesive measured using the aluminum adherends.

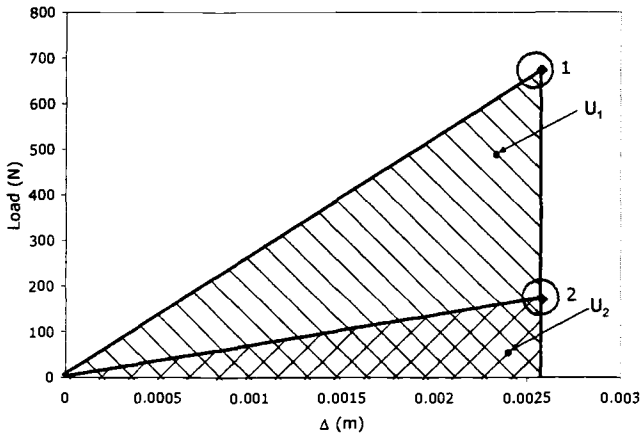


FIG. 8—Load versus time trace, load drop after first initiation.

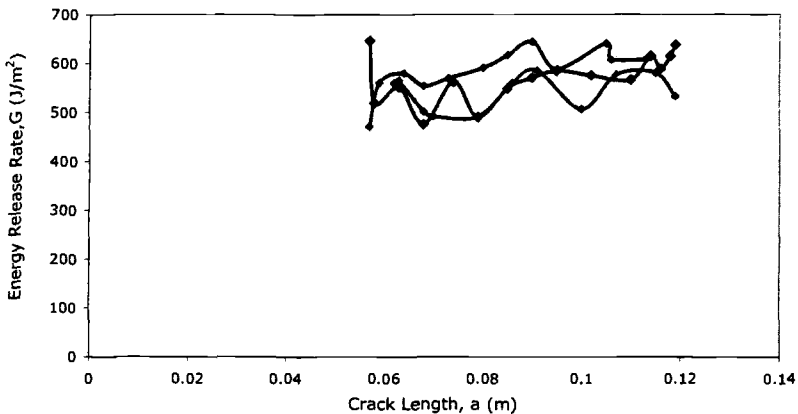


FIG. 9—Results for interlaminar crack growth within three composite adherend specimens.

Static DCB with New Precracking Technique—After trying multiple techniques to keep the crack growth within the adhesive layer, heating composite specimens prior to precracking was found to induce crack growth within the adhesive material. The final preheating procedure entails placing specimens in an oven set at 200°C for 10 min and then immediately precracking them at an elevated temperature as detailed in the specimen preparation section of this thesis.

No explanation has been found as to why this preheating procedure works. Possibly the heating of the adhesive above its T_g during the preheating makes it softer and more rubbery, thus reducing the fracture energy necessary to propagate the crack within the adhesive layer. This may also cause further curing of the adhesive, thus lowering the fracture toughness, which may explain why crack propagation remains in the adhesive layer during testing at room temperature.

Results for static DCB tests on bonded 12 ply and 36 ply adherends using the heated precrack procedure are shown in Fig. 10. Bonded 36 ply specimens were made with a 0.5 mm bondline thickness, and bonded 12 ply specimens were made with both 0.5 mm and 1 mm bondline thicknesses to investigate the effect of the bondline thickness on the fracture energy. Based on preliminary bulk tension (dogbone) and compact tension testing, the plastic zone radius is 0.26 mm, which could indicate that the plastic zone is being restricted by the bondline in the case of the 0.5 mm bondline thickness. No significant difference was found between the 1 mm and 0.5 mm bondline thickness specimens, leading to the conclusion that the 0.5 mm thickness is not significantly constricting the plastic zone. Two batches of each bondline thickness were tested for both adherend thicknesses, again looking at the batch to batch variations. Unstable crack growth is evident, as in the case of the aluminum adherend specimens, resulting in rapid crack propagation and very few data points per specimen.

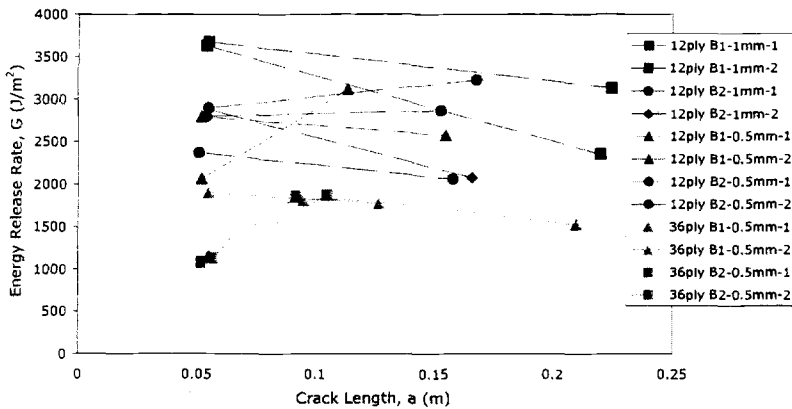


FIG. 10—Static DCB initiation energy release rates, bonded 12 and 36 ply composite specimens.

Initiation energy release rates averaged 2700 J/m² for the bonded 12 ply specimens and 1600 J/m² for the bonded 36 ply specimens. These values are as much as 2150 J/m² greater than that of the composite material, yet the crack propagation remains in the adhesive layer regardless of the fact that the composite is actually the “weakest link” [10].

The bonded 12 ply specimens exhibited higher initiation energy release rates, as well as longer crack jumps between propagation points. Several hypotheses were developed to explain this behavior. The first suggested that this behavior is a result of the difference in stiffness

between the two thicknesses of composite adherends. The stiffness of each adherend type and thickness were calculated, and the results of this study are shown in Table 1.

TABLE 1—*Stiffness of aluminum and bonded 12 and 36 ply composite adherends.*

| Material | Stiffness (N*m) |
|------------------|-----------------|
| Aluminum | 38 |
| 12 ply composite | 2 |
| 36 ply composite | 50 |

As Table 1 shows, the 12 ply adherends are significantly less stiff than the 36 ply and aluminum adherends, leading to the conclusion that the stiffness differences could in fact be causing the variation in test results. Evidence in the literature was found that supported this claim, showing that stiffer adherends led to a higher local loading rate at the crack tip, even when specimens were loaded at the same rate globally [11]. This lower local loading rate in the thinner, less stiff, adherends leads to a larger and more defined plastic zone, thus requiring a higher amount of energy to initiate the crack. The plastic zone size for both the 12 and 36 ply adherends was calculated as 0.42 mm and 0.25 mm respectively, using the Dugdale method, further showing that the 12 ply adherends are being loaded slower locally, leading to a larger plastic zone as well as a higher energy release rate [12].

Dynamic DCB

Dynamic DCB tests were also conducted on both aluminum and composite adherends using the aforementioned drop tower. The results from the tests on aluminum are shown in Fig. 11, and those on composite are shown in Fig. 12. These figures show the apparent energy release rate, sampled at 2000 frames/s and not necessarily the discrete initiation and arrest energy release rates. This apparent energy release rate is the applied energy release rate, not a critical value, over the duration of the test and possibly includes dynamic effects due to the test rate.

In the case of these dynamic tests, the unstable crack growth created problems in capturing the critical energy release rates, as well as in providing sufficient data to calculate crack velocities. Because of the rapid crack propagation, data were lost as the crack velocity exceeded that which the available imaging system was capable of recording. A system with a higher sampling rate could capture more data leading up to initiation, possibly resulting in higher calculated critical energy release rates as well as more complete crack velocity data, showing definite initiation and arrest points.

Because of the number of data points collected per test, the sampled results are difficult to interpret when plotted together. One significant difference between the aluminum and composite results is the fact that there are peaks and valleys in the composite data, whereas the aluminum results are fairly constant. This disparity is most likely an indication of stick-slip crack growth in the case of the bonded 12 ply composite adherends due its lower relative stiffness. Also, there is an apparent convergence in energy release rate values in Fig. 11 as the crack length increases. This is possibly due to lost data as a result of an insufficient sampling rate. This hypothesis could be verified by using a camera with a higher sampling rate and comparing the results to those shown in Fig. 11.

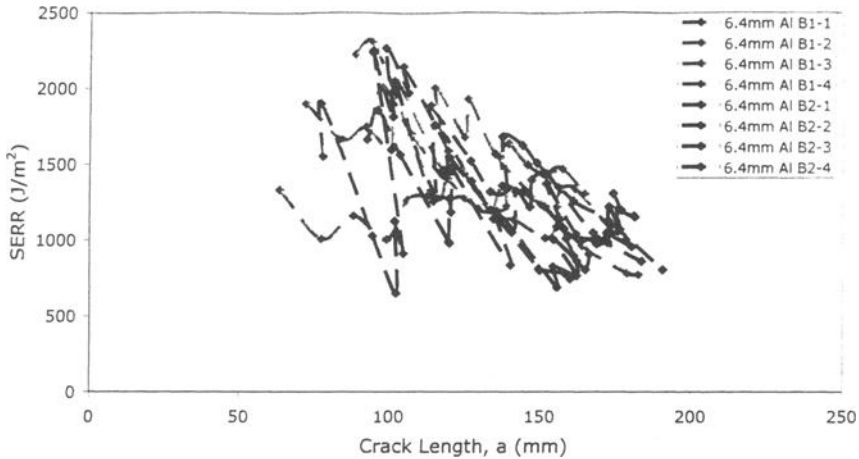


FIG. 11—Dynamic DCB with 6.35 mm aluminum adherends.

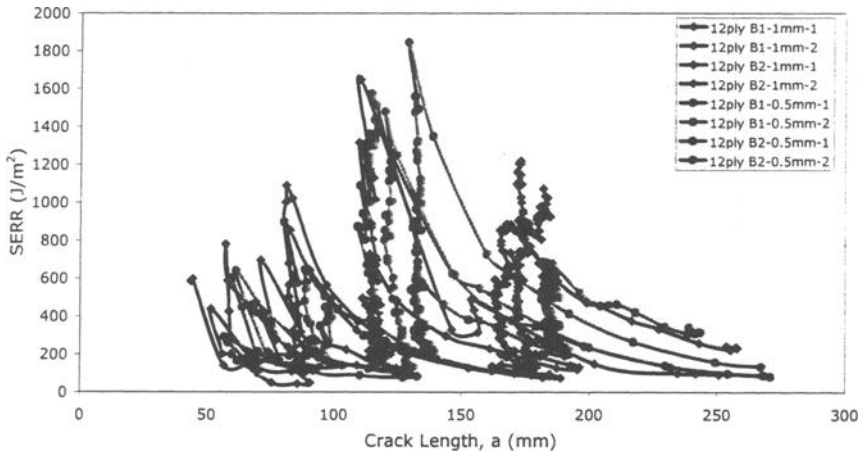


FIG. 12—Dynamic DCB with 12 ply composite adherends.

Because of the flexibility of the 12 ply composite adherends, the local loading rate is reduced enough to allow plastic zones to form ahead of the crack tip, causing unstable growth, even at this high global loading rate. Figure 13 shows the crack velocity versus time and energy release rate versus time for a single test for the 12 ply composite adherends.

The velocity data indicate two possible arrest points for the bonded 12 ply adherend test, corresponding to peaks in the energy release rate data. Because the velocities are calculated using a finite difference and are not instantaneous, strong claims cannot be made about crack arrests based on the information shown in the figures. With a higher speed camera and a method to obtain instantaneous velocity data, it would be possible to determine if there are in fact crack arrests during dynamic DCB tests. The results shown do indicate that the crack velocity is changing and peaks in energy release rate correspond to valleys in the crack velocity as expected.

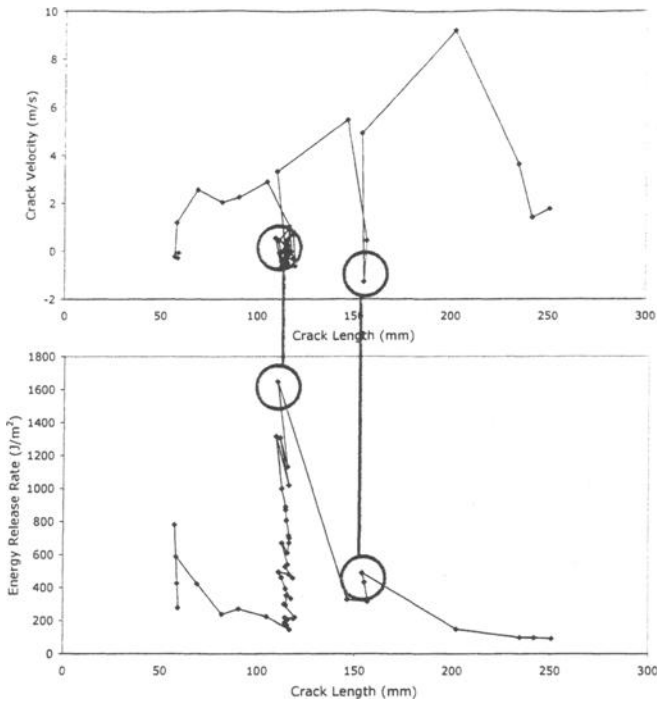


FIG. 13—Dynamic DCB with 12 ply composite adherends, crack velocity, and energy release rate versus time from a single test.

To provide a means for comparison of the dynamic data to static DCB results, Fig. 14 shows only the peaks of the dynamic DCB results for the bonded 12 ply adherends, which may or may not represent the actual critical energy release rates. The peaks in energy release rate may or may not have been captured because the data collection was limited to 2000 frames/s by the imaging system. These results could be verified by using a higher speed imaging system to capture more data points per test.

The average “peak” energy release rate for these dynamic tests is 1000 J/m^2 , which is significantly lower than the static initiation energy release rate of 2700 J/m^2 . This reduction in energy release rate may be due to the sampling rate of the imaging system, but could also be due to a smaller plastic zone being formed at the crack tip as a result of the higher loading rate, both globally and locally. Approximate plastic zone size for the static DCB was 0.42 mm , whereas the dynamic DCB plastic zone size was 0.16 mm . These values were calculated using the previously mentioned Dugdale method with the yield stress value of 55 MPa deduced from bulk tensile testing and the stress intensity factors calculated using the average measured static and dynamic DCB energy release rates.

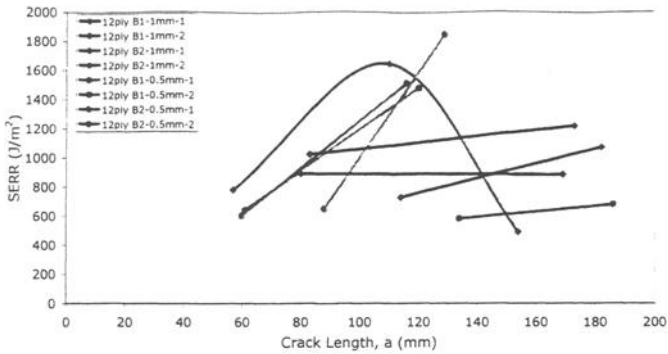


FIG. 14—Peak energy release rates—bonded 12 ply dynamic DCB.

Mode II and Mixed Mode I/II

Dynamic ELS testing was also conducted to obtain mode II energy release rates. These tests were run using the drop tower configured as described in the test setup section of this paper. Only one data point was collected per specimen because the crack traveled into the composite material after propagating from the precrack in the adhesive layer. The average initiation energy release rate for the 0.5 mm bondline thickness was 3100 J/m², and the average value for the 1 mm bondline thickness was 750 J/m². The fracture surfaces of the 1 mm thickness specimens were very non-uniform, as was the precrack, possibly leading to the low average energy release rate. There were also possible issues with the curing of the 1 mm specimens, but due to time constraints more specimens could not be made. Figure 15 shows the differences in the fracture surfaces between the 0.5 mm and 1 mm bondline thickness specimens.

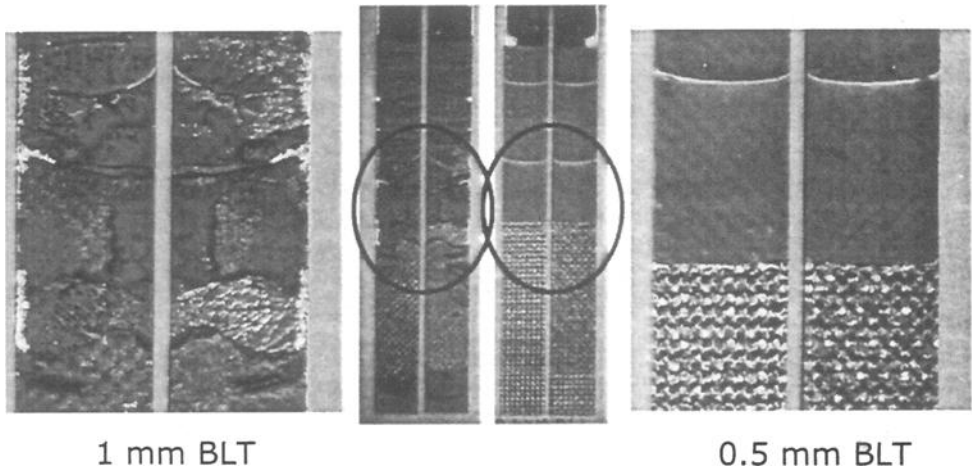


FIG. 15—Bonded 12 ply dynamic ELS fracture surfaces, 1 mm and 0.5 mm bondlines.

As Fig. 15 shows, the 1 mm bondline thickness specimen has a very non-uniform fracture surface, whereas the fracture surface of the 0.5 mm bondline thickness specimen is fairly smooth and uniform. The precrack region, noted by the circle in the image, is also very non-uniform in the case of the 1 mm bondline thickness specimen. Because the only data point collected from these tests is an initiation from this precrack, the data may be suspect due to the non-uniformity of the precrack.

Mixed Mode I/II

Preliminary dynamic SLB testing was also conducted to obtain mixed-mode data. These tests were run with symmetric specimens, which produced a mode I to mode II ratio of 1.33. This testing resulted in energy release rates on the order of 1000 J/m² for mode I and 1400 J/m² for mode II. These values, calculated using the developed analysis program, were verified to be within 10 % of values calculated by hand, as in the case of the ELS results. This agreement in results led to the conclusion that the crack length could be predicted by the analysis program. Further testing is currently underway on this geometry.

Summary and Conclusions

Static and dynamic DCB tests were run with 6.35 mm aluminum and 12 ply adherends, and 36 ply composite adherends were also tested statically. Dynamic ELS and SLB tests were also run with 12 ply composite adherends. Table 2 shows the initiation energy release rates for the static DCB and dynamic ELS and SLB testing, the peak energy release rates from dynamic DCB testing, and the energy based average energy release rates calculated for the static DCB testing.

TABLE 2—Average initiation energy release rates for static and dynamic testing.

| Mode I/II Energy Release Rates | | | |
|---------------------------------------|---------|--|--------------------------------|
| Adherend | | Peak/Initiation J/m² | Average J/m² |
| 6.4 mm Al DCB | Static | 1800 | 610 |
| | Dynamic | 1900 | N/A |
| 36 ply Composite DCB | Static | 1200 | 440 |
| 12 ply Composite DCB | Static | 2700 | 510 |
| | Dynamic | 1400 | N/A |
| 12 ply Composite ELS | Dynamic | 3100 | N/A |
| 12 ply Composite SLB | Mode I | 1000 | N/A |
| | Mode II | 1400 | N/A |

As previously mentioned, the bonded 12 ply static DCB results were significantly higher than for the aluminum and 36 ply composite adherend results due to the reduced local loading rate resulting from the lower stiffness of the 12 ply adherends. This loading rate effect was also seen in the difference between the bonded 12 ply static and dynamic results, as the lower quasi-static test rate allowed for a larger plastic zone and thus a higher initiation energy release rate. Mode II critical energy release rates were also found to be higher than mode I, as is commonly reported in the literature.

The test results were also used to construct a preliminary failure envelope, which is shown in Fig. 16. The data points represent the average critical energy release rates obtained for the mode II and mixed-mode dynamic testing and the peak values previously presented for the dynamic DCB testing. A rough failure curve was drawn through the data points to illustrate the general

region where the final loci of failure may be located, although further testing is needed to refine the results. When fully developed through further testing, the failure envelope encompassed by the loci could be used for the chosen adhesive/composite system in the same manner that the current failure criteria for design with metals are being used for design purposes.

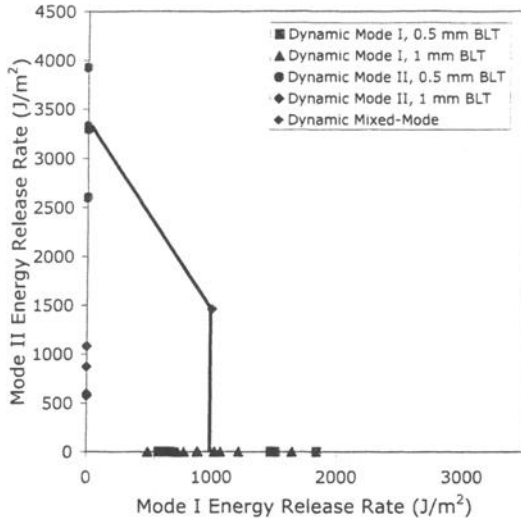


FIG. 16—Mode I/II Fracture Failure Envelope.

Along with the data collected for use in design, the methods developed to collect and analyze dynamic fracture data may lead the way for future work in this field. These image-based data collection methods provide an alternate means for gathering data in situations where the use of load cells and sensors may not be feasible due to loading rate, loading method, or test environment. The work of this paper provides the tools to collect dynamic mode I, II, and mixed-mode data using a high speed imaging system for the DCB, ELS, and SLB geometries, and can be easily adapted to other geometries, including asymmetric versions of the aforementioned tests. Future work will include the development of a method to visually obtain dynamic mode III data as well.

Acknowledgments

The authors would like to thank the project monitor, Dr. Naveen Rastogi, of the USCAR Automotive Composites Consortium for technical discussions held with him. We also acknowledge that this research is supported, in whole or in part, by the Department of Energy cooperative agreement number DE-FC05-95OR22363. Such support does not constitute an endorsement by the Department of Energy of the views expressed herein. We would also like to acknowledge the contributions of our collaborators, Prof. Rakesh Kapania and Dhaval Makhecha, for their discussions and helpful input.

References

- [1] Shigley, J. E. and Mischke, C. R., *Mechanical Engineering Design*. New York, McGraw-Hill, 2001.
- [2] Gledhill, R. A. and Kinloch, A. J., *Mechanics of Crack Growth in Epoxide-Resins*. *Polymer Engineering and Science*, Vol. 19, No. 2, 1979, pp. 82–88.
- [3] Xu, S. Y. and Dillard, D. A., "Determining the Impact Resistance of Electrically Conductive Adhesives Using a Falling Wedge Test," *Ieee Transactions on Components and Packaging Technologies*, Vol. 26, No. 3, 2003, pp. 554–562.
- [4] Blackman, B. R. K., et al., "The Failure of Fibre Composites and Adhesively Bonded Fibre Composites under High Rates of Test .2. Mode I loading - Dynamic Effects," *Journal of Materials Science*, Vol. 31, No. 17, 1996, pp. 4451–4466.
- [5] Blackman, B. R. K. and Kinloch, A. J., "Fracture Tests for Structural Adhesive Joints, in Fracture Mechanics Testing Methods for Polymers," *Adhesives and Composites*, A. Pavan, D. R. Moore, and J. G. Williams, Eds., Elsevier, Amsterdam, 2001, pp. 225–267.
- [6] Brown, S., "Time and Temperature-Dependence of Fracture Energies of Copper/Epoxy Bonds," *Engineering Science and Mechanics*, Virginia Tech: Blacksburg, VA, 2004.
- [7] Blackman, B. R. K., et al., "The Failure of Fibre Composites and Adhesively Bonded Fibre Composites under High Rates of Test .1. Mode I Loading - Experimental Studies," *Journal of Materials Science*, Vol. 30, No. 23, 1995, pp. 5885–5900.
- [8] Simón, J. C., "Response and Failure of Adhesively Bonded Automotive Composite Structures under Impact Loads," *Mechanical Engineering*, Virginia Tech. Blacksburg, VA, 2004.
- [9] Blackman, B. R. K., et al., "The Failure of Fibre Composites and Adhesively Bonded Fibre Composites under High Rates of Test .3. Mixed-Mode I/II and Mode II Loadings," *Journal of Materials Science*, Vol. 31, No. 17, 1996, pp. 4467–4477.
- [10] Lai, Y. H. and Dillard, D. A., "Using the Fracture Efficiency to Compare Adhesion Tests," *International Journal of Solids and Structures*, Vol. 34, No. 4, 1997, pp. 509–525.
- [11] Gagliano, J. M., "An Improved Method for the Fracture Cleavage Testing of Adhesively-Bonded Wood," *Wood Science and Forest Products*, Virginia Tech, Blacksburg, VA, 2001.
- [12] Yamini, S. and Young, R. J., "The Mechanical-Properties of Epoxy-Resins .2. Effect of Plastic-Deformation Upon Crack-Propagation," *Journal of Materials Science*, Vol. 15, No. 7, 1980, pp. 1823–1831.

Emmett P. O'Brien,^{1,2} Thomas C. Ward,^{2,3}

Interfacial Diffusion of Fluids in Pressure Sensitive Adhesives

ABSTRACT: Diffusion of acetone at the interface of a bonded pressure sensitive adhesive tape was measured using single frequency capacitance measurements (SFCM) and a novel interdigitated electrode sensor design. The relative concentration of acetone at the bondline as a function of distance from the edge of the specimen and exposure time was correlated to adhesion loss measured by the 90° peel test. This work suggests that these novel sensors are applicable for the study of interfacial diffusion processes, and could be extended to other coatings or adhesives in a variety of environments.

KEYWORDS: interfaces, impedance, dielectric spectroscopy, non-destructive testing, durability, diffusion, coatings, water, neutron reflectivity

Introduction

Measurements of the electrical response of polymer materials has been used to elucidate molecular relaxations [1], monitor real-time changes in the chemical and physical state in polymers brought about by crystallization [2] and cure [3], measure moisture diffusion into polymers [4], and measure the moisture content and integrity of adhesive joints [5–8]. Our research applies this technique in order to obtain detailed measurements of interfacial diffusion of fluids into an adhesive bondline.

Bulk diffusion into adhesive joints has been studied considerably [9], however little work has focused on diffusion at adhesive interfaces, largely because of the limitations of experimental techniques. Mass uptake experiments are a convenient method to study fluid absorption in adhesives. This method has been used to study interfacial diffusion by comparing the relative rates of diffusion from non-bonded or free-standing films with diffusion into the actual adhesive joint [10,11]. A disadvantage of mass uptake experiments is that the method does not provide any direct evidence of the concentration of fluid at the interface.

Additional techniques exist for measuring fluid absorption at adhesive interfaces. Fourier transform infrared spectroscopy in the multiple internal reflection mode (FTIR-MIR) is an available technique for studying diffusion at the interface. FTIR-MIR has provided direct evidence of water accumulation, and therefore adhesive debonding, at the interface [12,13]. The technique of neutron reflectivity has also shown that the concentration of absorbed fluid can be significantly greater at the interface than in the bulk adhesive [14–18].

Takahashi and Sullivan [19,20] measured the impedance in the bulk and at the interface of a coated substrate. They detected changes in the impedance attributable to adhesive debonding and

Manuscript received 5 August 2004; accepted for publication 20 December 2004; published June 2005. Presented at ASTM Symposium on Advances in Adhesives, Adhesion Science, and Testing on 4-6 October 2004 in Washington, DC.

¹ Guest Researcher, currently at the National Institute of Standards and Technology, Gaithersburg, MD 20899-8615.

² Center for Adhesive and Sealant Science, Blacksburg, VA 24061.

³ Professor, Department of Chemistry, Blacksburg, VA 24061.

the accumulation of moisture at the interface. However, limited information about the transport of moisture at the interface was obtained.

Our research builds on this limited body of work concerning diffusion at the interface of adhesive joints. We have measured the interfacial diffusion process of acetone into a bonded pressure sensitive adhesive tape by employing single frequency capacitance measurements and a novel interdigitated electrode sensor design.

Experimental

A schematic of the top-view of the sensor is shown in Fig. 1. The sensor is a series of 15 conductive interdigitated gold traces patterned into a grid and arranged in parallel with respect to the free edge of the sensor. The adhesive is applied to the sensor surface over the gold traces and is immersed in a fluid. Capacitance changes are detected by the interdigitated gold traces that act as parallel plate capacitors on the surface of the wafer, where the dielectric medium (in this case, the adhesive) resides in the trenches formed by three adjacent traces. The measured change in capacitance is proportional to the change in concentration (or volume fraction) of absorbed fluid in the adhesive [6]. Because the traces lie on the surface, changes in capacitance reflect the concentration change and diffusion processes that occur near the surface or at the interfacial region. The sensor design is novel because the surface capacitance can be measured as a function of the distance from the free edge of the applied adhesive. This is possible because each set of three gold traces have independent contact pads, which are labeled 1–10 in Fig. 1. As shown in Fig. 1, two gold traces are connected to each gold pad labeled 1–5, and a single gold trace is connected to each gold pad labeled 6–10. The capacitance can be measured between any two pads provided they are connected to a set of three adjacent gold traces. Therefore, the capacitance can be measured from the following pairs of pads, listed in order from the nearest to the most remote from the edge of the sensor: pairs 1-10, 2-9, 3-8, 4-7, and 5-6. From the aforementioned pair of pads, the capacitance can be obtained as a function of x , the distance from the free edge of the sensor. The value of x ranges from $x = 0$ mm at the free edge of the specimen to $x = 5$ mm at the center of the specimen. The values of x measured by each pair of pads, based on the distance between the free edge of the sensor and the center of the working set of gold traces, are listed below in Table 1. The deviation associated with each value of x is 0.15 mm. The deviation is based on the width of the working set of traces.

The sensor is manufactured by the Hewlett-Packard Co. The size of the sensor is 10 mm \times 30 mm. The surface of the sensor is silicon wafer having a 100 Å silicon oxide surface layer. Gold traces are 75 microns wide and rise 1.26 microns off the silicon oxide surface. The traces are composed of a 60 nm bottom layer of tantalum and 1200 nm top layer of gold. The traces are separated by 72 microns.

The 10 individual gold pads connect to a Hewlett-Packard HP4285A impedance analyzer. The impedance analyzer measures the capacitance and any other electrical property of interest as a function of frequency. Only the capacitance was considered in this work. The frequency used in these experiments was 1 MHz. Measurements below a frequency of 1 MHz had significant scatter. The automated measurement for each pair of pads was obtained using an Agilent 34970A switchbox. Shielded coaxial cables were used between the switchbox and the impedance analyzer. The IIS sensor was placed into a 14 pin edge card connector mounted to a custom board, which connects to 10 twisted parallel wires, one for each pad. The length of the wire between the switchbox and the die is approximately 0.6 m in length.

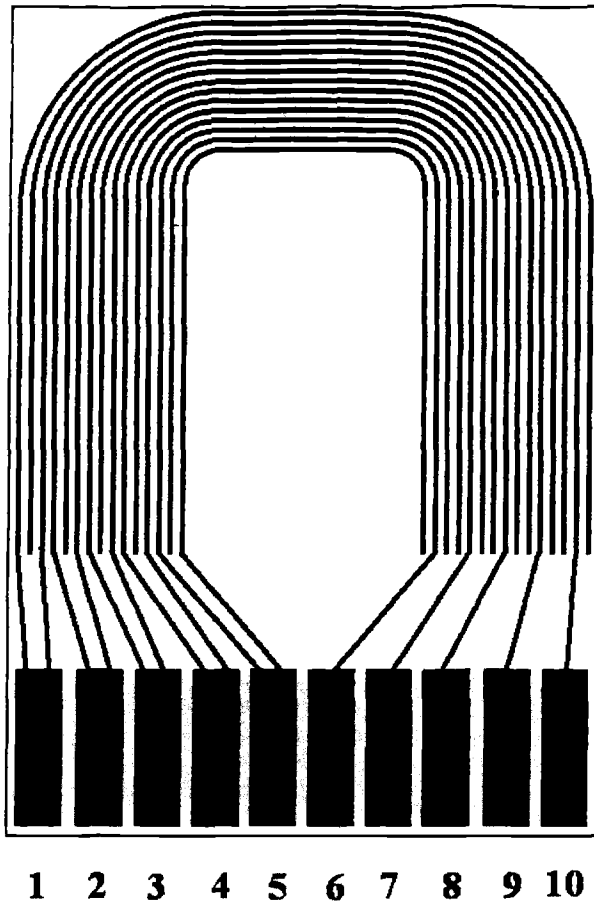


FIG. 1—Schematic (not shown to scale) of the sensor. The contact pads are labeled 1–10.

TABLE 1—The value of x measured by each pair of pads. The deviation is ± 0.15 mm.

| Pair of Pads | x (mm) |
|--------------|----------|
| 1-10 | 0.44 |
| 2-9 | 0.89 |
| 3-8 | 1.33 |
| 4-7 | 1.77 |
| 5-6 | 2.20 |

The PSA tape is manufactured by Compac Industries, Inc. (manufacturer part number 807). The backing is 51 microns thick aluminum foil with a 31 microns thick acrylic pressure sensitive adhesive. The surface of each sensor was washed with isopropyl alcohol and then blown dry with nitrogen prior to applying the pressure sensitive adhesive tape. Tests were conducted at room temperature using acetone as the liquid.

A schematic of the environmental chamber is shown in Fig. 2. A small glass bottle (approximately 40 mL) was utilized as the fluid reservoir. The sensor is partially submerged in the fluid reservoir and is fixed in place by a plastic lid fabricated with a silicon rubber top. The silicon rubber top has a slit which acts as a soft holding clamp that the sensor passes partly through. The sensor contact pads sit above the silicon rubber top and the coated interdigitated gold traces lie below in the sealed chamber formed by the lid and vial. Evaporation was slow, and no appreciable reduction in the acetone level was noticeable after a week.

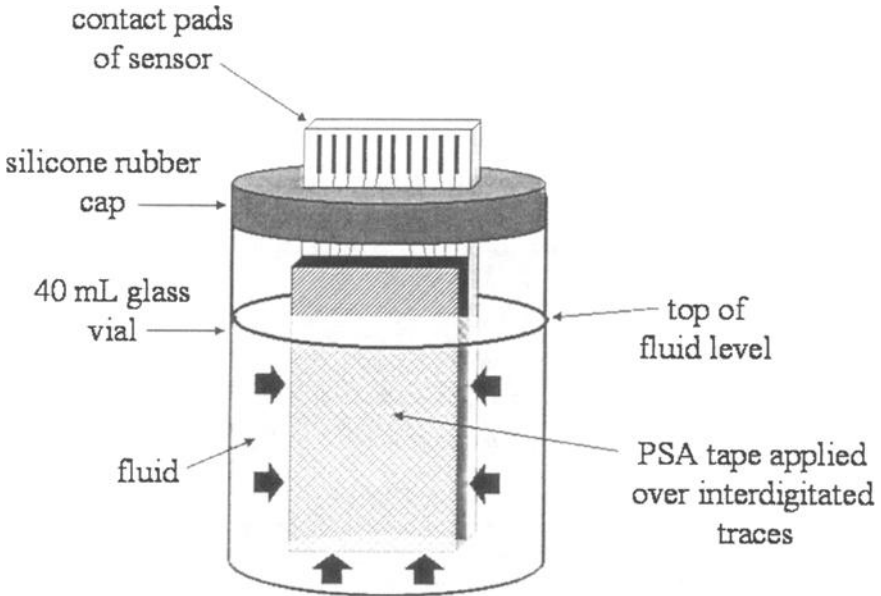


FIG. 2—Schematic of the experimental set-up of the sensor and environmental chamber. The path of diffusion is shown with the arrows.

Results and Discussion

Shown in Fig. 2 is the environmental chamber with the PSA tape adhered to the sensor. The path of diffusion of the acetone into the PSA tape is illustrated with several arrows. The path of diffusion is also illustrated in a schematic of the side-view of the edge of the specimen, shown in Fig. 3. Because the backing is impermeable, the source and maximum concentration of acetone are at the sensor edge, and the confined path of diffusion is parallel to the bondline. Therefore, the acetone diffusion begins at the edge of the PSA tape and sensor. The acetone then proceeds toward the center of the bonded PSA tape and sensor, and across each gold trace. Changes in the capacitance, due to fluid absorption, are detected at the sensor surface.

The initial value of the capacitance and resistance obtained from each pair of pads is different because each trace has a slightly different length and location. In order to make comparisons

among the different pairs of pads, the capacitance was normalized according to the following expression:

$$\frac{(C - C_0)}{(C_f - C_0)} \tag{1}$$

where C is the capacitance at a value of x and exposure time, and C_0 and C_f are the initial and final capacitances, respectively. Equation 1 is based on treating the volume fractions of fluid and adhesive as two independent layers aligned parallel to the applied electric field. A perpendicular layer model and the Brasher-Kingsbury model [21] were also employed. The resulting normalized capacitance as a function of exposure time data were essentially identical for all three models.

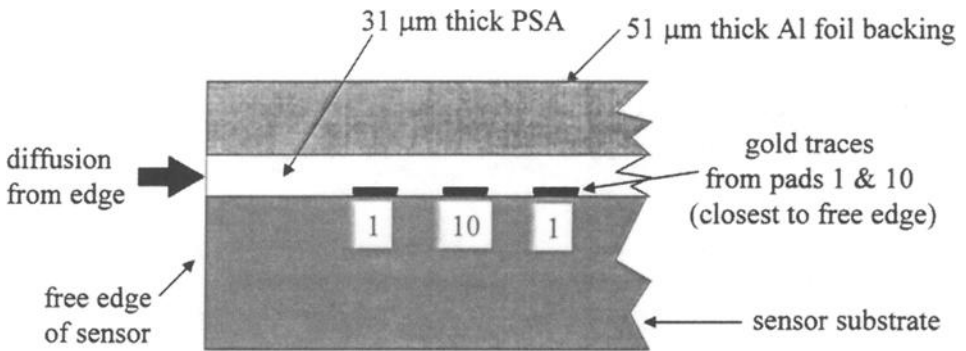


FIG. 3—Schematic of the side-view of the bonded PSA tape illustrating the path of diffusion of acetone.

Figure 4 shows the normalized capacitance as a function of exposure time, up to 2 h. The final capacitance was obtained after 60 h of exposure. Figure 4 illustrates that the rate of change in capacitance resulting from absorption of the acetone occurs faster in regions closer to the edge of the specimen. Figure 4 also shows the initial region of the normalized capacitance as a function of exposure time and illustrates a “lag” time necessary for the acetone to traverse across the sensor from the free edge to the respective pair of contact pads. If we assume the capacitance is a linear function of absorbed fluid, the normalized capacitance and normalized concentration are equivalent. From the data in Fig. 4, the concentration profile of the acetone near the interface in the bonded PSA tape was determined. The concentration profile, shown in Fig. 5, is the normalized concentration as a function of the distance from the edge of the specimen, x , for different values of exposure time. The absorption behavior of acetone into the PSA was clearly non-Fickian. This was not unexpected, given that interfacial diffusion plays a role and that the PSA absorbs acetone readily and has poor cohesive strength, resulting in significant swelling and loss of mass.

The adhesion of the tape bonded to the sensor was measured as a function of exposure time to acetone. The adhesive fracture energy (G) was measured using the 90° peel test and Eq 2 [22,23].

$$G = \frac{P}{b} \tag{2}$$

where P is the average load, and b is the tape width. In the experiment, the PSA tape was adhered to the sensor and then immersed entirely in the acetone. The specimens were then

removed, patted dry with paper, and tested in a universal testing machine. No special modification of the peel test fixture was required for the adhesion test. The cross-head displacement rate was 0.1 mm/s. Figure 6 shows the G as a function of exposure time. After 6 h, the adhesion has been reduced to approximately 5 % of the initial dry strength. Comparison between the peel test results and the concentration profile shown in Fig. 5 reveals the relationship between adhesion loss and the relative concentration of acetone at the surface. After 6 h, the relative concentration of acetone at the interface is approximately 80 %.

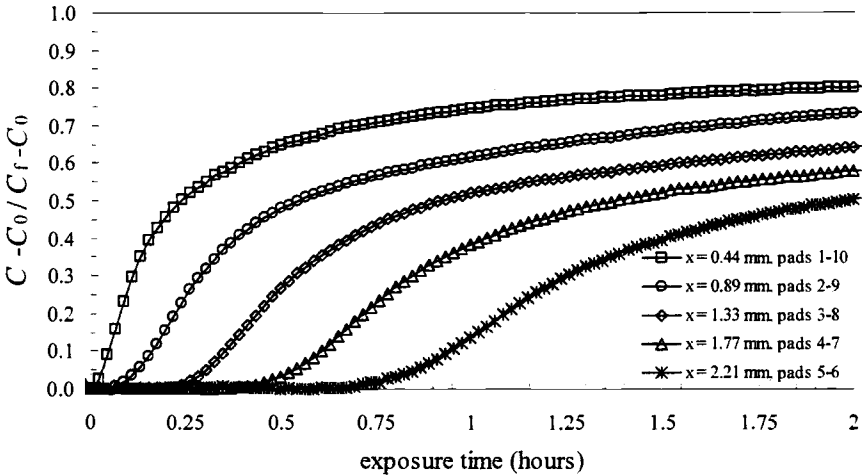


FIG. 4—Initial region (up to 2 h) of the normalized capacitance as a function of exposure time (hours) for different values of x .

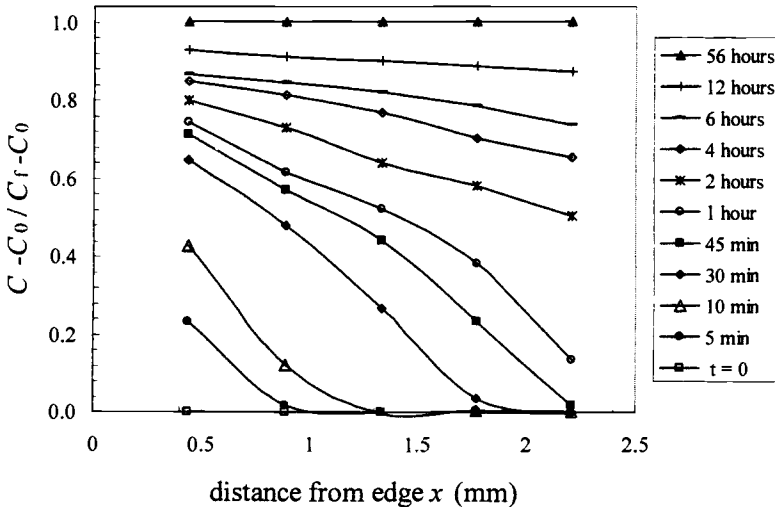


FIG. 5—The resultant concentration profile.

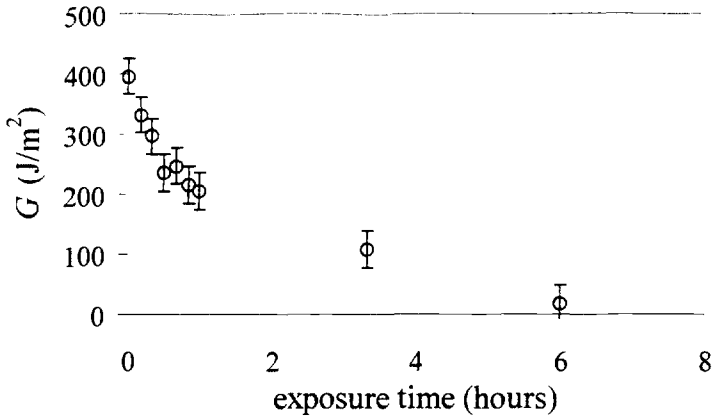


FIG. 6—The adhesive fracture energy as a function of exposure time.

Summary

The absorption of acetone at room temperature into an adhered PSA tape was measured by applying the technique of SFCM and utilizing a unique interdigitated electrode sensor design. The interfacial diffusion results and adhesion measurements were compared, and the relationship between the relative concentration and adhesion loss was determined. This study suggests these novel sensors are applicable for the study of interfacial diffusion processes, and could be extended to other coatings or adhesives in a variety of environments.

Acknowledgments

The authors acknowledge the financial support of the Hewlett-Packard Co., the Center for Adhesive and Sealant Science at Virginia Tech, and the Adhesive and Sealant Council Education Foundation. We also thank Paul Reboa, Marshall Field, Dan Pullen, Dave Markel, Jim McKinnel, and Josh Smith of the Hewlett-Packard Co. for all of their work. We acknowledge the help of Prof. David A. Dillard, Prof. John G. Dillard, Jim Coulter, Sandra Case, Jeremy Lizotte, Scott Trenor, and Doug Crowson of Virginia Tech. In addition, we extend our appreciation to Prof. Kai-tak Wan of the University of Missouri at Rolla. Emmett O'Brien thanks Tom Seery, Christopher White, and Jonathan Martin for funding during the preparation of this manuscript.

References

- [1] McCrum, N. G., Read, B. E., and Williams, G., *Anelastic and Dielectric Effects in Polymeric Solids*, John Wiley and Sons, New York, 1967.
- [2] D'Amore, A., Kenny, J. M., Nicolais, L., and Tucci, M., *Polymer Engineering Science*, Vol. 30, No. 314, 1990.
- [3] Senturia, S. D. and Sheppard, N. F., *Advances in Polymer Science*, Vol. 80, No. 1, 1986.
- [4] Day, D. R., Shepard, D. D., and Craven, K. J., *Polymer Engineering and Science*. Vol. 32, 1992, pp. 524–528.

- [5] Nairn, B. J., Dickstein, P. A., Plausnis, D. J., and Spelt, J. K., *J. Adhesion*, Vol. 48, 1995, pp. 121–136.
- [6] Rammelt, U. and Reinhard, G., *Prog. Org. Coat.*, Vol. 21, No. 205, 1992.
- [7] Davis, G. D., Krebs, L. A., Drzal, L. T., Rich, M. J., and Askeland, P., *J. Adhesion*, Vol. 72, 2000, pp. 335–358.
- [8] Affrossman, S., Banks, W. M., Hayward, D., and Pethrick, R. A., *Proc. Instn. Mech. Engrs.*, Vol. 214, 2000, pp. 87–102.
- [9] vanderWel, G. K. and Adan, O. C. G., *Prog. Org. Coat.*, Vol. 37, 1999, pp. 1–14.
- [10] Zanni-Deffarges, M. P. and Shanahan, M. E. R., *International Journal of Adhesion and Adhesives*, Vol. 15, 1995, pp. 137–142.
- [11] Vine, K., Cawley, P., and Kinloch, A. J., *Journal of Adhesion*, Vol. 77, 2001, pp. 125–161.
- [12] Nguyen, T., Byrd, E., Bentz, D., and Lin, C., *Progress in Organic Coatings*, Vol. 27, No. 181, 1996.
- [13] Linnossier, I., Gaillard, F., Romand, M., and Nguyen, T., *Journal of Adhesion*, Vol. 70, 1999, pp. 221–239.
- [14] Wu, W. L., Orts, W. J., Majkrzak, J., and Hunston, D. L., *Polymer Science and Engineering*, Vol. 35, 1995, pp. 1000–1004.
- [15] Kent, M. S., Smith, G. S., Baker, S. M., Nyitray, A., Browning, J., Moore, G., et al., *Journal of Materials Science*, Vol. 31, 1996, pp. 927–937.
- [16] Kent, M. S., McNamara, W. F., Baca, P. M., Wright, W., Domier, L. A., Wong, A. P. Y., et al., *Journal of Adhesion*, Vol. 69, 1999, pp. 139–163.
- [17] Kent, M. S., McNamara, W. F., Fein, D. B., Domier, L. A., and Wong, A. P. Y., *Journal of Adhesion*, Vol. 69, 1999, pp. 121–138.
- [18] Vogt, B. D., Soles, C. L., Jones, R. L., Wang, C. Y., Lin, E. K., Wu, W. L., et al., *Langmuir*, Vol. 20, 2004, pp. 5285–5290.
- [19] Takahashi, K. M., *J. Appl. Phys.*, Vol. 67, 1990, p. 3419.
- [20] Takahashi, K. M. and Sullivan, T. M., *J. Appl. Phys.*, Vol. 66, 1989, p. 3192.
- [21] Brasher, D. M. and Kingsbury, A. H., *Journal of Applied Chemistry*, Vol. 4, No. 62, 1954.
- [22] Gent, A. N. and Hamed, G. R., *Journal of Applied Polymer Science*, Vol. 21, 1977, pp. 2817–2831.
- [23] DeVries, K. L. and Adams, D. O., “Mechanical Testing of Adhesive Joints,” *The Mechanics of Adhesion*, Dillard, D. A. and Pocius, A. V., Eds., Elsevier, 193, 2002.

Norm V. Gitis,¹ Jun Xiao,² and Michael Vinogradov³

Advanced Methods of Coating Adhesion Testing

ABSTRACT: Adhesion of coatings from 1 nm to 0.1 mm was successfully evaluated with multi-sensing technology, based on simultaneous high-resolution force, electrical, and acoustic measurements. Sharp changes in the signals were indicative of the thresholds of adhesion and delamination for various thin and thick coatings during scratching and indenting with several test tools, both sharp (diamond tips) and dull (balls).

KEYWORDS: adhesion, coatings, thin films, testing

Introduction

There are numerous techniques known for adhesion and delamination testing, some of the most common being a tape test, stud-pull test, scratch test, and an indentation test [1]. In the tape test, a tape is pulled off the surface containing a scratch, which provides the failure initiation. In the stud pull test, a stud held with thermosetting epoxy is pulled off the film surface. The indentation test, wherein a ball is pressed into the surface, is used for hard coatings, and the failure pattern indicates acceptable behavior. In the scratch test, where an indenter moves in both vertical (loading) and horizontal (sliding) directions, an acoustic emission sensor allows for detection of the initiation of fracture, while the scratch pattern indicates the type of failure.

The Universal Nano+Micro Materials Tester (UNMT) has been developed to perform a variety of the common adhesion tests [2]. During any of them, it can simultaneously measure contact or surface electrical resistance; displacement, deformation, or depth of penetration; contact acoustic emission; temperature; forces in all three directions; and digital video of the contact area. This report covers evaluation of the adhesion and delamination properties of coatings by the scratch test.

Instrumentation

The fully computerized tester UNMT provides a combination of precision linear and rotational, including reciprocating, motions to the specimens, with programmable speeds ranging from 0.1 $\mu\text{m/s}$ to 10 m/s. A load is applied via a closed-loop servo-mechanism and is programmed to be kept constant or linearly increasing, ranging from 10 nN to 1 kN. The environmental temperature and pressure can also be controlled. Friction force, normal load, electrical contact resistance (ECR), and contact acoustic emission (AE) are all measured at a total sampling rate of 20 kHz, displayed in real time and recorded for further analysis.

Manuscript received 4 October 2004; accepted for publication 8 April 2005; published October 2005. Presented at ASTM Symposium on Advances in Adhesives, Adhesion Science, and Testing on 4-6 October 2004 in Washington, DC.

¹ President, Center for Tribology, Inc., 1715 Dell Avenue, Campbell, CA 95008.

² Applications Manager, Center for Tribology, Inc., 1715 Dell Avenue, Campbell, CA 95008.

³ Engineering Manager, Center for Tribology, Inc., 1715 Dell Avenue, Campbell, CA 95008.

Specimens in a wide variety of shapes and dimensions (up to 200 mm) can be accommodated. For scratch-adhesion tests, various tool geometries and materials can be used, metal or ceramic ball or needle, diamond stylus or patented micro-blade.

Experimental

Two types of coatings were tested in this work: 50-micron “thick” soft elastomer coatings used on ink-jet cartridges and few-nanometer “thin” hard diamond-like coatings used on hard magnetic disks. These two types have been chosen as being very different in both hardness and thickness; thus covering a wide spectrum of practical applications.

The effects of scratching tools were studied on three types of tools, 1.6-mm balls from stainless steel and tungsten carbide, 10-micron sharp diamond stylus, and a novel tungsten carbide micro-blade, which is as sharp as the stylus (10 micron) but very wide (0.8 mm) [3].

To achieve effective results, the multi-sensor technology was utilized.

Results on Thick Soft Coatings

Neither steel nor tungsten carbide balls produced useful delamination data. The sharp diamond stylus scratched the coating, but did not delaminate it. The micro-blade produced repeatable scratch-resistance and delamination/adhesion results.

The micro-blade test consisted of linearly increasing the applied load from 10–1000 mN, while slowly sliding the micro-blade at 1 mm/s, with continuous multi-sensor process monitoring.

The optical photo of the tested surface is shown in Fig. 1 above; the corresponding friction force plot is presented in Fig. 2 below. One can clearly see three zones, namely: deformation with no debris formation at very low loads (right part of Fig. 1, left part of Fig. 2), micro-scratching with production of a lot of micro-debris (middle parts of Figs. 1 and 2), followed by delamination with chunks of debris formed at higher loads (left part of Fig. 1, right part of Fig. 2). The critical loads (or times) of scratching (on the borderline of the deformation and micro-scratching zones) and delamination (on the borderline of the scratching and delamination zones) can be found easily from these tests, and they tend to be repeatable.

Though both the optical and force plots show all three zones, the borderlines between them, defining the critical loads (times) or micro-scratching and delamination, can be determined with higher accuracy by utilizing additional electrical and acoustic measurements.

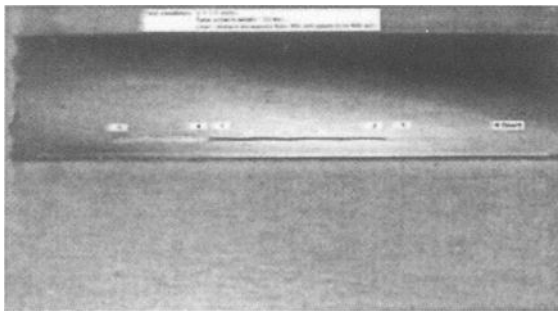


FIG. 1—Coated surface tested with micro-blade.

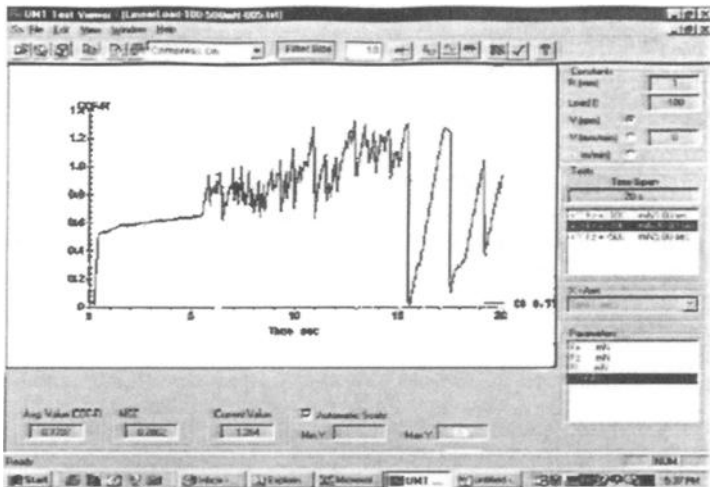


FIG. 2—Friction force in test with micro-blade.

If a coating is non-conductive and a substrate is conductive, then electrical contact resistance is measured. If a coating is conductive, the electrical surface resistance is monitored. In either case, the electrical measurements typically show both critical thresholds of the onset of scratching (when electrical resistance begins to change) and breaking through the coating (when electrical resistance reaches the level of the substrate resistance). An example of a sharp threshold is given in Fig. 3.

The high-frequency contact acoustic emission reflects the scratching and delamination processes of solid coatings when their structure is relatively ordered and they are relatively hard. For instance, most metal and ceramic coatings emit substantial acoustic waves during such tests, while most soft polymers do not emit measurable acoustics. The acoustic emission resolution in terms of surface defects is defined by its frequency. For example, to detect a 10-nm scratch or delamination defect in the coating at a test speed of 1 cm/s (taking into account that 1 cm = 10 000 nm, and a signal has to be several times higher than the process), one needs the signal frequency of at least 5 kHz. In fact, we use the range of up to 5 MHz, which allows for detection of the very beginning of the tiniest micro-scratches and micro-delamination.

The effective use of the contact acoustic emission signal is illustrated in Fig. 3. In this example, the critical threshold of breaking through the coating can be determined by the sharp drop in electrical resistance, and this is fully supported by the sharp increases in friction and acoustic signals. It is interesting that both friction and acoustic show a substantial pre-failure rise at the same lower load, corresponding to the beginning of coating damage. Moreover, the ultra-sensitive acoustic emission started even earlier, which reflected the onset of tiny coating damage, undetectable yet by the electrical and force signals.

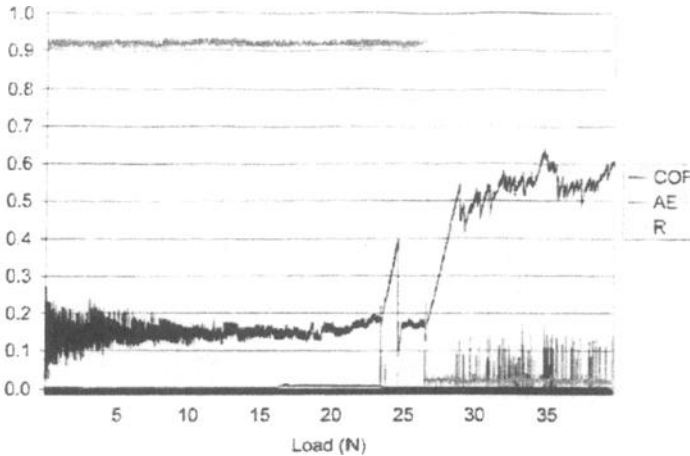


FIG. 3—Multi-sensor determination of coating failure.

Results on Thin DLC Coatings

DLC, or diamond-like carbon coatings, are used in various industries. Their deposition technologies, and therefore properties, vary from application to application [4]. For example, we have observed in numerous tests that the durability of very thin DLC coatings on hard magnetic disks and heads is the highest, while the durability of the DLC coatings on window glass and razor blades is much lower [4]. Correspondingly, the scratch adhesion test procedure should be different.

Soft copper or gold-plated 4-mm or 6-mm balls have produced the most repeatable test data on the softest DLC coatings. Hard 1.6-mm tungsten carbide balls produced quite repeatable results on mid-range DLC coatings. Sharp diamond styluses scratched the coating but did not delaminate it. Also, the sharp stylus data had limited repeatability due to the surface morphology differences from one scratch to another. The tungsten carbide micro-blade, averaging the scratch data over their substantial width, produced the most repeatable results for the hardest and thinnest coatings. Again, in all of these tests, the critical thresholds were determined by simultaneous measurements of forces, electrical and acoustic signals (see Fig. 3), though the latter ones were not informative for very thin coating films. The electrical resistance of DLC coatings was always measurable, though the harder and more diamond-like a coating, the less conductive it was.

The thinnest coating tested was a 1.5-nm DLC film on a magnetic head wafer, the durability of which was found to depend on the rate of deposition. Figure 4 includes some of the results for thin, hard DLC coatings on magnetic disks. For each DLC thickness, four disks were tested, and the high data repeatability between them is obvious from this figure. Reduction in film thickness by a factor of 4, from 10 nm to 2.5 nm, decreased the critical load by a factor of 5, from 125 to 25 cN. Lubricating the disk with a thin 2-nm layer of a topical Fomblin lubricant, common for the magnetic disks, increased the critical load by a factor of 4.5 for the thin 2.5-nm coating. The micro-blade test consisted of linearly increasing the applied load from 1 cN to 100 cN, while slowly sliding the micro-blade at 1 mm/s, with continuous multi-sensor process monitoring.

Conclusion

1. The multi-sensing technology, based on simultaneous high-resolution force and electrical and acoustic measurements, allows for very accurate determination of both delamination/adhesion and scratch resistance of both thin and thick coatings. Using the test tools with higher contact area (or length), like micro-blade or ball, may allow for more repeatable results than those obtained with sharp styluses.
2. The nano+micro tester UNMT provides a useful platform for all common types of adhesion and delamination tests, with the complete utilization of all the advantages of the multi-sensing technology.

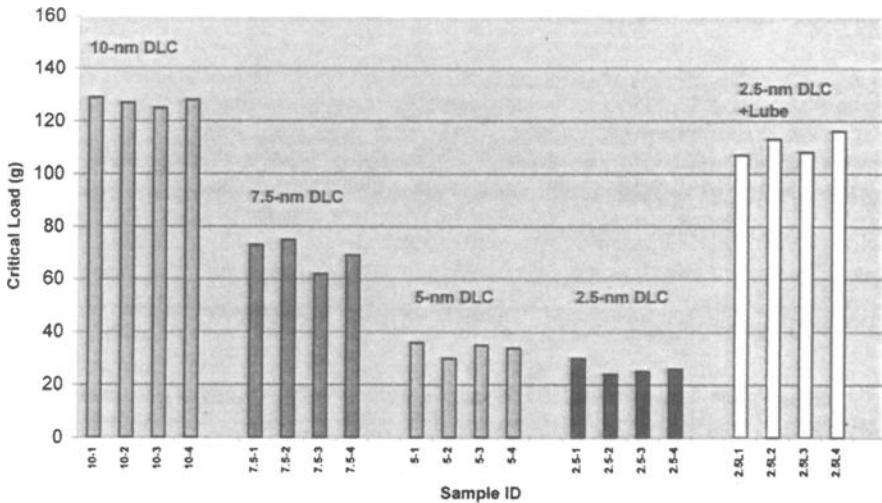


FIG. 4—Micro-scratch test data for thin hard coatings.

References

- [1] Mattox, D. M., "Surface & Film Characterization," *Vacuum Technology & Coating*, January 2001, pp. 14.
- [2] Gitis, N. and Vinogradov, M., patent of "Micro-scratch Test Indentation and Method of Micro-scratch Testing," 1999.
- [3] Xiao, J., "Scratch Test Report," *CETR 2003*, July 23.
- [4] Xiao, J. and Gitis, N., "Novel Testing Method and Apparatus for Characterizing Terminological Properties of Lubricant and Durability Evaluation of thin Film Coating," *The 7th China National Tribology Conference*, pp. 306–307.

Gerald E. Wheeler,¹ Ben S. Madsen,¹ K. L. DeVries¹

Fracture Mechanics Applied to Adhesive Joints

ABSTRACT: Since the advent of synthetic adhesives in the middle of the last century, the growth in their usage has been so phenomenal that a handbook, the International Plastics Selector-Adhesives, published by D.A.T.A. in 1991, lists some 5000 different adhesive formulations that are commercially available. Despite their wide usage, much is not well understood about adhesives and adhesive joint failure. A few observations relevant to this discussion of Fracture Mechanics Analysis of Adhesive Joints are: (a) The stress distribution in such joints is never as simple as often assumed, and the usually reported "standard test results" often completely ignore the most important aspects of the stress distribution. (b) Crack growth does not always initiate at the point of maximum stresses in an adhesive joint. (c) The locus of adhesive crack growth is often somewhat removed from the adhesive-substrate bond-line, but there are instances where it closely follows this bond-line. (d) Adhesive Fracture Mechanics analysis can provide significant information on the resolution of questions raised in these observations. This presentation will review some of the work in these areas by graduate students in our laboratory. Some of the cited work was accomplished by previous lab students. Other parts of the cited work are from ongoing research by current students. The presentation will endeavor to demonstrate that: (a) Adhesive Fracture Mechanics can be used to quantitatively predict the strength of adhesive joints and, more particularly, to elucidate the effects of such factors as adherend thickness, adhesive thickness (and variation), amount of overlap, geometric configuration, material discontinuities, etc. (b) Other factors being equal, crack growth tends to initiate at locations of maximum energy release rate irrespective of whether or not these are points of maximum stresses. (c) The preferred locus of crack growth is along those paths for which the energy release rate is a maximum. In each of these cases, results of a fracture mechanics analysis will be presented along with experimental verification of the analyses.

KEYWORDS: adhesive joints, adherends, shear stress, normal stress

Introduction

This paper explores the role of various geometric factors on the mechanical behavior of adhesive joints. In doing this, some new analyses will be presented, and some prior work will be reviewed. Perhaps the most important property of an adhesive is the durability of the joints it produces. Durability is a property that is not always easy to define and certainly depends on many factors other than what adhesive is used. The nature and type of adhesive is one important factor, and the designer of a joint has many adhesives from which to choose. The 1991 edition (6th ed.) of the International Plastics Selector *Adhesives* [1] lists some 5000 different adhesives that are commercially available. While the properties of many of these are similar and may overlap, there is also considerable versatility and difference among them. Some of these differences relate to the adhesive's strength and durability. As a case in point, this same handbook lists values of adhesive joint strength for many of these adhesives as the "Lap Shear Range" (an item to be discussed subsequently) with values ranging from under 100 psi to more

Manuscript received 22 September 2004; accepted for publication 3 November 2004; published May 2005.

Presented at ASTM Symposium on Advances in Adhesives, Adhesion Science, and Testing on 4-6 October 2004 in Washington, DC.

¹ University of Utah, 50 S Central Campus Dr., Salt Lake City, UT 84112.

than 5000 psi. Durability of a joint is not solely dependent on the adhesive used. It is a complex function of many different factors. First, it is more than just short-term strength as might be measured in a testing machine. Chemical and physical aging, environmental factors (e.g., the presence of moisture), and curing conditions can affect durability. Surface preparation and surface treatment of the adherends play critical roles in durability. The nature and mode of loading are also important; an adhesive may have very different strength values when loaded in tension than when loaded in shear. The role of time is also important, as a joint that supports rather large loads may fail at much lower loads under sustained loading (creep) or with cyclic loading (fatigue). What may appear as subtle differences in geometry can dramatically affect durability. These differences include, for example, thickness of the adherends, amount of overlap of the adherends (for lap joints), the thickness of the adhesive bond-line, and many other factors. The purpose of this paper is to explore and partially quantify the effect of some of these geometric factors on short-term strength.

It is fortunate that ASTM and other organizations have developed and formalized a number of different test methods to investigate behavior of adhesives and adhesive joints. Engineers have recognized that there are many factors that affect the quality of a joint and have designed tests to measure many of these effects. Most of the standards related to adhesives can be found in the Annual Book of Standards, Section 15 [2]. The following example illustrates the utility of some of the standards that have been developed: In recognition that different adhesives might bond to different substrates, the Spot Adhesion Test Method described in ASTM D 3803 was developed. In this test, a small spot of a chosen adhesive is applied to the appropriately prepared substrate and allowed to cure. The difficulty in prying the adhesive spot loose from the substrate with a spatula or other object is used as a quick screening method to help determine if full scale quantitative testing of that particular adhesive/adherend system is justified. Likewise, there are tests designed to determine adhesive joint resistance to: (1) moisture by ASTM D 3498, (2) heat by ASTM D 4502, (3) chemical attack by ASTM D 896, (4) oxidative deterioration by ASTM D 3498, (5) creep under sustained loading by ASTM D 1780, and (6) fatigue failure under cyclic loading by ASTM D 3166. There are also other standards that measure resistance to weathering, attack by fungi, bacteria, yeast, etc.

Of more immediate interest to this paper are the tests that measure strength of a joint. Again, a variety of standards have been developed to explore different aspects related to strength. Superficially, at least, it appears that most adhesive joints are loaded in one of three modes; tension, shear, or peel. Accordingly, there are many standards describing test methods designed to expose joints to these loading modes. It is now well known, and as will be substantiated further in this paper, that the stress state in adhesive joints is complex and rarely, if ever, falls solely into any one of these modes. ASTM standards also classify some tests as cleavage tests (e.g., D 1062, D 5041, D 4896, and D 3433), which might be viewed as a combined tensile and peel mode. The analysis found in D 3433 has its basis in fracture mechanics and provides insight into behavior not available through stress analysis alone. This paper will attempt to demonstrate that fracture mechanics analysis of different adhesive joint failure tests can also be enlightening. To accomplish this task, results from some prior work in this laboratory and elsewhere will be reviewed along with some new results.

Analysis

The geometry of most adhesive joints appears deceptively simple, which has led to some misleading design methodologies. The stress state and stress distribution in most adhesive joints

is actually quite complex [2]. To address this complexity, ASTM D 4896, "Use of Adhesive-Bonded Single Lap-Joint Specimen Test Results," was developed. Figure 1 from this standard is reproduced in this paper as Fig. 1. When using a lap joint, it is noted that not only do the stresses along the length of the overlap vary dramatically, but significant tensile stresses are induced in the joint. Note: in Fig. 1, near the bond termini, the magnitude of these tensile stresses actually exceeds the magnitude of the shear stresses. Bond termini, as used here, represents the ends of the region of overlap. For adhesive joints, it also represents the start and end of the adhesive bond-line. Accordingly, in Fig. 1, the bond termini are at $Z/l = 0$ and 1. Could the failure of this often called "lap shear specimen" actually be dominated by the induced tensile stresses?

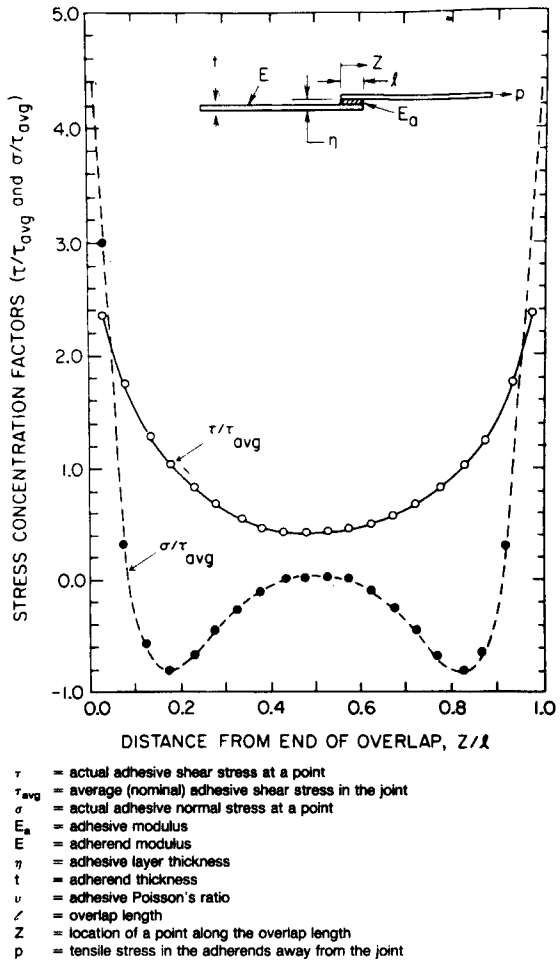


FIG. 1—(copy of Fig. 1 from ASTM D 4896): Variation of the shear and normal stresses (formalized) (τ/τ_{avg} and σ/τ_{avg} , respectively) of a single-lap specimen (adapted from [2]).

The results shown in Fig. 1 were obtained with the aid of computers using finite element techniques. In fact, the stresses for most practical adhesive joint geometries are difficult (or even impossible) to solve in closed form by analytical techniques. The advent of the finite element method (FEM) has allowed complex geometries to be analyzed. While the authors feel that a strong argument can be made that such computer techniques are the best means available to quantitatively analyze joints, it is unrealistic to expect every designer, user, and tester of adhesives to become experts in finite element analysis. Furthermore, many designer and design firms may not have sophisticated finite element analysis programs available. Computer-based "turn-key" design packages are becoming more popular and widely available. Some of these computer aided design (CAD) packages provide the user a seamless transition to less complex FEM packages. Examples of such software include Pro/ENGINEER and SolidWorks with their FEA components: Pro/MECHANICA and COSMOSWorks, respectively. A major goal of this study was to investigate the use of finite element analysis (FEA) software, such as Pro/MECHANICA, which is increasingly being included as part of various "turn-key" design packages. In this study, FEA programs were used to aid in the fracture mechanics analysis (FMA) as will be describe subsequently. To determine the effectiveness of this type of software, the software was used in Finite Element/Fracture Mechanics Analyses in which variations in geometric dimensions of lap joints were investigated. These geometric differences included variations in the adherend thickness, adhesive thickness, and overlap length. In some cases, independent research results will be presented to compare with the FEA predictions.

One of the authors of this paper (Ben Madsen) was a part-time student-employee of Parametric Technology Corporation (PTC). PTC produces and markets pro/ENGINEER, a 3D solid modeling computer design package. As noted above, integrated with Pro/ENGINEER is the FEA package, Pro/MECHANICA. The appeal of Pro/MECHANICA is its "black box" approach. To perform a structure analysis in Pro/MECHANICA, only five straightforward steps are required. CAD programs are prevalent in industry and are likely to be used by many designers in the workforce. This has placed a large number of inexperienced FEA users in reach of Pro/MECHANICA and other similar CAD/FEA software. It is possible that these users may be more willing to use the simpler "black-box" approach as opposed to a more advanced and, possibly, intimidating specialized FEA software program. Pro/MECHANICA is integrated to run simultaneously with the 3D solid modeling computer package Pro/ENGINEER. After a design is modeled, the user may select the Pro/MECHANICA option to access a finite element analysis menu without having to leave the graphical environment. The overall use of this product is aesthetically pleasing and relatively simple. One example of this is that the user is never required to see or define the mesh. The software contains what is called an "autogem" feature that automatically selects the "best" mesh according to the program's examination of the geometry. To perform a structure analysis in Pro/MECHANICA, the five required steps are:

1. Select a coordinate system and model a shape.
2. Define materials.
3. Define constraints.
4. Define loads.
5. Run the analysis.

It is the ease of use that makes this software appealing. However, this more simplistic approach is not without problems. Obviously, as with all "black box" applications, the user is left

somewhat in the dark as to exact details in the calculations. As a consequence, the user may not be aware of sources of error in the analysis, providing a false sense of confidence in the results. Although the mesh necessary to calculate the displacement is applied automatically by Pro/MECHANICA, the user does have an aid to increase the accuracy of the software. Pro/MECHANICA offers a multipass-adaptive analysis that may be run to apply p-refinement to the mesh in order to obtain convergence. Convergence occurs when the program's results compare closely to criteria set up by the model. The criteria can include displacement, stresses, rotations, etc. Two common types of refinements are the p-refinement and the h-refinement. Generally, these are included with FEA software [3]. P-refinement modifies the polynomials that define the mathematical finite element shape functions by implementing higher order polynomials to define the elements. The order of the polynomials is continually increased, by adding nodes to elements or degrees of freedom to the nodes, until convergence occurs. The h-refinement method typically decreases the element length by adding more nodes. Pro/MECHANICA utilizes a p-refinement analysis as opposed to an h-refinement analysis. The authors are indebted to PTC for allowing Mr. Madsen free access to their software and facilities for this study.

There are several other noteworthy features of lap joints that may be obvious from Fig. 1. Both the values of the tensile and shear stresses increase very rapidly as the bond termini is approached. These values are actually singular for elastic analysis. Inspection of these stresses clearly indicates that an average shear stress criteria would likely not be terribly useful for predicting load carrying capacity of such joints. Yet, this is what is all too often done. ASTM standards [2] for testing "Lap Joints" (e.g., D 1002, D 3163, D 3165, D 3933, etc.) typically specify as stated in ASTM D 3933, Section 13.3, "*Shear Strength*-Calculate the shear strength or nominal shear stress at failure of adhesive bonds in shear from the test 5 load-slip curve as follows: $(\tau_{\max})_{\text{ave}} = (P_{\max}/A)$." Where test load-slip curves are plots of force versus displacement from a universal testing machine, P_{\max} is the maximum value of P read from this plot, and A is the size of the bonded area. The "Lap Shear Range" referred to in the first paragraph of the introduction is this lap shear strength and was determined in tests on lap joints. Reporting the results in this way has led many to assume that this quantity can be used as a design parameter. In fact, several engineering texts propose the use of the lap shear strength (obtained from handbooks or independent tests) as a "popular design rule" that, in essence, suggests using lap shear strength and design load to determine the required overlap area. Quoting from a popular (and good) material science text, "*Engineering Materials-Properties and Selection*" by K. G. Budinski [4]:

In selecting an adhesive system, one must calculate the strength required. If, for example, you wish to design an adhesive-bonded lifting device for a 50 lb (23 kg) machine component, you can use an adhesive with a 100 psi (0.689 MPa) shear strength and make the bond area 0.5 in² (3.2 cm²). You must use this type of joint-strength analysis in all adhesive-joint designs [Ref. 4, pp. 171–172].

Following the above quoted "design rule," a lap joint's shear strength is typically defined as the force at failure divided by the area of the overlap:

$$\tau_s = \frac{P_f}{A}$$

In this equation, τ_s is defined as the "shear strength," P_f is the load at failure, and A is the area of the overlap. An equation of this type suggests no dependence of strength on the adherend thickness or adhesive thickness. Texts and handbooks are relatively mute on the important role that these parameters have on lap joint strength. The description found in most texts and articles concerning joint design would suggest that doubling the bond area by increasing the overlap lengths should have a concomitant effect on strength.

This has led many researchers to postulate a simple shear stress criterion for failure. This idea persists to this day despite some early analysis, such as that of Goland and Reissner who used classical "mechanics of material concepts" to demonstrate that the joint includes shear, bending, and cleavage stresses [5]. This is more recently substantiated by several numerical analyses, some of which are cited in [1].

As previously mentioned, the single lap joint is the most common test used to evaluate adhesives because of its practical resemblance to many "real-world" joint designs. The adhesive lap joint has proven useful over the years and will likely continue to be widely used in the future. This paper discusses some of the complexities of the lap joint. The discussion will now concentrate on using finite element analysis to aid in a fracture mechanics approach to aid in understanding the mechanics of a lap joint. It will, to some extent, explore the validity of the design rules discussed above and look at the affect of some of the joint features that are not considered in these rules.

Referring again to Fig. 1, the parameters mentioned earlier [length of overlap (l), the thickness(es) of the adherends (t), and the adhesive bond-line thickness (η)] are listed in the figure, but no indication is given as to their potential affect on the load at failure. Due to the complex nature of the stress state, there is no a priori reason that each of these would not affect the strength of a joint and, hence, the load carrying capability of the joint. One might explore their effects empirically by conducting tests of lap specimens in which these quantities are systematically varied. However, if they could be explored analytically and the results compared with observations, one might gain additional insights into causal effects. This also should provide a useful tool for not only designing joints but, perhaps, pointing the way to optimize behavior.

It was noted above that average stress criteria may not always be a very useful failure criteria. Maximum stress criteria (whether it be max-normal, max-shear, or max-Von Mises equivalent stress) likewise suffer in application. At first blush, the maximum stress criteria would have a strong appeal, since with modern computational methods, such as finite element analysis, the stresses can be calculated for almost any geometry. Once these are determined, it might be argued, their maximum value could be compared with the critical value for the particular adhesive system, determined from independent tests, to predict performance. The problem is in the nature of the stresses for the lap joint. As the bond termini is approached, the stresses become singular for elastic systems. They are, therefore, infinite for any finite applied load making comparison with a critical value difficult at best. While some rather artificial methods have been devised to circumvent this problem, the authors prefer the approach of using fracture mechanics.

Fracture Mechanics had its birth in the 1920s with the work of Griffith [6]. His methods lay rather dormant for several decades. Several failures about the time of the second World War stimulated interest in the problem of fracture resulting in a resurrection of the method. For the last 60 years or so, it has been an area of very vigorous and fruitful research, technological growth, and usage. While it was initially used for brittle-homogeneous materials, its use has expanded to include materials that experience some ductility, adhesive systems, composites, and

other materials. Modern computational methods have greatly broadened its potential uses. While the actual application of the Fracture Mechanics method is often very complex, requiring highly sophisticated mathematical/computational methods, it is, in principle, really rather straightforward and easy to understand. The following brief description might help those who are unfamiliar with the method to understand the approach used in this paper.

Griffith's fracture approach might be viewed as a couple of necessary/sufficient criteria. It also assumes the presence of cracks or crack-like discontinuities in the material. In order to make one of the cracks grow, it is necessary that, at least locally, the stresses be sufficient to break the bonds in the material. For sharp cracks in a homogeneous material or at the end of a bond as discussed previously, the elastically determined stresses are singular, so these criteria are easily met. Griffith's hypothesis might be viewed as a statement of the first law of thermodynamics in that he postulated that the crack can grow only if the energy released from the stress/strain field is sufficient to account for the energy required to "create" the new fracture surface resulting from the crack growth. The value of this energy per unit surface is given various names in the literature: the specific fracture energy, the fracture toughness, the critical surface energy, or the critical energy release rate. While the actual calculations are usually not done this way, the following approach is rather descriptive of the basic approach. Assume a crack of a specific size is located at a given location in a body, which is to be exposed to an external loading. Apply a unit load to the body, and calculate the stresses and strains along with their associated strain energy in the body (U_1). Now, assume the crack has grown a small (infinitesimal) amount, increasing the crack area by an amount ΔA . Again, apply the unit load, and calculate the stresses and strains along with their associated strain energy (U_2) in the body for this new crack size. The difference between these two quantities [$\Delta U = (U_1 - U_2)$] divided by the increase in area (ΔA) is the energy release rate, i.e., $ERR_{(unit\ load)} = \Delta U / \Delta A$. The ERR is often referred to as the fracture toughness, G . For a linear elastic system, the ERR is directly proportional to the applied load. The ERR for any other load, P , would be the applied load P times the $ERR_{(unit\ load)}$, i.e., $ERR_{(P)} = P * ERR_{(unit\ load)}$. To find the value of the load (P_c) at which the crack should grow, one compares this $ERR_{(P)}$ with the critical value ERR_{crit} , usually determined from independent tests. For failure in cohesive systems, tabular values of ERR_{crit} (commonly referred to as the critical fracture toughness, G_c) are available for a number of materials reducing the need for such tests. Expressed mathematically, the relationship between the predicted load at failure, the calculated ERR, and the ERR's critical value can be written as $P_c = ERR_{crit} / ERR_{(unit\ load)}$ or, substituting the fracture toughness, G_c , for ERR_{crit} , then $P_c = G_c / ERR_{(unit\ load)}$. Stated another way, if the ERR for a given crack and loading is less than the ERR_{crit} for the given material, the crack will not grow. If it is equal to ERR_{crit} , crack growth will be impending. For greater values of ERR, the crack will accelerate with the excess energy going into kinetic energy.

Hopefully, the brief description in the previous paragraph will be helpful to those not versed in fracture mechanics in understanding the basic concept of the Griffith approach to fracture mechanics. It is, however, not the approach normally practiced in this or most other laboratories. We normally use one of two other approaches that lend themselves particularly well to FEA. The first approach is the so-called crack closure method [7] in which a finite element analysis is performed on the body of interest with an assumed crack at a given location. A pair of nodes near the tip of the crack are closed, and the forces and displacements required to close the crack are determined using FEA. The work associated with this operation is calculated, the magnitude of which, for an elastic system, is equal the ERR. The second approach, which is used for the results using Pro/MECHANICA reported in this paper, can be explained by referring to Fig. 2.

Assume we load a sample, such as a lap specimen, with concentrated loads at its ends. If both the adherends and adhesives are linearly elastic, the load-displacement curve could be schematically represented as the upper curve in Fig. 2. In the study, this curve is constructed “quantitatively” using FEA. The area under the curve represents the work done by the applied force and is equal to the elastic energy stored in the sample. Now, if this crack is assumed to grow to a new size under constant load and the analysis repeated, the result is the lower curve in Fig. 2. The area between these two curves represents the difference in specimen’s strain energy for the two crack lengths. If we assume, as hypothesized by Griffith, that this energy goes into “creating” the new fracture surface, then the energy release rate (ERR) is numerically equal to this energy divided by the increased crack area. For this simple model, this area would be the increase in crack length multiplied by the specimen thickness (25.4 mm in this study). To explore the effect that differences in sample geometry should have on strength using this mode, one would but need to make the above change in the model and then perform the analysis described above to determine the $ERR_{(unit\ load)}$ for cracks at the same location for the given unit loading. The geometry with the larger $ERR_{(unit\ load)}$ should represent the weaker sample, since as the load is increased, the critical value of the $ERR_{(unit\ load)}$ for the given material would be reached first. In the same way, “assumed” cracks could be located at various locations to predict the most critical locations for crack growth. A study of the effect of the location of a “starter crack” will be the subject of a future paper.

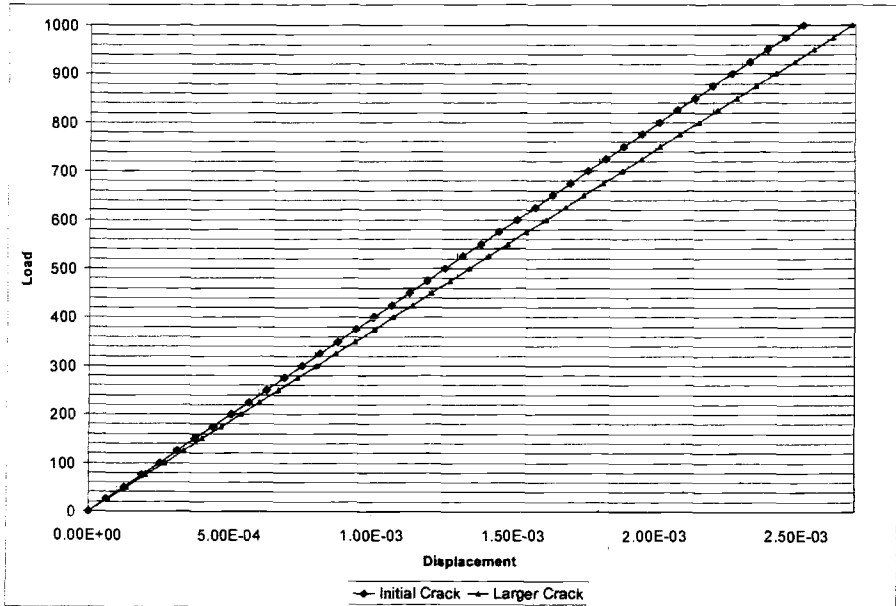


FIG. 2—Schematic of a force displacement curve for a specimen with a crack. The upper curve is for the initial crack, and the lower curve is after the growth of the crack. For elastic systems, the area between the curves represents the energy necessary to produce the new crack surface.

Effects of Geometric Differences on Lap Joint Strength

The methods outlined in the previous section were used to explore how differences in length of overlap, adherend thickness, and thickness of the adhesive bond should effect ERR and, hence, strength of the joint. Figure 3 shows schematics of the models used in this phase of the study. A crack was assumed to be located at each of the different locations shown and a FEA/ERR analysis made for that crack for differing geometries. At first glance, one might assume that cracks at the front and rear of the joint should be equivalent and have the same ERR. Such is not quite true, however, because of differences in assumed end conditions for the "fixed" and loaded ends of the specimen. The authors note that comparable differences typically occur in testing as well. Often, one grip is supported by a flexible U-Joint, while the other grip is often more rigidly attached to the machine's other cross-head. The result would be different energy release rates for cracks located at the different ends of the bond for both the FEA and experimental situations. In the finite element analyses, comparing the ERRs for the different geometries should provide a measure of how the changes in geometry affect strength for the given joint. It is assumed, in the results reported here, that a critical point for the crack growth is in the adhesive near or at the bond termini. Most of the results reported in this study are for cracks located at the position in second figure from the top (for the loaded adherend) in Fig. 3. This is an ongoing study, and a future paper will explore cracks at the various other locations, including at the interface, both at the ends, and further into the adhesive. In the analyses, the modulus of the adherends was taken as 70 GPa (10×10^6 psi) and Poisson's ratio as 0.3, both typical of aluminum. The properties for the adhesive were taken as 2.4 GPa (350×10^3 psi) and 0.35, respectively.

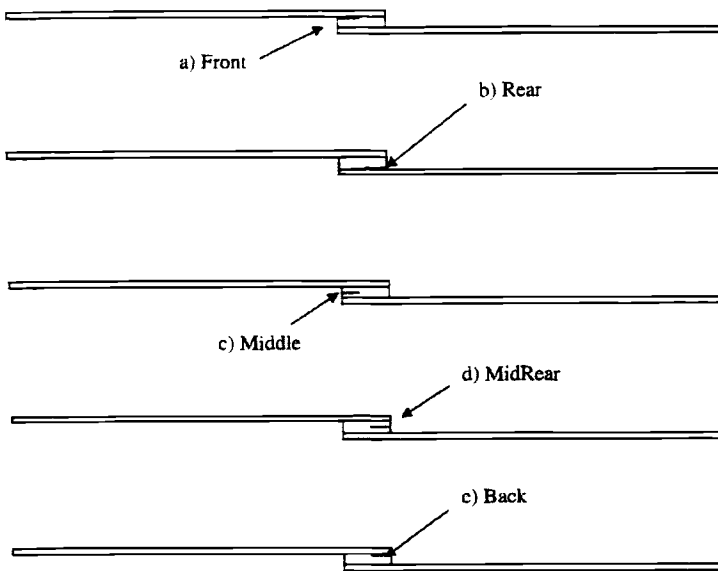


FIG. 3—Five different crack locations and corresponding identifications: a) "front" crack in interface, b) "rear" crack in interface, c) "middle" crack in the middle of the adhesive, d) "midrear" crack in the middle of the adhesive, and e) "back" crack placed at the interface.

Adherend Thickness

To explore the effect of adherend thickness on joint strength, the analysis outlined above was made for samples in which the length of overlap was held constant at 25 mm (1 in.), the width of the specimen was 25 mm (1 in.), and the adhesive thickness was taken fixed at 6.4 mm (0.25 in.). The adherend thickness was taken as either 1.6 mm (1/16 in.) or 3.2 mm (1/8 in.). A hypothesized crack was positioned at the front termini at the interface between the adherend and the adhesive. Crack lengths of 4.2, 8.4, and 12.7 mm (0.167, 0.333, and 0.5 in.) were assumed. For each crack length, the ERR decreased as the adherend thickness was increased. For example, increasing the thickness of the adherends from 1.6 to 3.2 mm resulted in an energy release rate decrease by nearly a factor of two for cracks 4.2 and 8.4 mm long, while the change was approximately 1.5 for the 12.7 mm long crack. This would suggest that the thicker adherend should exhibit the higher strength, since, as the load is increased, the critical value of the ERR would be reached at lower loads for the thinner adherend than for the thicker one. Our future plans are to conduct tests as well as further analyses to confirm these studies. In the interim, we have identified some experimental results by Anderson et al. [5] that confirm the validity of these predictions. This published study includes experimental results on tests of lap specimens with differing adherend thicknesses. These specimens were made of steel adherends bonded with an epoxy, 25 mm wide, with 12.7 mm overlap, and adherend thicknesses of 1.6, 3.2, 6.4, 9.5, and 12.7 mm. These experimental results demonstrated that the strength of the joint increased with increase in adherend thickness approaching a plateau at thicknesses greater than about 13 mm. These results are consistent with the FEA/ERR analysis outline above. The reported average strength of the joints increased 10 500 N and 16 800 N for adherend thicknesses of 1.6 and 3.2 mm, respectively. The authors feel that these data show good agreement with the ERR results. The differences between the two studies appear to be: (1) aluminum adherends for the analysis are compared to steel for the experimental results; (2) relatively large initial cracks are assumed in the analysis, and only very small (inherent) cracks were present in the experimental specimens; (3) the amount of overlap is smaller for the experimental specimens; and (4) an assumed 6.4 mm adhesive thickness for the analysis is compared to an unknown (at least unspecified) thickness for the experimental specimens.

In any case, both the FEA/ERR analysis from this study and the experimental results cited from the literature clearly demonstrate the importance of considering adherend thickness in the design of joints. Test results and commonly used design rules that ignore this aspect of adhesive joints should be used with great caution.

Thickness of the Adhesive Bond-Line

An additional factor that is often neglected in design, and to a lesser extent in joint testing, is the role thickness of the adhesive can play on joint strength. Pro/MECHANICA was used in a FEA/ERR analysis to investigate this effect. The assumed geometry for the specimens analyzed, in this part of the study, was: (1) a constant adherend thickness of 3.2 mm (1/8 in.), (2) a specimen width of 25 mm (1 in.), and (3) an overlap length of 25 mm (1 in.). For the analyses reported here, the assumed crack location was at or near the bond interface and near the front bond termini with assumed crack lengths of 4.2 mm (0.167 in.) and 8.4 mm (0.33 in.). The results for adhesive thicknesses of 1.3 mm (0.05 in.) and 6.4 mm (0.25 in.) will be compared in this paper. The ERR for the model specimen with a 6.4 mm thick adhesive was slightly more than four times the value of that of the 1.3 mm thick adhesive. This would suggest that the

strength of the specimen with the thinner adhesive should be roughly four times that of the 6.4 mm thick-adhesive specimen. We are seeking funding to conduct experiments to confirm these analyses. In the interim, however, a paper has been published [8] since Madsen completed the analysis reported here, and defended it as part of his MS Thesis. Reference [8] uses a different mechanical model to predict the effect of bondline thickness on joint strength, and also includes some experimental results of load at failure versus bondline thickness for a single-lap joint. These results are duplicated here in Fig. 4. These empirical results can be compared with the predictions of the FEA model discussed in this paper. It is noted that the adhesive used in their experiments (see their Fig. 4) exhibits considerable plastic deformation, while Madsen's analysis assumed elastic behavior. Otherwise, the geometry (see their Fig. 6 and Table 2) of their experimental specimens quite closely duplicated that of the model used in Madsen's analysis and described in this paper, except they used a 25 mm overlap length and adherend thickness of 2 mm compared to the 3.2 mm used in this paper. The elastic moduli for the adherends and the adhesive used in the experiments also compared closely to those used in Madsen's model. The experimental failure load versus bondline thickness data shown in Fig. 4 (Fig. 7 from [8]) shows the same trend as predicted by the FEA/ERR analysis presented in this paper, i.e., increasing the bondline thickness from 1.3 to 6.4 mm substantially decreases the joint strength. Extrapolation of the data from Fig. 4 for a bondline thickness of 1.3 mm to a bondline thickness of 6.4 mm indicates a decrease of strength from just over 600 N/mm width to just under 175 N/mm. This is in reasonable agreement with the factor of approximately 4 predicted in Madsen's analysis and discussed earlier in this section.

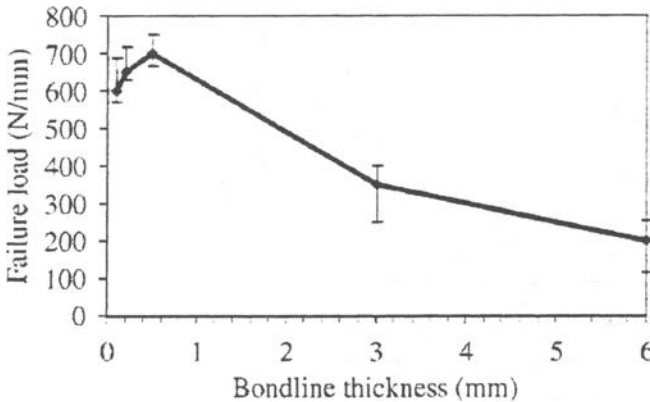


FIG. 4—Experimental failure load versus bondline thickness for single-lap joint specimens with Araldite 2011 adhesive (from [8]).

Length of Overlap

To explore the effect of overlap length on joint strength, the ERR of model specimens with overlap lengths of 25 mm (1 in.) and 50 mm (2 in.) were compared. The model sample thickness was taken as 3.2 mm (1/8 in.) and the adhesive thickness as 6.4 mm (1/4 in.), while the crack was situated at the rear of the overlaps with assumed lengths of 4.2, 8.4, and 12.7 mm, respectively. For the 25 mm long overlap, the calculated energy release rate was 0.46, 0.49, and 0.53 (in arbitrary units) for the 4.2, 8.4, and 12.7 mm long cracks, respectively. Increasing the overlap to

50 mm decreased the energy release rate for the same length cracks and the same load by approximately 3 %, 7 %, and 12.5 %, respectively. This clearly suggests that doubling the bond area of a joint with a 25 mm overlap by doubling the length of overlap will not dramatically increase the joint strength. We hasten to note that the analysis assumes an elastic adhesive. Plastic behavior will likely result in a larger increase in strength with the above amount of overlap. Prior experiments in this laboratory [9], in which the bond area was reduced, demonstrated that the reduction of joint strength was not concomitant with the amount of area reduction. For example, a series of lap specimens was constructed of steel bonded with epoxy and tested in this laboratory for Thiokol Corporation [9]. Three variations of the specimens were manufactured and tested (five each) as shown in Fig. 5: (a) lap specimens in which no debonds were intentionally introduced, (b) lap specimens in which Teflon[®] Tape (<0.08 mm thick) was used to effectively reduce the bond area by one half starting at one bond termini, and (c) lap specimens similar to those of b), except the tape was again placed to reduce the bond area by one half the unbonded area, but the tape was located in the center of the overlap. It is noted that these latter geometries might be viewed as more severe than simply reducing the length of overlap by 50 % since the tape introduced rather sharp and long cracks. Nevertheless, the joint's strength was not reduced by 50 %. Instead, the average reduction (of 5 samples each) in strength of the joints was 23 % and 3 %, respectively, from the average value of 4715 (sd = 1210) N for the fully bonded specimens. All these tests were conducted at a loading rate of 0.5 mm/min in an Instron Testing Machine. Clearly, both the FE analysis and the experimental test results demonstrate the fallacy in using a design rule based solely on a joints reported (or measured) "Lap Shear Strength" to determine the needed amount of overlap to support the design load.

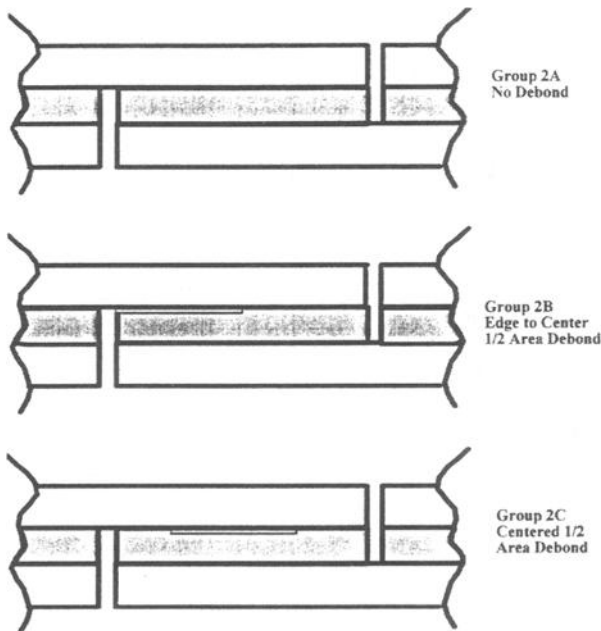


FIG. 5—Schematic of lap specimen Group 2 showing locations at which intentional large initial debonds were introduced in specimens 2B and 2C.

Locus and Path of Crack Growth

As a final part of this section of the paper, the reader's attention is directed to prior research that demonstrates some additional utility of the combined FEA/FMA approach to predict joint failure. One might reasonably ask: (1) For a given geometry, at what location will fracture most likely originate; or equivalently, at what location(s) would a crack of a given shape and size be most likely to propagate? (2) What is the most likely path a propagating crack will follow?

For at least some cases (those explored to date), it has been demonstrated that crack growth originates at points of maximum energy release rate [10]. Button tensile joint tests were analyzed by finite element methods in conjunction with fracture mechanics analysis as a function of the joint diameter to adhesive thickness ratio (D/t), where D is the diameter of the rod shaped specimen (and adhesive), and t is the adhesive thickness. It was determined that the values of the energy release rate, as well as the locations of maximum energy release rate, are both functions of this D/t ratio. In the analysis, "starter" cracks were assumed to be located at the center of the joint or around the edge of the adhesive bond, and the energy release rates for a unit load were calculated. Samples were constructed of clear PMMA rod and sheet bonded with a transparent polyurethane (Solithane 113[®] manufactured by Thiokol Chemical Corporation) with varying diameter to adhesive thickness ratios. These samples were pulled to failure on an Instron with a light path set-up such that the failure along the adhesive bond could be observed with a video camera from below the specimen. In this way, both the load at failure and the site of failure "initiation" could be recorded. Using the experimental results and assuming there is an "inherent crack size," the FE analysis was used to calculate the trend in predicted failure load as a function of adhesive thickness for both assumed sites for crack growth. The experimental results are shown in Fig. 6.

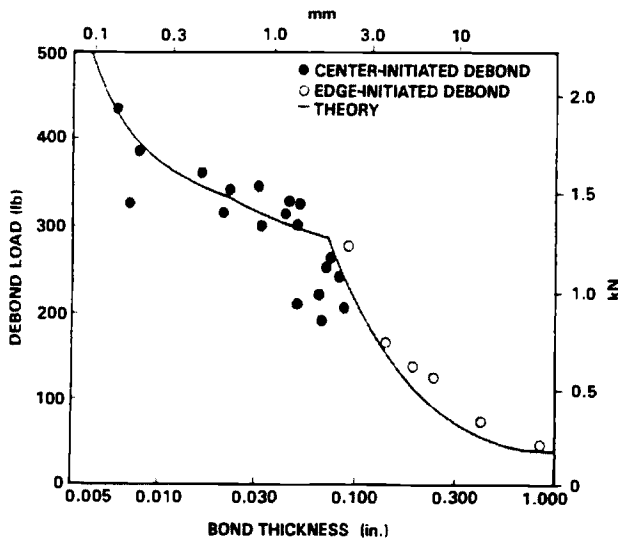


FIG. 6—Effect of adhesive thickness on load at failure and location from which cracks grow for button tensile test. Specimens made of PMMA with a diameter of 1.5 in. The model adhesive was Thiokol Chemical Corp. Solithane 113[®] polyurethane. Crack growth was observed and recorded with a video camcorder.

The specimens used in this testing were 38 mm (1.5 in.) diameter PMMA rods bonded with the transparent adhesive (also 38 mm diameter) to flat PMMA sheets. The bottom plate was attached to the testing machine's lower crosshead with four bolts that could be adjusted to obtain correct alignment. A flexible cable was bonded into the "free" end of the rod and attached to load cell on the other crosshead of the testing machine. As noted above, a mirror was arranged below a hole in the lower crosshead so that the bondline could be observed both visually and with a camcorder. The figure shows the FEA/FMA theoretical curve as well as the experimental data in the form of load at debond (failure) versus the thickness of the adhesive. The experimentally determined failure loads are shown as circles on the plot. Note that two theoretical trend curves are evident in Fig. 6, one for cracks proceeding from "inherent cracks" located at the edge, and the other from such cracks located at (or near) the center. The experimental data closely follow these theoretical trend lines, and the optically/video observed location of failure "initiation" represented by open or filled circles is surprisingly consistent with what would be expected from the analysis. That is, cracks tend to propagate from points of highest ERR. In another earlier study, a frustum of a cone was used to model the pull-off of a dental crown adhesively bonded to a tooth remnant. A similar effect was observed. The PMMA cone segment was bonded (with different model adhesives) into a complimentary transparent PMMA conical hole with a 1.5 mm starter crack produced about its periphery using mold release. During cone pull-off testing, it was observed that when the cone angle was zero (i.e., the cone was a cylinder), crack growth always proceeded from this starter crack as shown in the top photograph in Fig. 7. On the other hand, when the cone angle was increased to 5°, the crack did not proceed from this relatively large starter crack for any of the five samples tested. Rather, for these samples, the cracks first "appeared" and grew from a location nearer the center of the cone frustum as illustrated in the other photograph in Fig. 7. Subsequent FE analysis established that, for a 5° cone and a given load, the energy release rate at the tip of the "starter crack" was less than that for a very small crack [so small that it would be difficult to observe optically (e.g., 0.03 mm)] located halfway up on the bond area. On the other hand, the maximum energy release rate, for the 0° cone (a cylinder), was at the tip of the "starter crack." Again, it was noted that cracks were observed to grow from regions of high energy release rate as determined by FE/FM analyses.

Finally, it will be demonstrated that fracture mechanics provides insight into the preferred path of crack growth. A perplexing problem that, despite considerable speculation over the last 50 years, has remained unsolved is: why do cracks follow a particular path? For example, for many practical joints, it has been observed that cracks typically proceed in the adhesive rather than along the interface. This phenomenon is so common that, in his classical text on adhesives, Kinloch states [11]:

"...the locus of joint failure of adhesive joints when initially prepared is usually by cohesive fracture in the adhesive layer, or possibly in the substrate materials. However, a classic symptom of environmental attack is that after such attack, the joints exhibit some degree of apparently interfacial failure between the adhesive (or primer) and the substrate."

Hence, according to Kinloch, adhesive failure along the interface might be viewed as evidence for environmental attack. Borgmeier, in his Ph.D. dissertation, hypothesized that crack growth would tend to proceed along paths of maximum energy release rate [9]. Borgmeier used double cantilever beam (DCB) specimens, similar to those described in ASTM 3433, to check this

hypothesis. This specimen is similar to that shown schematically in Fig. 8. Testing is accomplished by using a universal testing machine to apply the forces (P) in Fig. 8.

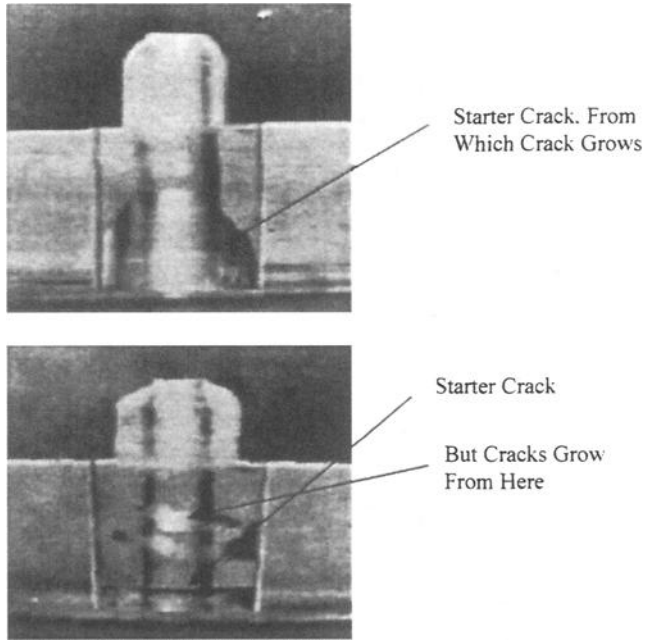


FIG. 7—Photographs of samples in the cone pull-out test showing difference in location of initial crack growth for 0° cylinder and 5° cone.

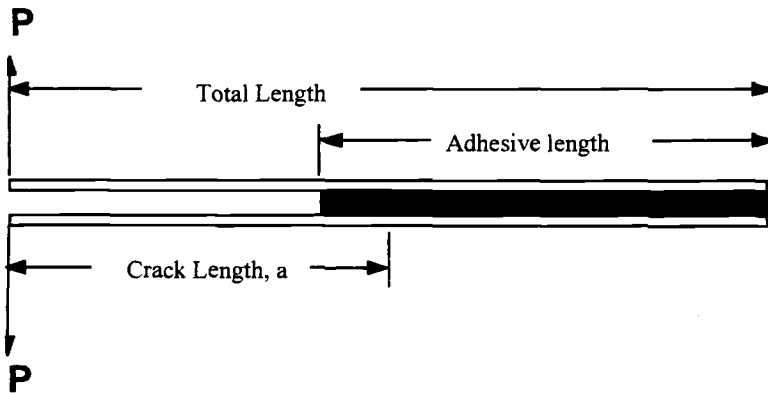


FIG. 8—Schematic of a typical geometry for DCB adhesive joint fracture specimens (shown with adherends of equal thickness) that was analyzed and experimentally tested. The forces (P) were applied by an Instron Universal Testing Machine.

Borgmeier used FEA/FMA to determine the path of ERR for varying geometries of DCB specimens (differing adherend thickness, differing adhesive thickness, and/or making one adherend thicker than the other). Section 11.1.1 in D 3433 provides the equation for the calculation of ERR, also known as G_{ic} , as $G_{ic} = [4L^2(\max)]/[3a^2 + h^2]/[E*B^2*h^3]$. This equation is based on beam theory assuming the energy absorbing parts of specimen are two cantilever beams “fixed” at the end of the crack. This analysis includes shear effects but ignores any energy in the beams beyond the end of the crack and more importantly, for this study, and energy that might be present in the adhesive. The FE/FM analysis used by Borgmeier includes all these effects. His analyses showed that, for some geometries, the max ERR was near the center of the adhesive. For others, it was near the interface. And, for still others, the ERR was relatively independent of the hypothesized path. DCB specimens were manufactured, using aluminum adherends and Hysol® 907 Epoxy adhesive, duplicating the geometry of the specimens analyzed. This epoxy was chosen because in independent bending experimental tests it exhibited relatively linear-elastic behavior up to its fracture point. The aluminum used was also well within its elastic region for the loads applied during the testing. Nearly 50 specimens of varying geometries were tested. In every case, the “adhesive failure cracks” proceeded along paths of max ERR as determined by the FE/FM analyses. This is illustrated in Fig. 9, which shows photographs of three samples after being pulled to failure. For samples with the geometry depicted in Fig. 9a, the analysis indicated that the path of max ERR was along the center of the adhesive. For samples of the type shown in Fig. 9b, the calculated ERR was largest near the bond-line between the metal and the epoxy. And, for the samples depicted in Fig. 9c, the ERR was relatively constant across the adhesive thickness. In each case (for 5–10 specimens of each of these specimen types), it was observed that cracks tended to follow paths of largest ERR. So it is observed that: a) in Fig. 9a, the specimen failed along the center of the adhesive, b) for Fig. 9b, the failure is near the metal, and c) for Fig. 9c (the specimen for which the ERR did not vary much across the adhesive thickness), the crack wanders, seeking a path of least resistance for reasons other than the ERR. These other reasons might be due to differences in density, molecular structure or morphology, the presence of minute cracks, air-holes, etc.

Conclusions

Scientists, engineers, and technicians have a myriad of tests available to characterize adhesives and adhesive joints. Fortunately, many of these have been formalized and standardized by such organizations as ASTM, so that different laboratories may use similar methods and obtain results that can more reliably be compared and used. The tests related to mechanical strength of joints are often generally characterized as tensile (including cleavage), peel, and shear. In actuality, however, the stress state for most tests is much more complex than it might first appear. Not only is the stress (magnitude) distribution non-uniform over the bonded area, but the nature of the stress is also complex. For example, the so called lap shear specimen, when loaded in the prescribed manner, experiences large tensile stresses near the bond termini. The usual way of presenting the results in lap joint tests (as well as tensile tests) is to report so called joint strength, that is, the force at failure (N or lb) divided by the bonded area (m^2 or in^2). Reporting test results as this “average stress” at failure has lead many designers to conclude that average stress criteria would be an adequate design rule for joint design. The use of such rules should be done only with considerable caution and care. In designing an adhesive joint, some of the parameters that might be considered are: 1) adhesive type and nature, 2) thickness of the

adhesive, 3) type of adherends, 4) thickness(es) of the adherends, 5) surface preparation of the bonded area, and 6) adhesive bond area.

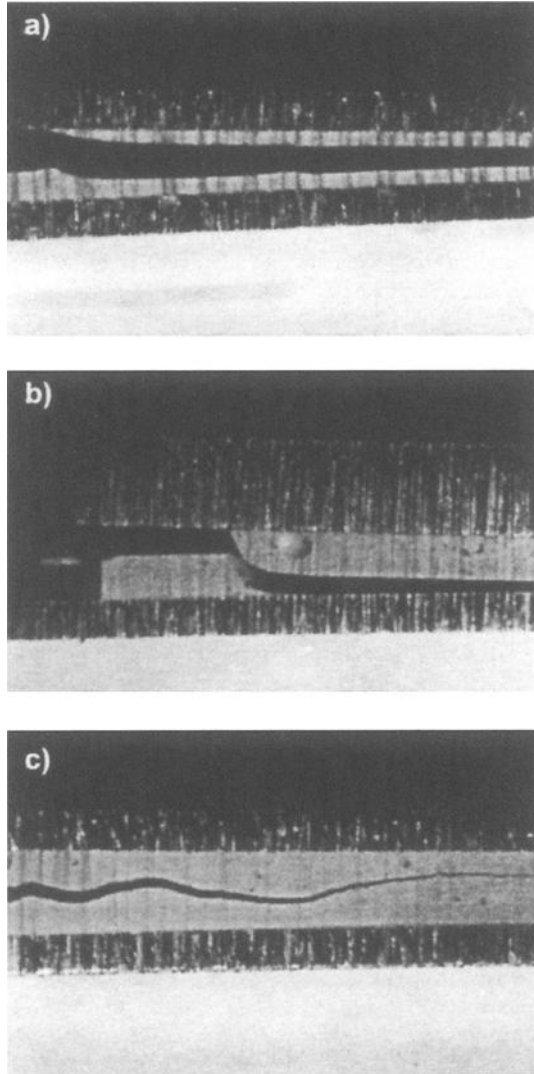


FIG. 9—Photographs of the side of DCB specimens after failure in which the FEA/FMA indicated that the path of max ERR was at: (a) the center of the adhesive, (b) the edge of the adhesive, and (c) relatively independent of location in the adhesive.

In general, for the lap specimen, doubling the bond area by increasing length of overlap will not result in a concomitant increase in the strength of a joint. While use of the standard lap specimens provides a good way of comparing joint strength between different adhesives, again caution should be used in making these comparisons. Joint strength is not only dependent on the nature of the adhesive and the amount of overlap but also such factors as listed at the end of the previous paragraph. This paper demonstrates that varying the adherend's thickness while keeping all parameters constant results in significant difference in the load at failure. That is, lap joints with a 25 mm width and 12.7 mm overlap length when the thickness of the adherends was increased from 1.6 to 3.2 mm experienced an increase in load at failure from 10.5 MPa to 16.8 MPa, which is an increase of 60 %.

In a similar manner, differences in adhesive thickness also complicate the comparison between adhesive joints. Say, for example, a person was comparing the lap joint strength of two adhesives in which the amount of overlap and the adherends were identical, but the thickness of the adhesives differed. If the first adhesive thickness was 1.3 mm and the second was 6.4 mm, the adhesive thickness effect would likely "swamp" any differences due to the adhesive type. Similar effects of thickness are noted for tensile tests. Not only does the relative thickness of the adhesive affect the load at failure, but it may also influence the point from which cracks are likely to grow.

The methods of Fracture Mechanics in conjunction with Finite Element analyses were explored as a means of explaining the observations described above. The agreement between the trends predicted by the analyses and the experimental observations are quite persuasive. Not only do the methods of analyses that were presented provide means of predicting the effect of the various parameters on the load at failure, but in some cases at least, they also yield insight into other behavior. FMA/FEA analyses could be used to predict the locus of crack growth "initiation" and the path along which the crack is most likely to proceed, at least for the cases studied. The authors hope to continue the study to include other specimen geometries and to explore how universal the utility of these methods of analysis might be.

References

- [1] *Adhesives - International Plastics Selector*, 6th ed., D.A.T.A. Publishing, San Diego, CA, 1991.
- [2] *Annual Book of ASTM Standards*, ASTM International, West Conshohocken, PA, published annually.
- [3] PTC, "Suggested Technique for Understanding the P-Version of the Finite Element Method," *PTC Knowledge Database*, <http://www.ptc.com/>.
- [4] Budinski, K. G., *Engineering Materials*, 3rd ed., Pearson Education Inc., NJ, 1989.
- [5] Anderson, G. P. and DeVries, K. L., "Analysis of Standard Bond-Strength Tests," *Treatise on Adhesion and Adhesives*, 6th ed., R. L. Patrick, Ed., Dekker, New York, 1989.
- [6] Griffith, A. A., *Philosophical Transaction of the Royal Society of London*, 221A, 163, 1921.
- [7] Rybicki, E. F. and Kanninen, M. F., *Engineering Fracture Mechanics*, 9, 931, 1977.
- [8] Van Tooren, M. J. L., Gleich, D. M., and Beukers, A., *J. Adhesion Sci. Technol.*, Vol. 18, 395, 2004.
- [9] DeVries, K. L. and Borgmeier, P. R., "Prediction of Failure in Polymeric Adhesives," *1st International Congress on Adhesion Science and Technology*, W. J. van Ooij and H. R. Anderson, Jr., Eds., 4-84, VSP, NL, 1998.

- [10] DeVries, K. L. and Borgmeier, P. R.. "Interpreting Adhesive Joint Tests." *2nd International Congress on Adhesion Science and Technology*, Ed. K.L. Mittal, 135. VSP. NL. 2002.
- [11] Kinloch, A. J., *Adhesion and Adhesives Science and Technology*. Chapman and Hall. New York. 1987.

Ming-Gin Lee,¹ Chui-Te Chiu,² and Yung-Chih Wang³

The Study of Bond Strength and Bond Durability of Reactive Powder Concrete

ABSTRACT: This research project aims to use reactive powder concrete, RPC, as a new repair material and evaluate its bond strength and bond durability to existing concrete. One accelerated aging environment, namely a freeze-thaw cycle acceleration deterioration test, was selected for the evaluation of bond durability of the repair materials. Before and after aging, the samples were evaluated by the compressive strength, bond strength (slant shear test), steel pull out strength, and relative dynamic modulus NDT tests.

The test results show that the RPC possesses high bond strength, dynamic modulus, and bond durability as compared with other concretes. The adhesion between the RPC and the steel is also much greater than that for the other concretes. It would be interesting to verify the consequences of this improved adhesion in reinforced concrete structures.

Test results revealed that RPC was still in good condition after 1000 cycles of freezing and thawing in accordance with ASTM C 666-97. After 1000 cycles, the nonshrinkage high strength mortar showed a reduction in compressive strength, slant shear strength, steel pull out strength, and dynamic modulus by 17, 21, 24, and 25 %, compared with the corresponding values of 6, 7, 5, and 10 %, respectively, for RPC. Specimens of normal strength concrete were used as reference specimens. The 5 cm × 10 cm slant shear cylinders made of normal strength concrete had deteriorated severely after 600–700 freeze-thaw cycles. For the normal strength concrete, the average values of relative dynamic modulus of elasticity based on resonant frequencies after 300 and 600 freeze-thaw cycles were 75 and 55 %, compared with the corresponding values of 96 and 92 %, respectively, for RPC.

KEYWORDS: bond strength, bond durability, freeze-thaw, reactive powder concrete, relative dynamic modulus

Introduction

In the modern age, a highly developed infrastructure is essential for economic growth and prosperity. Many structures essential to this infrastructure, especially those made of reinforced concrete, have suffered severe degradation since their construction due to the combined effects of deicing salts, freeze-thaw cycles, aggressive environments, and drastically increased live loads. One of the major problems facing the civil engineers of today is to preserve, maintain, and retrofit these structures [1].

The majority of concrete structures that require strengthening or rehabilitation are exposed to severe environmental conditions. Many of these severe circumstances are the result of cold

Manuscript received 18 August 2004; accepted for publication 6 January 2005; published July 2005. Presented at ASTM Symposium on Advances in Adhesives, Adhesion Science, and Testing on 4–6 October 2004 in Washington, DC.

¹Associate Professor, Department of Construction Engineering, Chaoyang University of Technology, Taichung County, 413, Taiwan, R.O.C. mglee@mail.cyut.edu.tw.

²Associate Professor, Department of Civil Engineering, Chung Hua University, Hsin Chu, 300, Taiwan, R.O.C.

³Associate Professor, Department of Civil Engineering, National Central University, Chung Li, 320, Taiwan, R.O.C.

climate conditions such as low temperature, freeze-thaw action, and exposure to deicing salts. Because of this, the environmental durability of both the bonding materials and methods used in rehabilitation applications are of utmost importance, especially in aggressive climates such as those found in north Asia and north America [2].

For concrete, deterioration due to freeze-thaw is caused by freezing of pore water inside the concrete. If the pores are too small, then the expansion caused by freezing can exert stresses on the concrete that crack the concrete and thus cause deterioration. Air entrainment of 7–8 %, depending on the aggregate size, can essentially eliminate this freeze-thaw damage [3].

However, very little research has been performed in evaluating the environmental durability of different repair materials for concrete members. Very little work has been done on the effects of freeze-thaw cycling on bonding and repair materials. Green, Bisby, Beaudoin, and Labossière [1] conducted durability tests on the bond between FRP and concrete, and found that the bond was not significantly damaged up to 300 freeze-thaw cycles. Lee and Wang [4] stated that the mechanical properties of reactive powder concrete, RPC, the ingredients of which are given in Table 1, showed high strength, toughness, and bonding strength. The RPC displayed excellent repair and retrofit potentials. Using RPC and CFRP on strengthening concrete members could give excellent retrofit effects, but material costs are different for these two materials. The improved properties of RPC are achieved by the following methods [4,5]:

- Improvement of the material homogeneity by removing all coarse aggregates.
- Increase of the compactness by granular optimization and compaction.
- Possible improvement of the microstructure by heat treatment.
- Achievement of material ductility by the addition of steel fibers.
- Reducing the amount of water in the concrete.
- Extensive use of highly refined silica fume.
- Optimum chemistry of all components [2,4].

TABLE 1—*Mix design of RC, HSM, and RPC.*

| Materials (kg/m ³) | Cement | Stone | Sand | Silica Sand | Silica Fume | Crushed Quartz | Steel Fiber | Super- plasticizer | Total Water |
|-----------------------------------|------------------------|-------|------|----------------|----------------|-------------------|----------------|-----------------------|----------------|
| RC | 342 | 926 | 785 | - | - | - | - | - | 222 |
| HSM | HSM : Water = 1 : 0.15 | | | | | | | | |
| RPC | 720 | - | - | 900 | 216 | 252 | 40 | 71.3 | 133.7 |

The RPCs have a remarkable flexural strength and very high ductility; their ductility is greater than 250 times that of conventional concrete [6–7]. Their extremely low porosity gives them low permeability and high durability, and makes them potentially suitable for being used in a new technique for retrofitting reinforced concrete structures [7].

The main aim of the work presented here is to assess the performances of RPC, as a new repair material and to evaluate the strength and durability of its bond to existing reinforced concrete.

Experiments

Laboratory freezing and thawing tests on concrete specimens are carried out to evaluate RPC as a new repair material for concrete structures and the strength and durability of its bond to existing structures.

Materials

The two cement-repair materials, which were used as references in this study, are representative of concretes with regular strength on one hand and very high strength on the other. The mix design of the regular concrete (RC) with a compressive strength of 30 MPa contains no admixture and yields a slump of 150 mm. The nonshrinkage high strength mortar (HSM), with a ready-mix formula, contains 10 % silica fume. Its compressive strength is high, and its low water cement ratio assures good durability. The characteristics of these two cement-repair materials are provided in Table 1.

The RPC to be used as a prospective repair material contains a Type II cement, silica fume, silica sand, quartz powder, steel fiber, and a superplasticizer. The mix design of the RPC repair material is also displayed in Table 1. The flexural strength of RC in comparison with its repair materials is shown in Table 2. The bending beams had dimensions of 100 mm × 100 mm × 350 mm as shown in Fig. 1.

Tests performed in this experimental study included abrasion resistance, compressive strength, bond strength (slant shear test), steel pull out strength, and relative dynamic modulus NDT tests.

TABLE 2—*Bending strength of RC in comparison with its repair materials.*

| Materials Curing duration | RC | HSM | RPC | HSM/RC ^a | RPC/RC ^a |
|------------------------------|-----|-----|------|---------------------|---------------------|
| 7 days | 4.7 | 4.3 | 16.3 | 4.6 | 7.2 |
| 28 days | 5.9 | 5.3 | 19.7 | 5.4 | 8.0 |

The dimension of specimens is 100 mm × 100 mm × 350 mm with bonding repair material (HSM or RPC) of 10 mm thickness.

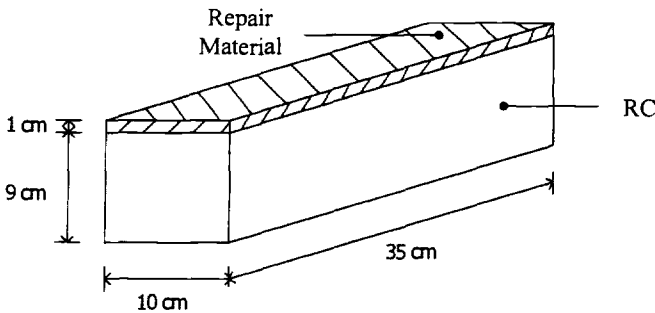


FIG. 1—*Specimen configuration for bending tests.*

Experimental Procedure

This research project aims to use three different concretes, RC, HSM, and RPC, as repair materials and evaluate their bond strength and bond durability to existing reinforcement concrete structure. One accelerated aging environment, namely the freeze-thaw cycle acceleration deterioration test, was selected for the evaluation of bond durability of bonding materials. Freeze-thaw cycling of all specimens was conducted using the cold climate testing facilities at Chaoyang University of Technology in Taiwan. Freeze-thaw cycles were applied to the blocks at a rate of one cycle/185 min, in accordance with ASTM C 666-97, Test Method for Resistance of Concrete to Rapid Freeze and Thawing, with 1.5 h of freezing in cold air at -18°C followed by 1.5 h of thawing in cool air at $+4.4^{\circ}\text{C}$. Specimens that were not subjected to freeze-thaw cycling were stored in the material testing laboratory by immersing in saturated lime water for 24 h prior to testing. The specimens were divided into groups of three, with groups subjected to 0, 300, 600, or 1000 freeze-thaw cycles.

Before and after freeze-thaw cycling, the samples were tested for their compressive strength, bond strength (slant shear test), steel pull out strength, and relative dynamic modulus.

Test Specimens Fabrication

For the steel pull out tests, a total of 24 concrete cylinders were used. A No. 3 reinforcing steel bar coated with epoxy was inserted in the center of a concrete cylinder, 50 mm in diameter and 100 mm in height, as shown in Fig. 2. Similar cylinders but with no steel bar were made for testing according to ASTM C 131, Test Method for Resistance to Degradation of Small-Size Coarse Aggregate by Abrasion and Impact in the Los Angeles Machine, Aggregate Abrasion Testing Procedure by Use of Los Angeles Machine, and for measurement of the variation in slant shear strength refer to ASTM C 882-99, Test Method for Bond Strength of Epoxy-Resin Systems Used with Concrete by Slant Shear, as shown in Fig. 3. The slant shear test measures the shear bond between the repair material and the substrate at an inclined angle of 45° , and is used by most manufacturers of repair materials to evaluate product performance. The surface preparation of substrate concrete was sandblasting before placing the repair material. The test is economical and can be easily reproduced.

The beams, fabricated in the material testing laboratory, having dimensions of $7.5\text{ cm} \times 7.5\text{ cm} \times 30\text{ cm}$ were tested for relative dynamic modulus in accordance with ASTM C 666-97. Three-inch cubes were sawn from each of the beams after the relative dynamic modulus test. The cubes were tested using procedures presented in ASTM C 116-90, Test Method for Compressive Strength of Concrete Using Portions of Beams Broken in Flexure. When the specimens were 28 days old, the freeze-thaw durability specimens were cured in lime-saturated water until testing was begun.

The experimental program was conducted to determine the effects of freeze-thaw cycling on the durability of bond between bonding materials and concrete.

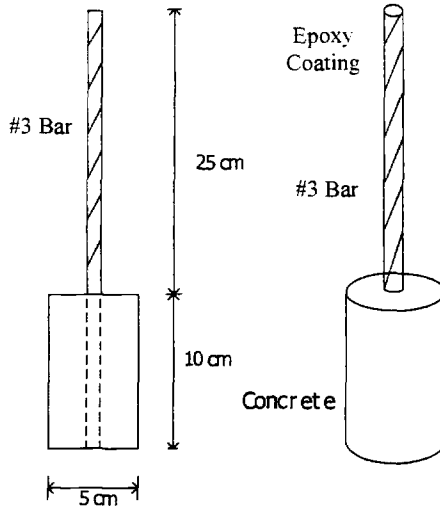


FIG. 2—Specimen configuration for pull-off tests.

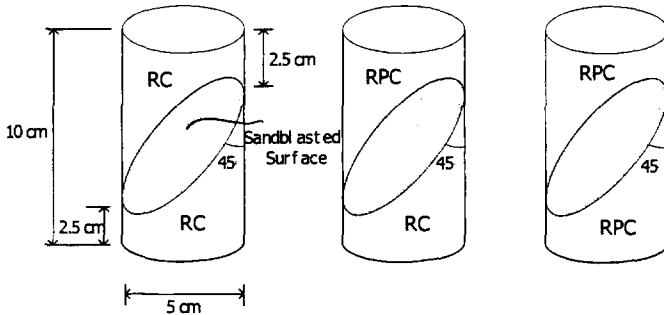


FIG. 3—Specimen configuration for slant shear tests.

Experimental Results and Discussion

Resistance to Abrasion

Abrasion coefficients were measured in accordance with ASTM C 131-96, Aggregate Abrasion Testing Procedure. After undergoing 500 and 1000 cycles of abrasion, the weight of the specimen was measured. This weight was then compared with the one obtained before abrasion testing in order to determine the abrasion coefficient (W/W_0). The abrasion coefficients for different concrete specimens are presented in Table 3. After undergoing 500 and 1000 cycles of abrasion, the normal strength concrete cylinders showed a reduction in weight of 32 % and 67 % compared with the corresponding values of 5 % and 8 % for RPC. The abrasion resistance of RPC is about eight times higher than that of normal strength concrete and about four times higher than that of HSM.

TABLE 3—Abrasion coefficients measured with ASTM C 131 aggregate abrasion testing procedure.

| Duration \ Materials | RC | HSM | RPC |
|----------------------|------|------|------|
| 500 cycles | 0.68 | 0.86 | 0.95 |
| 1000 cycles | 0.33 | 0.67 | 0.92 |

Dynamic Modulus of Elasticity

Concrete subjected to freeze-thaw cycling may suffer from micro cracks and surface scaling. Dynamic modulus of elasticity was measured to evaluate the degree of deterioration in the concrete cylinders. A decrease in dynamic modulus indicates that the concrete is internally deteriorating by micro cracks and/or surface scaling.

The changes of relative dynamic modulus (E/E_0) for concrete cylinders subjected to freeze-thaw cycling up to 1000 cycles are given in Table 4. The results show that the relative dynamic modulus increased significantly at the early stages due to continuous hydration of cement and/or pozzolanic reaction of silica fume. A steady decrease in relative dynamic modulus then occurred after 300 cycles of freezing and thawing. The 7.5 cm \times 7.5 cm \times 30 cm beams made of normal strength concrete had surface cracking after 600–1000 freeze-thaw cycles. For the normal strength concrete specimens, the average values of the relative dynamic modulus of elasticity based on resonant frequencies at 300, 600, and 1000 cycles were 75, 55, and 39 %, respectively, compared with the corresponding values of 96, 92, and 90 %, respectively, for RPC.

TABLE 4—Ratio of dynamic modulus (E/E_0) of RPC in comparison with RC and HSM.

| Duration \ Materials | 28 Days + 100 Cycles | 28 Days + 300 Cycles | 28 Days + 600 Cycles | 28 Days + 1000 Cycles |
|----------------------|-------------------------|-------------------------|-------------------------|--------------------------|
| RC (MPa) | 1.11 | 0.75 | 0.55 | 0.39 |
| HSM (MPa) | 1.08 | 0.90 | 0.84 | 0.78 |
| RPC (MPa) | 1.03 | 0.96 | 0.92 | 0.90 |

Compressive Strength

Following the completion of ASTM C 666-97 testing, the freeze-thaw beams from the RC, HSM, and RPC mixtures were sawn into 3-in. concrete cubes from each of the beams after resonant frequency testing. The 3-in. concrete cubes were tested using the procedures presented in ASTM C 116-90.

The strength development of the three mixtures before and after the freeze-thaw testing is presented in Fig. 4 and Table 5. Results show that a steady decrease in compressive strength was then followed after 300 cycles of freezing and thawing, with the exception of the RPC cubes, which increased in compressive strength at 300 cycles of freezing and thawing. This increase in strength of the RPC specimens might be caused by continuous hydration of cement and/or pozzolanic reaction of silica fume. The 7.5 cm \times 7.5 cm \times 30 cm beams made of normal strength concrete had surface cracking after 600–1000 freeze-thaw cycles. For the normal strength concrete cubes, the average values of the compressive strength at 300, 600, and 1000 cycles of freezing and thawing were 90, 67, and 43 %, respectively, compared with the corresponding values of 98, 90, and 84 %, respectively, for HSM, and compared with the corresponding values of 103, 99, and 94 %, respectively, for RPC.

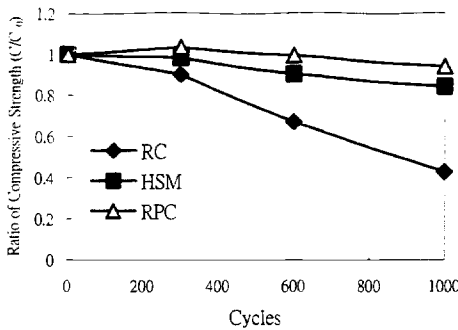


FIG. 4—Ratio of compressive strength of RPC in comparison with RC and HSM.

TABLE 5—Compressive strength of RPC in comparison with RC and HSM.

| Materials \ Duration | Duration | | | |
|----------------------|----------|----------------------|----------------------|-----------------------|
| | 28 Days | 28 Days + 300 Cycles | 28 Days + 600 Cycles | 28 Days + 1000 Cycles |
| RC (MPa) | 34.1 | 30.7 | 22.8 | 14.5 |
| HSM (MPa) | 65.8 | 64.6 | 59.4 | 55.3 |
| RPC (MPa) | 181.6 | 187.5 | 180.3 | 170.2 |

After 1000 freeze-thaw cycles, the normal strength concrete cubes showed a reduction in compressive strength of 57 % compared with the corresponding values of 6 % for RPC.

In general, factors influencing strength development of the concrete cubes in this research were:

1. Cement hydration and pozzolanic reaction of silica fume that increased the concrete strength;
2. Suspension of cement hydration by the low-temperature curing;
3. Pore pressure of ice formation from freeze-thaw cycling that might induce micro cracks and reduce strength.

The measured strength of the concrete cubes was controlled by the interaction and combination of the above mechanisms. Strength reduction was noted after 600 and/or 1000 freeze-thaw cycles due to freeze-thaw damage.

Steel Bond Strength and Failure Type

The changes of steel bond strength for the concrete cylinders with inserted steel bars up to 1000 freeze-thaw cycles are given in Fig. 5 and Table 6. The results show that the steel bond strength of RC and HSM decreased significantly with freeze-thaw cycling as compared with that of RPC. For the normal strength concrete specimens, the average values of the steel bond strength at 0 and 1000 cycles were 6.21 and 4.05 MPa, respectively, compared with the corresponding values of 12.7 and 12.09 MPa, respectively, for RPC.

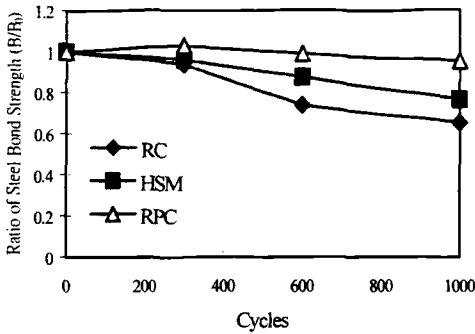


FIG. 5—Ratio of steel bond strength of RPC in comparison with RC and HSM.

TABLE 6—Steel bond strength and failure type of RPC in comparison with RC and HSM.

| Duration | | 28 Days | 28 Days + 300 Cycles | 28 Days + 600 Cycles | 28 Days + 1000 Cycles |
|----------|---------------------|---------------|----------------------|----------------------|-----------------------|
| RC | Bond Strength (MPa) | 6.21 | 5.82 | 4.58 | 4.05 |
| | Failure Type | Split Failure | Split Failure | Split Failure | Split Failure |
| HSM | Bond Strength (MPa) | 9.21 | 8.84 | 8.05 | 7.05 |
| | Failure Type | Split Failure | Split Failure | Split Failure | Split Failure |
| RPC | Bond Strength (MPa) | 12.70 | 13.05 | 12.55 | 12.09 |
| | Failure Type | Bond Failure | Steel Break off | Steel Break off | Bond Failure |

There were three different failure modes in this steel pull out test. The failure mode for RC and HSM was a split failure. The failure modes for RPC included bond failure and steel break off. RC and HSM specimens had relatively lower steel bond strength, while RPC specimens still had relatively higher values after 1000 freeze-thaw cycles. It can be concluded that the steel bond strength of RPC is almost 3 times that of the conventional concrete after 1000 freeze-thaw cycles.

Slant Shear Strength and Failure Type

The changes of slant shear strength for the different combinations of concretes after freeze-thaw cycling up to 1000 cycles are given in Fig. 6 and Table 7. The results show that the bond strength of RC/RC, HSM/RC, and RPC/RC decreased by a significantly higher amount with freeze-thaw attack as compared with that of RPC/RPC. The RC/RC specimens had deteriorated severely after 600–1000 cycles. For the RC/RC specimens, the average values of bond strength at 0 and 1000 cycles were 12.4 and 3.8 MPa, respectively, compared with the corresponding values of 59.6 and 57.6 MPa, respectively, for RPC/RPC.

There were three different failure modes in this slant shear test. The failure type for RC/RC specimens was interface failure. The failure modes for RPC/RPC specimens included repair material failure and substratum failure. The failure modes for HSM/RC and RPC/RC specimens were interface failure or substratum failure. RC and HSM specimens have relatively lower concrete bond strength, while RPC specimens still have relatively higher values after 1000 freeze-thaw cycles.

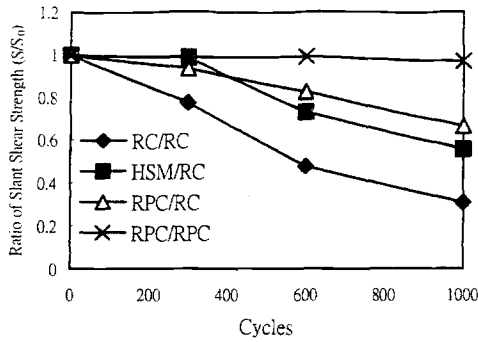


FIG. 6—Ratio of slant shear strength of RPC in comparison with RC and HSM.

TABLE 7—Slant shear strength and failure type of RPC in comparison with RC and HSM.

| Repair Material/Substratum | | Duration | | | |
|----------------------------|----------------------------|--|----------------------|----------------------|-----------------------|
| | | 28 Days | 28 Days + 300 Cycles | 28 Days + 600 Cycles | 28 Days + 1000 Cycles |
| RC/RC | Slant Shear Strength (MPa) | 12.4 | 9.6 | 5.9 | 3.8 |
| | Failure Type | Interface Failure | | | |
| HSM/RC | Slant Shear Strength (MPa) | 12.6 | 12.4 | 9.2 | 7.0 |
| | Failure Type | Substratum Failure | | Interface Failure | |
| RPC/RC | Slant Shear Strength (MPa) | 13.7 | 12.8 | 11.3 | 9.1 |
| | Failure Type | Substratum Failure | | | Interface Failure |
| RPC/RPC | Slant Shear Strength (MPa) | 59.6 | 58.9 | 59.0 | 57.6 |
| | Failure Type | Repair Material and Substratum Failure | | | |

In this study, the results show that the RPC specimens not only enhanced bond strength but also helped to increase bond durability when compared with that of RC and HSM specimens subjected to the same environmental condition.

Summary

The main findings from this study are summarized as follows:

1. The abrasion coefficient of RPC is about eight times higher than that of normal strength concrete and about four times higher than that of HSM.
2. All concretes generally exhibit drastic loss in compressive strength, bond strength, and dynamic modulus of elasticity after 1000 freeze-thaw cycles.

3. The results of relative dynamic modulus and compressive strength tests after 1000 freeze-thaw cycles indicate that RPC is more sound than HSM and RC. under the environmental conditions used in this study.
4. The results of steel pull out tests show that the RPC not only enhances steel bond strength but also helps to increase bond durability. The strength and durability of bond of RPC to steel are much better than those of RC and HSM specimens subjected to the same environmental conditions.
5. The results of slant shear tests show that the bond strength of RC/RC, HSM/RC, and RPC/RC decreased significantly more with freeze-thaw cycling as compared with that of RPC/RPC.

Acknowledgments

This research was supported by the National Science Council in Taiwan R.O.C. under contract No. NSC 91-NU-7-324-001. The authors wish to acknowledge the assistance of Dr. Mang Tia.

References

- [1] Green, M. F., Bisby, L. A., Beaudoin, Y., and Labossière, P., "Effect of Freeze-thaw Cycles on the Bond Durability between Fibre Reinforced Polymer Plate Reinforcement and Concrete," NRC Canada, *Journal of Civil Engineering*, Vol. 27, 2000, pp. 949-959.
- [2] Neville, A. M., *Concrete Maintenance and Repair*, John Wiley & Sons, Inc., New York, NY, 1995.
- [3] Neville, A. M., *Properties of Concrete*, John Wiley & Sons, Inc., New York, NY, 1995.
- [4] Lee, M. G. and Wang, Y. C., "A Preliminary Study of Strengthening Concrete Members Using Reactive Powder Concrete," *Journal of Chinese Civil and Hydraulic Engineering*, Vol. 16, No. 4, 2004, pp. 1-9.
- [5] Roux, N., Andrade, C., and Sanjuan, M., "Experimental Study of Durability of Reactive Powder Concrete," *Journal of Materials in Civil Engineering*, Vol. 8, No. 1, February 1996.
- [6] Bonneau, O., Lachemi, M., Dallaire, E., Dugat, J., and Aitcin, P. -C., "Mechanical Properties and Durability of Two Industrial Reactive Powder Concretes," *ACI Materials Journal*, Vol. 94, No. 4, July-August 1997, pp. 286-290.
- [7] Richard, P. and Cheyrezy, M., "Composition of Reactive Powder Concrete," *Cement and Concrete Research*, Vol. 25, No. 7, 1995, pp. 1501-1511.
- [8] Alaei, F. J., "Retrofitting of Concrete Structures using High Performance Fiber Reinforced Cementitious Composite (HPFRCC)," Ph.D. Thesis, University of Wales, Cardiff, 2001.

Shin-Che Huang,¹ Thomas F. Turner,¹ Adam T. Pauli,¹ Francis P. Miknis,¹ Jan F. Branthaver,²
and Raymond E. Robertson¹

Evaluation of Different Techniques for Adhesive Properties of Asphalt-Filler Systems at Interfacial Region

ABSTRACT: Asphalt is a widely variable product used in public roadways at the rate of 30 million tons per year and is thus the largest volume of adhesive used in any application. Considering the commercial importance of asphalt, several analytical techniques were employed to investigate its adhesive properties. These techniques include the specially designed sliding plate viscometer, differential scanning calorimetry (DSC), atomic force microscopy (AFM), liquid chromatography, centrifugation, and infrared (IR) spectroscopy. The specially designed sliding plate rheometer was used to measure the rheological properties of asphalt film in contact with aggregate surface at thin film levels. DSC was applied to measure the effect of fine particles on the low temperature properties. AFM was used to produce a photo-like image of adhesion between asphalt and mineral fines. Chromatography and centrifugation techniques were used to separate the adsorbable, polar asphalt components from aggregate surfaces. Infrared spectroscopy was used to determine the quantities and natures of adsorbed molecules. The results of these asphalt-aggregate experiments have shown what types of organic molecules in asphalt adsorb onto aggregate surfaces. Aggregates are shown to adsorb large concentrations of the most polar functional groups found in asphalts. In addition, the theory of Interfacial Morphological Stability has been used to model air-asphalt film and asphalt film-glass substrate interfacial systems. Separately, a wet-packing chromatographic technique was developed to use pulverized aggregate to separate cyclohexane solutions of asphalt into polar and non-polar components. Furthermore, the DSC evidence suggests the immobilization of a surface layer of binder in contact with aggregate induces a large rigid, amorphous fraction of the binder. These methods have been employed to characterize the fundamentals of asphalt-aggregate interaction in order to devise improved road performance predictive tests.

KEYWORDS: asphalt, binder, asphalt-aggregate interaction, adhesion, chromatography, centrifugation, sliding plate viscometer, differential scanning calorimetry, atomic force microscopy

Introduction

Asphalt is a product of the fractional distillation of petroleum. This fractional distillation process can occur over a long period of time in nature resulting in deposits of material known as natural asphalts or in a short period of time in the refinery resulting in manufactured asphalts. Asphalts vary in consistency from solid materials at room temperature to materials whose

Manuscript received 1 September 2004; accepted for publication 3 November 2004; published May 2005. Presented at ASTM Symposium on Advances in Adhesives, Adhesion Science, and Testing on 4-6 October 2004 in Washington, DC.

¹ Western Research Institute, 365 North 9th Street, Laramie, WY 82072-3380.

² 9 Parkview Lane, Chatham, IL 62629.

*Disclaimer: This document is disseminated under the sponsorship of the Department of Transportation in the interest of information exchange. The United States Government assumes no liability for its contents or use thereof. The contents of this report reflect the views of Western Research Institute, which is responsible for the facts and the accuracy of the data presented herein. The contents do not necessarily reflect the official views of the policy of the United States Department of Transportation. Mention of specific brand names of equipment does not imply endorsement by the United States Department of Transportation or Western Research Institute.

consistency is practically the same as water at high temperature. For road mixes, too solid an asphalt lacks the necessary fluidity for workability and is susceptible to low temperature cracking, whereas too soft an asphalt may bleed to the surface or develop potholes and rutting under traffic. It is critical to have adequate consistency to ensure good workability and performance during service.

The mineral aggregate components of pavements are distributed throughout a mixture and range in size from coarse to fine. Properly compacted asphaltic mixtures produce a structure whose stability, stiffness, and wearing properties are dependent on the interlocking of the aggregate particles and the cohesiveness of the binder. Only the portion of the mineral filler consisting of particles thicker than the asphalt film contributes to the interlocking of the aggregate. The other portion of the filler, the fine particles smaller than the thickness of the asphalt film, is suspended in the asphalt and is part of the binder component of the mixture.

The asphalt-aggregate interaction is a thin-film phenomenon. A number of testing procedures have been used to attempt to measure rheological properties of thin films. The mechanical tests that are used in rheological measurements such as dynamic shear rheometer, bending beam rheometer, Brookfield viscometer, and direct tension test, for the most part, measure bulk properties. Thus, there is little basis for choosing one over another from the standpoint of application to thin-film properties. It is important to investigate the asphalt-aggregate interaction in the interfacial region to determine if this interaction relates to pavement distresses such as moisture damage, tender mix, permanent deformation, fatigue cracking, and low temperature cracking.

It is hypothesized that fine aggregate particles (mineral fillers) function as more than just inert particles in asphalt, and that physico-chemical interactions occur between asphalt and mineral fillers that affect pavement performance. Further, it is speculated that these physico-chemical interactions are three-way interdependent interactions of fine particles, asphalt, and larger aggregates. It is expected that the adhesion of the fine particle-asphalt binder to larger aggregate particles would be affected by the compositional characteristics and quantity of the fillers. With the use of larger quantities of fine particles or with the use of improper fine particles, adhesion may be critically affected, particularly when the paving mixture is exposed to the action of water, oxygen, or sunlight. In such an environment, the bond between asphalt binder and mineral aggregate may be weakened or even destroyed. This would lead to a poorly performing paving mixture.

It is assumed that contact between mineral fines and asphalts results in migration of polar organic asphalt molecules to polar sites on mineral surfaces. This aggregate induced interaction results in changes in asphalt microstructures. Currently, no standard binder test is in use to determine the aggregate-induced effects of asphalt microstructure on the rheological properties of asphalt binders (adhesion), nor is there a mixture test that determines the contribution of these physicochemical effects on the properties of asphalt-aggregate mixtures.

The objectives of this research were: 1) to develop a reliable procedure for characterizing important properties of asphalt mastics and 2) to develop a method that enables the interactions between thin asphalt layers and various aggregate surfaces to be predicted. The practical result of this study hopefully will be an improvement in the prediction of hot-mix-asphalt (HMA) performance by better characterization of asphalt thin-film behavior, which is known to vary significantly with the compositions of both asphalt and aggregate. The methodologies that are being used are: 1) to investigate the interaction between asphalt and the surface of the filler to determine how the aggregate alters the physical properties of asphalt, 2) to quantify any such

interaction and correlate readily measurable chemical properties with physical properties, and 3) to develop a test to characterize the behavior of mastics (asphalt at thin films) and therefore be able to improve Superpave® specifications.

Materials

The asphalts selected for study were the so-called Strategic Highway Research Program (SHRP) core asphalts. They are coded using three capital letters followed by an Arabic numeral. Some properties of the asphalts are listed in Table 1. Of particular interest are asphaltene and saturate contents, because these parameters relate to asphalt compatibility. In general, compatible asphalts are low in asphaltene content. Asphalts with high asphaltene contents are classified as not compatible. Of the eight asphalts listed in Table 1, AAG-1 (a lime-treated asphalt) and AAM-1 would be classified as highly compatible. AAD-1 and AAK-1 would be least compatible. The other four asphalts are intermediate. It is speculated that the property of compatibility will critically influence the interaction of an asphalt with mineral fines.

The aggregate fillers used in this study were prepared by crushing SHRP aggregates and collecting the particles passing through a #200 (75 micron) sieve.

TABLE 1—Physical and chemical properties of selected asphalts [1].

| Sample | AAA-1 | AAB-1 | AAC-1 | AAD-1 | AAF-1 | AAG-1 | AAK-1 | AAM-1 |
|-----------------------------|-------|-------|-------|-------|-------|-------|-------|-------|
| Viscosity, 60°C. Pa·s (AV*) | 86.4 | 102.9 | 41.9 | 105.5 | 187.2 | 186.2 | 325.6 | 199.2 |
| Component Analysis (Cb*) | | | | | | | | |
| Asphaltene (n-heptane) | 16.2 | 17.3 | 10.1 | 20.5 | 13.3 | 5.0 | 20.1 | 4.0 |
| Polar Aromatic | 37.3 | 38.3 | 37.4 | 41.3 | 38.3 | 51.2 | 41.8 | 50.3 |
| Napthene Aromatic | 31.8 | 33.4 | 37.1 | 25.1 | 37.7 | 32.5 | 30.0 | 41.9 |
| Saturates | 10.6 | 8.6 | 12.9 | 8.6 | 9.6 | 8.5 | 5.1 | 1.9 |
| Elemental Analysis | | | | | | | | |
| C, % | 83.9 | 82.3 | 86.5 | 81.6 | 84.5 | 85.6 | 83.7 | 86.8 |
| H, % | 10.0 | 10.6 | 11.3 | 10.8 | 10.4 | 10.5 | 10.2 | 11.2 |
| O, % | 0.6 | 0.8 | 0.9 | 0.9 | 1.1 | 1.1 | 0.8 | 0.5 |
| Nitrogen, % | 0.5 | 0.54 | 0.66 | 0.77 | 0.55 | 1.10 | 0.7 | 0.55 |
| Sulfur, % | 5.5 | 4.70 | 1.90 | 6.90 | 3.4 | 1.30 | 6.4 | 1.2 |
| Vanadium, ppm | 174 | 220 | 146 | 310 | 87 | 37 | 1480 | 58 |
| Nickel, ppm | 86 | 56 | 63 | 145 | 35 | 95 | 142 | 36 |
| Molecular Weight (VPO*) | 790 | 840 | 870 | 700 | 840 | 710 | 860 | 1300 |
| % Wax (INTEVEP) | 1.62 | 3.85 | 5.06 | 1.94 | 4.19 | 1.13 | 1.17 | 4.21 |

* AV = Absolute viscometer, Cb = Corbett, VPO = Vapor Phase Osmometry.

Chemical Characterization by Chromatography

Tests based on chromatographic techniques were undertaken to evaluate the interactions between asphalts and the surfaces of mineral fillers. The mineral fillers (mixed with a filter aid) serve as the solid support in chromatographic columns. Asphalt solutions in cyclohexane are percolated through the columns [2]. Polar organic molecules in the asphalt become adsorbed on the mineral particles, while non-polar components wash away. The polar organic components were desorbed by a stronger solvent than cyclohexane and then were dried and weighed. Weights of polar organic materials collected were observed to be a function of the particular asphalt-aggregate combination. In general, smaller amounts of polar organics were collected

from compatible asphalts than from non-compatible asphalts. The influence of the aggregate also was observed to be substantial. One granite adsorbed relatively small amounts of polar organics from those core asphalts tested. A greywacke and a high surface-area limestone adsorbed relatively large amounts of polar organic materials from the asphalts. It is assumed that this procedure mimics the interactions of asphalt polar components with mineral surfaces in pavements that take place over longer periods of time. It also is assumed that polar organic constituents of asphalts are the critical components involved in adhesion to mineral surfaces and in binder cohesion. If too few polar organics interact with mineral surfaces, adhesion would be expected to be poor. On the other hand, if too many polar organics are removed from an asphalt, cohesion might be adversely influenced.

Figure 1 shows the infrared (IR) spectra in carbon disulfide solvent of the polar organic materials that were desorbed from a cyclohexane solution of AAB-1 by a pulverized (+200 mesh) California granite. These polar materials were desorbed from the aggregate by a polar solvent. Of particular interest are the carbonyl absorbances at $\sim 1700\text{ cm}^{-1}$. In carbon disulfide, carboxylic acids form dimers that adsorb at 1700 cm^{-1} ; thus, in this solvent carboxylic acids and ketones both absorb at $\sim 1700\text{ cm}^{-1}$ [3]. Therefore, the relative amounts of each functional group cannot be determined from this spectrum. Previous work, however, has shown that carboxylic acids are highly concentrated on aggregate surfaces even though their concentration is low in the neat asphalt [4,5]. The nearby 1655 cm^{-1} peak is evidence of the presence of 2-quinolone type compounds [6]. Sulfoxides, which are major products of asphalt oxidative aging, are characterized by an IR peak at 1030 cm^{-1} . These three functional group types are the ones of paramount interest. Other features of note in the IR spectra are the three peaks between 900 and 700 cm^{-1} , characteristic of hydrogen bending vibrations of aromatic molecules. The broad band over the range of $3400\text{--}3000\text{ cm}^{-1}$ results from the hydrogen bonding of phenols, pyrroles, and carboxylic acids [7]. Hydrogen bonding of hydroxyl (OH) groups with the OH groups on the surface of siliceous aggregate would be particularly expected. Hydrogen bonding interactions, which are comparatively strong, are characteristic of polar molecules and would be expected to contribute significantly to interactions between asphalts and aggregates.

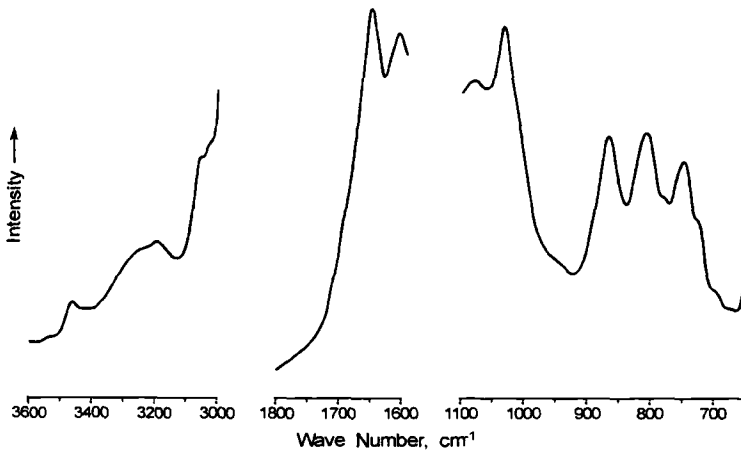


FIG. 1—Infrared spectra analysis on polar organic fraction that is extracted from AAB-1/California (filler) granite mixture.

The IR spectrum shown in Fig. 1 and other spectra of polar organics obtained from different asphalt-aggregate combinations demonstrate that molecules with polar functional groups become concentrated on mineral surfaces in these experiments and can be isolated and further studied to determine their involvement in adhesion and other phenomena.

Physical Characterization by Centrifugation

The objective of this experiment was to investigate whether a large volume, cylindrical (23 mm \times 11 mm I.D.) high-speed nuclear magnetic resonance (NMR) sample spinner could be developed into a rapid, reliable, and simple method to isolate polar organic fractions that adhered to aggregate surfaces. Spinning is achieved by supplying air pressure to a bearing to keep the spinner away from the walls of the spinner housing, and to a drive tip to achieve the desired spinning rates. Stripping experiments were carried out for spinning rates ranging from 1–4 kHz (1 kHz = 60 000 rpm) at ambient temperature. Spinning and drive pressures were determined experimentally. To achieve a spinning frequency of 4 kHz, the bearing and drive pressures were 10 and 33 psi, respectively. Initial experiments were conducted using asphalts, AAA-1, AAG-1, and AAK-1 that were mixed in roadway proportions with glass beads. The glass beads had a nominal size of 1 and 3 mm. It is not expected that polar organic fractions of asphalts will interact with glass beads as strongly as with pavement aggregates. Experiments were conducted for spinning times from 10–30 min and spinning rates from 1–4 kHz. Experiments conducted at 4 kHz for 10 min with 1 mm glass beads showed that a substantial portion of the asphalt was centrifuged out of the asphalt-bead matrix, leaving only a thin film of asphalt covering the beads. Figure 2a shows results from a typical spinning experiment using asphalt AAG-1 coated onto 3 mm glass beads. The photographs were taken using a Kodak 260 digital camera. This example clearly shows that spinning removes a significant amount of asphalt from the beads.

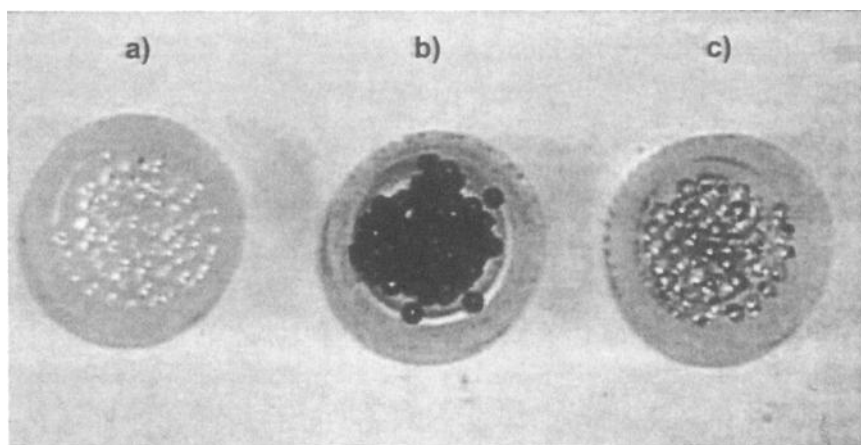


FIG. 2a—Asphalt AAG coated onto 3 mm glass beads: a) glass beads, b) glass beads coated with asphalt, c) glass beads after spinning at 3 kHz for 30 min, then at 4 kHz for 60 min.

The amount of material remaining on the 1 mm glass beads was determined as a function of spinning speed. The results are given for material closest to the center of the spinner. The amount of material retained on the glass beads was determined by burning off the organic material in a muffle oven and determining the weight loss. The amount of material remaining was normalized to the starting material to obtain a percentage of material retained. A plot of the percentages of asphalt remaining on the 1 mm glass beads after spinning at 4 kHz for 30 min is shown in Fig. 2b. As seen from the figure, more material was retained by asphalt AAK-1 than by AAA-1 and AAG-1. This might be interpreted to be the result of the viscosity function since AAK-1 was the most viscous of the three asphalts studied. However, this possibility seems less likely by the fact that asphalt AAG-1 is more viscous than asphalt AAA-1, yet more material was left on glass beads in contact with AAA-1. The most plausible explanation as to why the AAK-1 has the highest percent of retained asphalt components on glass beads after spinning at 4 KHz for 30 min is that asphalt AAK-1 has the highest asphaltene content of the three asphalts. However, more experiments are required to verify this phenomenon.

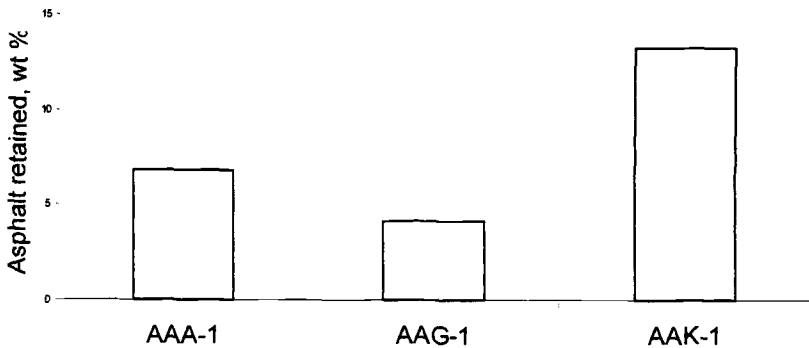


FIG. 2b—Percentage of asphalt retained after spinning at 4 kHz for 30 min.

Low Temperature Characterization by Differential Scanning Calorimetry

Differential scanning calorimetry (DSC) is the method most frequently used to determine the glass transition of polymers. However, the use of differential scanning calorimetry (DSC and/or modulated DSC) in asphalt-aggregate systems has both strengths and weaknesses. The main strength is that the heat flow characteristics of asphalts and mastics can be measured using the same configuration and the same instrument. A weakness of the technique is that the signal is proportional on first approximation to the asphalt content of the mastic. A further reduction of the transition height due to large scale interactions is the change of interest, and some mastic blends produce signals too small to be measured. Of course, low signal levels also increase the errors of measurement.

The results for the aggregate studies, as shown in Fig. 3a, tend to form a group near and slightly below the no-interaction line. In addition, the glass transition temperatures of these mastics exhibit little variance. These observations suggest that the components of asphalt attaching to an aggregate surface are not those contributing substantially to the glass transition properties. They are not flexible materials at low temperature in the original asphalt, and thus,

when attached to aggregate surfaces, they do not greatly affect the glass transition. Note that most values shown in Figs. 3a and b are averages of up to six individual experiments. Statistical analyses of measurements can be found in [8].

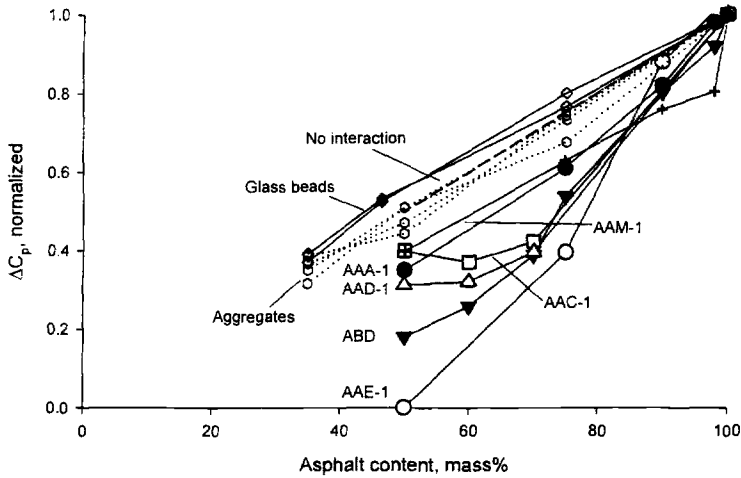


FIG. 3a—Changes in glass transition temperature with aggregate type and asphalt content.

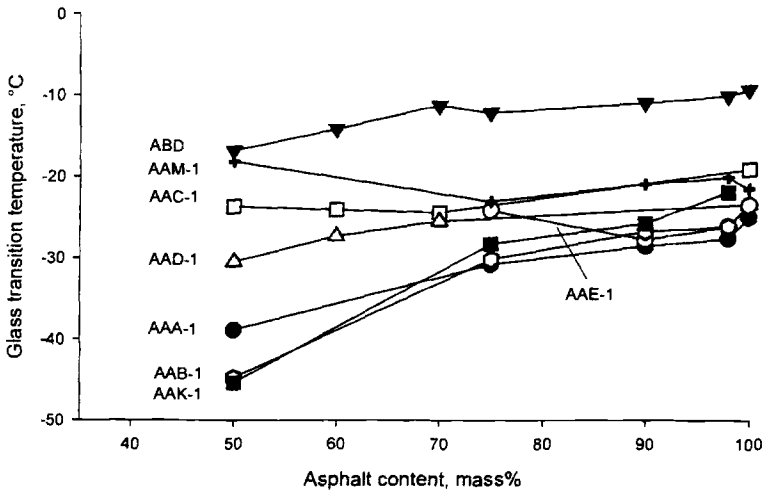


FIG. 3b—Changes in glass transition temperature with asphalt content in silica gel mastics.

The results for the aggregate mastics showed only small, although interesting and statistically significant, effects due to asphalt-surface interactions. To confirm and extend this study, an aggregate with a highly interactive surface was needed. Silica gel was chosen because of its high interaction with asphalt, its consistent size, and its predetermined specific surface area. The

results for eight asphalt-silica gel mastic combinations at various asphalt contents are shown in Fig. 3b. The interaction of asphalts with the silica gel is much stronger than with the glass beads or either of the aggregates studied. In the extreme case of asphalt AAE-1, an air blown AAA-1, there is little interaction at 10 % silica gel and complete rigidity at 50 % silica gel, where the glass transition is too small to identify unambiguously. Asphalt ABD (the parent asphalt of AAG-1, which is lime-treated) behaves similarly, but still has some flexible amorphous content at 50 % silica gel content. Asphalts AAD-1 and AAC-1 show a decrease in the height of the specific heat capacity at low silica gel contents, followed by a leveling at higher silica gel contents. Since it is unlikely that there is a larger fraction of flexible amorphous material at higher silica gel contents, the leveling may just be an indication of the limits of this technique. It is difficult at high silica gel contents to perform the curve fits on the modulated DSC scans.

Even with the uncertainties at higher silica gel contents, the data show distinct asphalt-specific differences. This is especially true of the glass transition temperatures (Fig. 3b) where, for example, asphalt AAK-1 has a change in temperature of over 20°C. Asphalts AAA-1 and AAB-1 show similar behavior. Asphalts AAM-1, AAC-1, and AAE-1, however, show little change in their glass transition temperatures with increasing silica gel content. Asphalts AAD-1 and ABD show intermediate behavior, having small decreases in their glass transition temperatures. The insensitivity of the glass transition temperatures of asphalts AAC-1, AAE-1, and AAM-1 is an indication that there is little difference between that material attaching and that material not attaching to the silica gel surface.

Rheological Characteristics by Specially Designed Sliding Plate Viscometer

The objective of this work was to develop a simple method to enable the interactions between thin asphalt layers and various aggregate surfaces to be rheologically measured. The practical application of such a method would be to improve the prediction of HMA performance by better understanding and accounting for the contribution of the oriented and/or structured asphalt in the asphalt-aggregate binding regions to the properties of pavement mixtures. The detailed information about the specially designed sliding plate viscometer can be found in [2]. It is well understood that the rheological behavior of asphalt is influenced by molecular structuring, crystallinity, and association forces. In the case of asphalt-aggregate mixtures, the importance of the asphalt binder flow properties becomes apparent when one considers the fact that under stress aggregate, particles slide past one another and cause shearing of the asphalt at the asphalt-aggregate interface. The shearing of aggregate particles during mixture preparation is assisted by the lubricating effects of the hot, low viscosity asphalt binder. As all of the aggregate particles are coated with asphalt, the achievement of inter-particle contact relies mainly on the shear flow of asphalt binder.

Figure 4 shows the thin-film (20 microns) rheological properties measured of asphalt AAD-1 on plates made of glass, granite, and limestone at 25°C. The data using glass plates were in agreement with expectation and are near what one would expect with steel plates. There was little interaction between AAD-1 and the glass plates, and AAD-1 exhibits Newtonian flow at 25°C. On the other hand, AAD-1 obviously interacts strongly with the granite and limestone plates and exhibits non-Newtonian flow behavior. Viscosities measured using the granite and limestones (simulating the real world interaction of asphalts on aggregates) are much higher than the viscosities measured using the glass plates. Because the thickness of the monomolecular layer adsorbed on the mineral surfaces is much smaller than the thickness between plates (probably 3–4 orders of magnitude), one can conclude that the monolayer interaction between

asphalt and aggregate has induced a multilayer buildup of more ordered or structured molecules in the asphalt extending inward from the aggregate surface. If the magnitude of the viscosity values reflects the strength of the interaction with the plates, the limestone induces more highly oriented multilayers with AAD-1 than does granite. Here we may have the fundamental explanation as to why most pavements made with limestones are more resistant to permanent deformation than pavements made with most siliceous aggregates such as this granite.

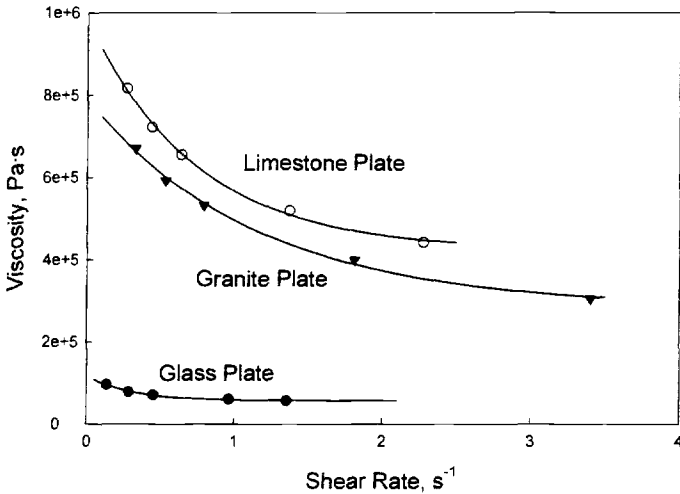


FIG. 4—Viscosity versus shear rate relationship for 20-μm film of asphalt AAD-1 with different plates at 25°C.

Interfacial Characteristics by Atomic Force Microscopy (AFM)

Contact mechanics models are commonly applied to predict the strength of adhesive bonding in polymers. Asphalts exhibit polymer-like characteristics including adhesive and viscoelastic properties. The work of adhesion, interpreted based on contact mechanics models such as the Johnson-Kendell-Roberts (JKR) contact theory and the DMT (Derjaguin-Muller-Toporov) approach [9–12] have been applied to measure the surface energies for eight asphalts in thin film samples solvent cast onto glass slide substrates. It is hypothesized that the work of adhesion between aggregate particles and asphalt binders directly relates to a pavement’s tendency to microcrack and to heal. To determine the work of adhesion, AFM is employed to measure force curves acquired as a function of contact loading and sampling frequency. The procedure uses cantilevers with 5 μm glass bead tips.

The pull-off force, F_s , is derived in terms of a maximum negative magnitude in F , the load force, just before detachment of two surfaces from each other, as the contact radius, r , between them remains constant.

$$F_s \propto \frac{(F_E * -F)^2}{3Kr} = -4\pi\gamma_{12}r^2 \tag{1}$$

Here, F_E^* is defined as an elastic Hertzian contact-force, K is a reduced bulk modulus, and γ_{12} is the interfacial surface energy between surfaces 1 and 2. By substituting r^2 by the term $R\delta$, where R is the radius of a spherical surface in contact with a flat surface, which is displaced by some small distance δ just before detachment of the two surfaces from each other, the pull-off force is re-derived as

$$F_S \equiv \frac{(F_E^* - F)^2}{3\delta K r} = -4\pi R \gamma_{12} \quad (2)$$

The DMT (Derjaguin-Muller-Toporov) approach [9,11,13,14], which gives the same magnitude of “contact” force but is opposite in direction to the JKR pull-off force, has been considered for interpreting data from AFM force-distance contact mechanics measurements. The DMT theory describes the interaction force, $F(D)$, acting between a flat surface and a spherical surface of radius, R , which is related to the interaction energy per unit area, $W(D)$, at some distance of separation, D .

$$F(D)_{spheric} = 2\pi R W(D)_{flatplane} \quad (3)$$

Under equilibrium conditions,

$$W(@D \rightarrow 0) = 2\gamma \quad (4)$$

such that,

$$F_S = 4\pi R \gamma \quad (5)$$

Generally speaking, the DMT approach is applied when the sphere of radius R is described as a small rigid body. By contrast, the JKR approach usually applies to a larger deformable spherical body.

Force curves for the eight asphalts were measured on $1 \mu\text{m}$ (approximated) solvent-cast thin films using a Digital Instruments MultiMode™ scanning probe microscope and a silicon cantilever with a $5 \mu\text{m}$ spherical glass tip [15]. The sample rate, which is the average velocity at which the tip approaches and retracts from the surface, had velocities ranging between 4.0×10^{-6} and 2.6×10^{-2} cm/s, with approach and retract velocities equal. Force curve data were collected for the eight asphalts on $1 \mu\text{m}$ films.

Typically, surface energy versus contact loading and surface energy versus tip deflection plots are constructed from force-distance AFM data. Actual “equilibrium” surface energy values are obtained by extrapolation to a minimum loading or a minimum tip deflection. With large tip deflections, the cantilever is “displaced” over a much greater distance compared to low values of tip deflection, where the cantilever is moved only a short distance as pull-off force measurements are made. Figure 5 depicts surface energy versus deflection (Fig. 5a) and surface versus load force (Fig. 5b) plots for asphalt AAM-1. It can be seen that the tip deflection varies between 50 nm and 200 nm, and load force varies between 0 and 7800 dynes. Based on observations of surface energy values derived by considering the tip deflection or load force-versus-surface energy data, extrapolated surface energy results were estimated to vary between 30 dynes/cm for asphalt AAM-1 to as high as 60 dynes/cm for asphalt AAD-1.

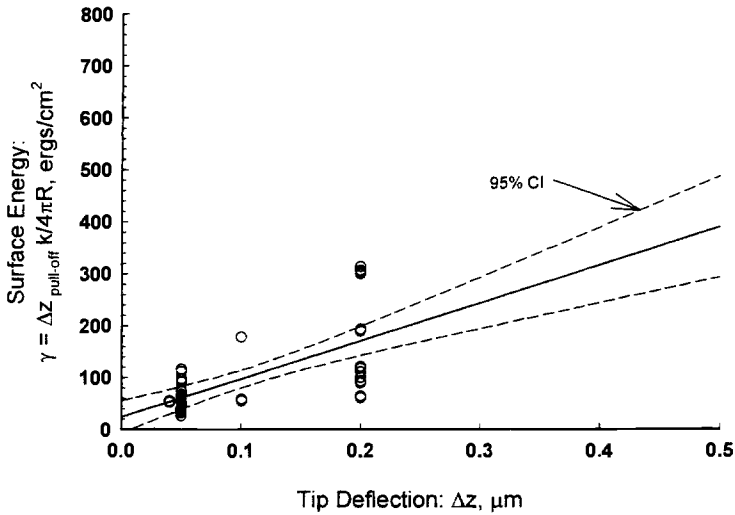


FIG. 5a—Tip deflection-versus-surface energy plots for asphalt AAM-1, derived from pull-off force data using Force-Distance AFM.

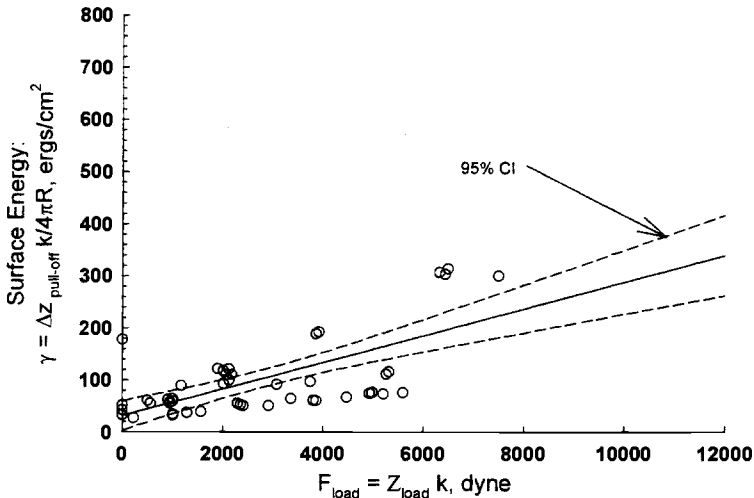


FIG. 5b—Loading force-versus-surface energy plots for asphalt AAM-1, derived from pull-off force data using Force-Distance AFM.

The shapes of the force curves further indicate that two distinctly different behaviors in “pull-off” are apparent. For example, force curves measured for less compatible asphalts of lower molecular weight, such as asphalt AAD-1 (Fig. 6a), fail abruptly as the tensile stress of the material increases nearly linearly up to a point of sudden failure with applied pull-off force. The contact area between the tip and the surface is assumed to remain constant up to the point of

failure with little indication of plastic deformation. The force curves for these “types” of asphalts show little or no sensitivity to sampling frequency. By comparison, force curves collected for higher molecular weight compatible asphalt, such as AAM-1 (Fig. 6b), were found to be distinctly different from lower molecular weight, less compatible asphalts. For this type of asphalt, the tensile stress portion of the force curve showed a distinct curvature, and failure was less abrupt, particularly in force curves collected at low frequencies. The shapes of these force curves changed significantly as the frequency was increased, where they became more like force curves collected for the less compatible asphalts. These results are not unlike findings by other investigators [16], where the shape of the force curve is dependent on the molecular weight of the material. In the referenced case, the material was a polymer that varied considerably by molecular weight. In general, asphalts that contained higher contents of petroleum wax (Table 1) were found to exhibit “necking” (i.e., a distinct curvature with less abrupt failure in the pull-off) in the unloading region of the force curve.

Interactions between asphalt molecules and mineral surfaces can affect the mobility of the molecules. Selective adsorption of asphalt components can also change naturally occurring hydrophilic filler surfaces to hydrophobic surfaces. It is proposed that for active fillers, the most polar and most strongly adsorbed components form the first adsorbed layers. Then through multilayer build up, the adsorbed layer is less strongly adsorbed because of weaker induced attractive forces from the aggregate and/or adsorption of less polar molecules. This process continues to a point where the interface no longer influences adsorption. Of course, the specific distance at which the interface ceases to influence adsorption depends on the degree of activity of the filler with the specific asphalt components and the polarity and special orientation of the asphalt molecules. The adsorbed components of the asphalt become structured, and the molecular mobility decreases. Thus, the multilayered adsorbed components are more rigid than the neat asphalt. When this rigid layer is involved in bonding, stiffer bonds are formed that have greater resistance to deformation. This phenomenon is important, since in asphalt pavement mixtures, it is desirable to use active fillers that will increase stiffness and elasticity.

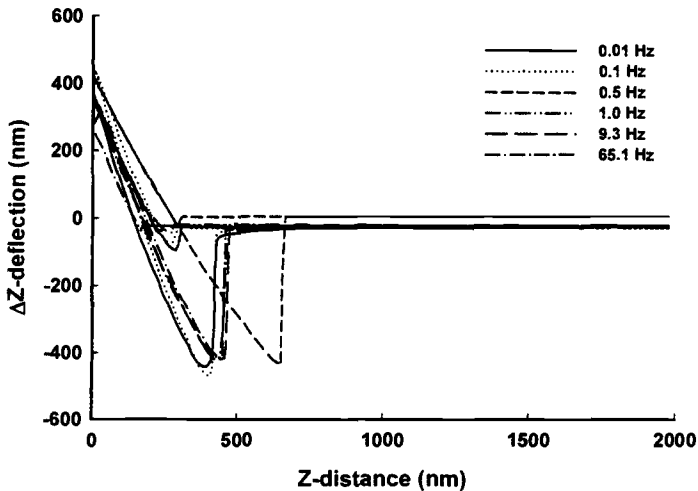


FIG. 6a—AFM force curve of asphalt AAD-1 measured as a function of contact rate at constant loading.

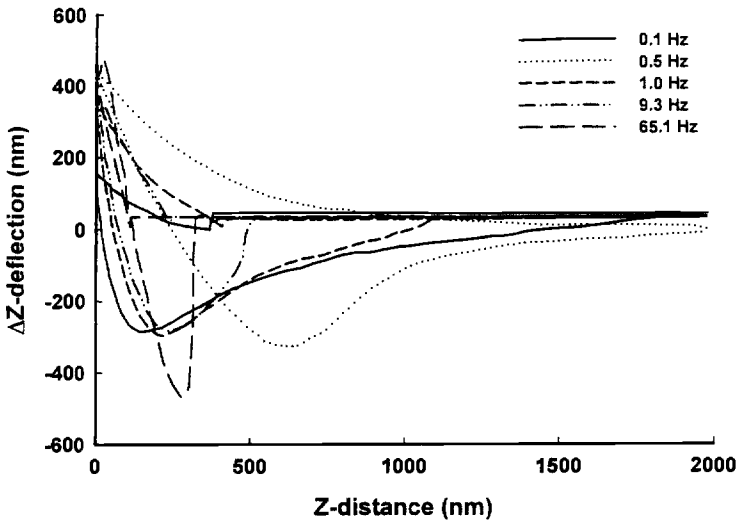


FIG. 6b—AFM force curve of asphalt AAM-1 measured as a function of contact rate at constant loading.

Results from this work should be useful in selecting those materials necessary to achieve improved performance, and in time be useful in developing a standardized test for classifying asphalts and aggregates according to their expected performance in mixtures. Undoubtedly not only the amount of asphalt components adsorbed is important, but also the chemical type that is adsorbed. This should be of particular importance with regard to the resistance of pavements to distresses (moisture damage, rutting, fatigue cracking, etc.). These predictions, of course, must be examined in terms of the performance of actual pavements.

Summary and Conclusions

Several different analytical techniques have been employed to study interactions between asphalts and inorganic substrates in various systems. These analytical results also demonstrated that each technique has possibilities for use, depending on the nature of the system to be studied. More specific conclusions can be addressed as follows:

- 1) The pulverized aggregates can be used as chromatographic supports to separate solutions of asphalts (in cyclohexane) into polar and non-polar components. The pulverized aggregate behaves as a chromatographic adsorbent and adsorbs polar components from the asphalt. The relative amounts and types of the polar components adsorbed on the pulverized aggregate are a function of chemical compositions of the particular asphalt-aggregate combination. The intensity of the adsorption of asphalt components onto filler surfaces can be quantitatively evaluated by measuring the amount of polar materials adsorbed onto the aggregate surfaces.
- 2) The preliminary experiments conducted with the high-speed NMR spinner indicated that the spinner can be a simple and rapid method to evaluate what types of asphalt

- components strongly adhere to an aggregate surface.
- 3) Differential scanning calorimetric (DSC) evidence suggests the possibility of using this thermal method to identify a rigid, amorphous fraction formed by the immobilization of a surface layer of binder in contact with aggregate.
 - 4) Using the most current design of the sliding plate viscometer, which uses machined aggregate plates, it was clearly shown that the effects of aggregate surface-induced structuring on the rheological properties of asphalt binders in the thin film region at the asphalt-aggregate interface can be measured.
 - 5) An experimental protocol using AFM has been developed to measure surface energies of asphalt on glass plates. Force curves were collected on 1 micron asphalt thin films by contact measurements with Silicon cantilevers using a Digital Instruments MultiMode TM scanning probe microscope equipped with a thermally controlled heating stage. The theories of the Johnson-Kendell-Roberts (JKR) contact and the Derjaguim-Muller-Toporov (DMT) approach have been employed to model air-asphalt film and asphalt film-glass substrate interfacial system.

All above-mentioned tests are relatively rapid methods. The method(s) that is (are) most predictive of pavement performance will be employed for further development of a test method for measurement of the adhesion properties between the asphalt and the aggregate surface.

Acknowledgments

The authors gratefully acknowledge the Federal Highway Administration, U.S Department of Transportation, for financial support of this project under contract no. DTFH61-99C-00022. Thanks are also expressed to Mr. James Beiswenger, Mr. Gerald Forney, Ms. Julie Miller, Ms. Janet Wolf, and Mr. Stephen Salmans. Thanks are also expressed to Ms Jackie Greaser for preparation of the manuscript.

References

- [1] Jones, D. R., "SHRP Materials Reference Library, Asphalt Cements: A Concise Data Compilation," ASHRP-A-645, Strategic Highway Research Program, National Research Council, Washington, DC, 1993.
- [2] Western Research Institute, "Fundamental Properties of Asphalts and Modified Asphalts, Draft Final Report, Volume 2, New Test Methods," Federal Highway Administration, Contract No. DTFH61-99C-00022, submitted for review, October 2003, pp. 23-27;157-176.
- [3] Petersen, J. C., "Quantitative Functional Group Analysis of Asphalts Using Differential Infrared Spectrometry and Selective Chemical Reactions - Theory and Application," *Transportation Research Record 1096*, 1986, pp. 1-11.
- [4] Plancher, H., Dorrence, S. M., and Petersen, J. C., "Identification of Chemical Types in Asphalts Strongly Adsorbed at the Asphalt-Aggregate Interface and Their Relative Displacement by Water," *Proceedings, Association of Asphalt Paving Technologists*, Vol. 46, 1977, pp. 151-175.
- [5] Petersen, J. C., Plancher, H., Ensley, E. K., Venable, R. L., and Miyake, G., "Chemistry of Asphalt-Aggregate Interaction: Relationship with Pavement Moisture-Damage Prediction Test," *Transportation Research Record 843*, 1982, pp. 95-104.

- [6] Petersen, J. C., Barbour, R. V., Dorrence, S. M., Barbour, F. A., and Helm, R. V., "Molecular Interactions of Asphalt. Tentative Identification of 2-Quinolones in Asphalt and Their Interaction with Carboxylic Acids Present." *Analytical Chemistry*, Vol. 43, 1971, pp. 1491–1496.
- [7] Petersen, J. C., "An Infrared Study of Hydrogen Bonding in Asphalt." *Fuel*, Vol. 46, 1967, pp. 295–305.
- [8] Western Research Institute, "Fundamental Properties of Asphalts and Modified Asphalts. Draft Final Report, Volume 1, Interpretive Report," Federal Highway Administration, Contract No. DTFH61-99C-00022, submitted for review, October 2003.
- [9] Kinloch, A. J., *Adhesion and Adhesives Science and Technology*, Chapman and Hall, New York, 1987, pp. 339–400.
- [10] Hui, C. Y. and Baney, J. M., "Contact Mechanics and Adhesion of Viscoelastic Spheres." *Langmuir*, 1998, Vol. 14, pp. 6570–6578.
- [11] Israelachvili, J., *Intermolecular & Surface Forces*, 2nd ed., Academic Press Limited, Academic Press Inc., San Diego, CA, 1992.
- [12] Pollock, H. M., Maugis, D., and Barquins, M., "The Force of Adhesion Between Solid Surfaces in Contact," *Applied Physics Letters*, Vol. 33, No. 9, 1978, pp. 798–799.
- [13] Derjaguin, B. V., Muller, V. M., and Toporov, Y. P., "Effect of Contact Deformations on the Adhesion of Particles," *Journal of Colloid Interface Science*, Vol. 50, 1975, pp. 314–326.
- [14] Sarid D., *Scanning Force Microscopy With Applications to Electric, Magnetic and Atomic Forces*, Revised ed., Oxford University Press, Inc., New York, 1994.
- [15] Pauli, A. T., Grimes, W., Huang, S. C., and Robertson, R. E., "Surface Energy Studies of Asphalts by AFM," *American Chemical Society Division of Fuel Chemistry Preprints*, Vol. 48, No. 1, 2003, pp. 14–18.
- [16] Wang, X. P., Xiao, X., and Tsui, O. K. C., "Surface Viscoelasticity Studies of Ultrathin Polymer Films Using Atomic Force Microscopic Adhesion Measurements," *Macromolecules*, Vol. 34, 2001, pp. 4180–4185.

David J. Moonay, Ph.D.¹

New Technique for Measuring Extended Viscosity Ranges - Gel Times, Pot Life, or Cure Monitoring - with Programmable Rotational Viscometers or Rheometers

ABSTRACT: A new algorithm written in commercially available software controls programmable viscometers and rheometers so that multiple decades of apparent viscosity data may be acquired. This work is new and important because previous methods involved either: (1) very simple instrumentation providing (a) single-point viscosity data or (b) equipment providing "gel times" but no viscosity data, or (2) complicated instrumentation costing at least \$20 000. Isothermal cure of a common epoxy system was successfully monitored in this work. Apparent viscosities measured during one room-temperature cure experiment ranged from approximately 1000 mPa·s to 50 000 000 mPa·s. Good repeatability of data was found for different batches prepared with similar stoichiometry. Viscosities measured at approximately 167 min of cure time, during multiple tests, differed by less than 1 %. Various test geometries were used, including disposable cylindrical spindles and sample chambers, to allow easy cleanup, with samples 10 mL or less in size. Samples were also successfully tested at 50 and 60°C. Aspects of the algorithm and its implementation are discussed. It is hoped that this new method will help personnel testing adhesives.

KEYWORDS: Brookfield, epoxy, gelation, cure, viscosity, viscometer

Introduction

This work arose because customers in different industries indicated that their "generic" or simple gel timers provided no viscosity data. Commercially available equipment, capable of monitoring large viscosity increases during cure, is far too expensive for typical quality control/quality assurance or "QC/QA" laboratories. These sophisticated devices often cost at least \$20 000 or more. Furthermore, simple tests, such as measuring viscosity after a 24-h wait time, provide only one data point and, as a result, may not reveal significant changes in material processability during the cure before that time. Therefore, the question from a practical standpoint is: How does one monitor viscosity during gelation, affordably?

The Brookfield DV-II+-series rotational viscometers and DV-III-series rheometers have a built-in *Time-to-Torque* feature. The selected instrument is run in stand-alone mode, at one constant speed with one spindle. The motor rotation automatically stops at a user-selected torque reading that is a percent of full-scale range or "FSR." The elapsed time and the setpoint torque are then shown on the instrument's display. This system can therefore be used as a type of gel timer - the instrument monitors the torque increase to 90 % of full-scale range, for example, as the sample's viscosity increases during gelation. However, it is a "one-point" test - that is, only one data point is acquired. If the instrument's "continuous printing" mode is selected and a

Manuscript received 29 September 2004; accepted for publication 23 February 2005; published September 2005.
Presented at ASTM Symposium on Advances in Adhesives, Adhesion Science, and Testing on 4-6 October 2004 in Washington, DC.

¹ Sales Engineer - Rheology Laboratory Supervisor, Brookfield Engineering Laboratories, Inc., 11 Commerce Boulevard, Middleboro, MA 02346.

nonzero data output interval selected. then the resulting data string can be output to and printed by a line printer, such as a commercially-available. parallel- or serial-port dot-matrix printer. However, this technique is still limited in its viscosity range and, therefore, will monitor only part of the curing process.

We recommend that measurements with rotational viscometers/rheometers be made between 10 % and 100 % FSR. Therefore, a recommended measurement, proceeding from 10–90 % FSR, may only correspond to a 10-fold increase in viscosity. However, it may be useful to characterize the material's rheology over a significantly greater range, to get a better idea of the working time, pot life, or processability window. This author envisioned that a much greater viscosity range could be accessed, by decreasing speed as the viscosity increased, to keep the readings onscale - that is, within the torque range of the instrument. Additionally, the *apparent* viscosity is measured, in many cases, because the samples are often non-Newtonian or become non-Newtonian as the gelation proceeds. The formal hypothesis, H_0 , is: Automatically decreasing the speed at user-selected, maximum torque setpoints should allow multiple decades of apparent viscosity to be measured.

The spring torque range of a given instrument is fixed. Torque, exerted upon the spindle that is immersed in the sample, is transferred through the coupling/transducer system of the Brookfield instrument. Therefore, the rotating spring will mechanically equilibrate at a particular degree of wind-up in response to an input torque from the spindle rotating in the sample. An appropriate spring torque range and spindle geometry are used, so that the initial spindle rotation speed may be high, say 100 rpm, while initially generating onscale torques, say 10 % of full-scale range, in the early stage of the gelation. Gelation results in a viscosity increase and a corresponding measured torque increase. Once the preselected torque maximum, say, 90 % FSR, is reached, the speed is automatically decreased. The lower speed should allow the measured torque to decrease, so more [onscale] measurements may be taken. This is repeated through several speed decades, thus permitting the measurement of several decades of apparent viscosity.

Programmable Brookfield viscometers and rheometers may be controlled through the Brookfield programming command language. *Wingather*TM software is currently used for DV-II+ Programmable and Pro viscometers. The *Rheocalc*TM software is used for the DV-III-series rheometers, presently including the DV-III, DV-III+, and DV-III Ultra; it may also be used with the DV-II+ Pro. Both software packages are run with the instrument connected to a personal computer or "PC" via a RS-232 or serial port cable. The data are collected by the software and may then be saved as PC files. *Rheoloader*TM is a precursor to *Rheocalc*TM, and it allows programs to be downloaded into the DV-III+ or the DV-III Ultra; the program is stored in the rheometer's memory and then run with the instrument in standalone mode, detached from the personal computer. The data are output as text strings, through either a parallel or serial port connection, to dot-matrix line printers, for example. *DVLoader*TM is analogous to *Rheoloader*TM but is used with DV-II+ Programmable or DV-II+ Pro viscometers.

Experimental

Sample Materials

The model system was selected for study such that the components were commercially available and would provide a cure or chemical gelation time on the order of eight hours at room temperature: EPONTM Resin 828 and EPIKURETM 3046 (Resolution Performance Products,

Houston, TX). EPON™ Resin 828 is an epoxy oligomer made from bisphenol A and epichlorohydrin, while EPIKURE™ 3046 curing agent is an amidoamine mixture [1].

Procedure

EPON™ 828 and EPIKURE™ 3046 batches were prepared using 1:1 ingredient ratios by weight, for convenience. The former was weighed into the latter and the mixture rapidly stirred in a Pyrex® glass beaker by hand with a stainless steel spatula for a few minutes until homogeneous. Portions of a given batch were then weighed into the appropriate chamber and the test promptly started. Several test setups were used:

1. LVDV-III+ rheometers were set up with LV-4 spindles attached by SP-7Y Quick Connect Couplings. The Quick Connect couplings allowed the standard spindles to be easily disengaged from the viscometer at the end of the experiment. The resin + curing agent mixture was transferred into poly(ethylene) sample vials. Two separate batches were prepared - batch #1 was transferred into vials #1-3 and tested first. Batch #2 was prepared after the first test set was completed, and this batch was transferred to vials #4-6. Each vial was approximately 64 mm high, approximately 13 mm in diameter, and held approximately 5.5 mL. Each vial was clamped to its rheometer stand so that (a) the vial was essentially vertical and (b) the vial was centered about the immersed spindle.

The reactions were monitored at ambient conditions, 23°C. Programs created in Rheolader™ software were downloaded to two instruments, through a laboratory personal computer's (PC's) serial or RS-232 port. These rheometers were then disconnected from the PC and run in Standalone mode. The subsequent data output was sent to dot-matrix line-printers via parallel-port connections from each instrument. A third instrument was run in External mode using Rheocalc™ software for instrument control and data acquisition. The data were saved as a file on the PC. Three separate aliquots from each given batch were simultaneously tested, using the three instruments.

2. LVDV-III+ rheometers were used with LV-4 spindles and SP-7Y Quick Connect Couplings. The reaction mixtures were contained in SC4-13RD disposable sample chambers. Brookfield Thermosel™ heaters with Programmable Temperature Controllers were used and the epoxy cures studied at (1) 50°C and (2) 60°C. The control and data acquisition algorithm was run through a Rheocalc™ software program.

3. RVDV-III+ and RVDV-II+ Pro instruments were used with SC4-27 disposable spindles, SC4-13RD disposable sample chambers, Thermosel™ heaters, and Programmable Temperature Controllers. These experiments were performed at 60°C. The spindles were held in a chuck, which was easily tightened and loosened by hand. Two reaction batches were prepared. The first batch was transferred into chambers "A" and "B" and promptly tested. The second batch was prepared after the completion of the first set of analyses, placed into chambers "C" and "D," and tested. Aliquots "A" and "C" were analyzed with the RVDV-II+ Pro and Wingather™ software, while "B" and "D" were monitored with the RVDV-III+ and Rheocalc™ software.

The algorithm was constructed such that data would be output at regular intervals; higher-temperature tests had faster reactions and viscosity increases, so the data output intervals were set somewhat shorter than for the room temperature tests. The speed, initially 100 rpm, was decreased by one decade each time the torque at the set speed reached 90 % FSR. An additional data string was output immediately after each speed change. The algorithm then waited for a set

amount of time before beginning to check the torque reading against the 90 % FSR setpoint at the new speed. This delay was such that the spring mechanically equilibrated for at least two minutes at the new, lower speed, and thus prevented the instrument from mistakenly decreasing speed by another decade.

Results and Discussion

Figure 1 is a graph of torque versus time for an EPONTM Resin 828 + EPIKURETM 3046 sample cured at room temperature, 23°C. A Brookfield LVDV-III+ with LV-4 spindle and Quick Release coupling was used, and the sample was measured in a small poly(ethylene) vial, mentioned above. The initial speed was 100 rpm and decreased in decade steps each time 90 % torque was reached. Figure 2 shows the speed steps during the same experiment. Five speeds were used, covering four decades of speed. Nearly five decades of viscosity were measured, because the torque is measured from approximately 10–90 % of full-scale range at each speed.

Figure 3 shows the calculated apparent viscosities as a function of time at 23, 50, and 60°C. The material at 23°C was tested in a poly(ethylene) vial. The latter two experimental procedures were conducted using the disposable sample chambers discussed above. The disposable chambers were aluminum and thus conducted heat very quickly. Therefore, it is not surprising that the viscosities at low extents of reaction - corresponding to low reaction times - are less for the heated materials than for the epoxy tested at ambient conditions. It is noteworthy that this technique successfully monitored cures over time periods varying by almost two orders of magnitude. The significantly decreased reaction time - or increased reaction rate - with increasing temperature, is as expected.

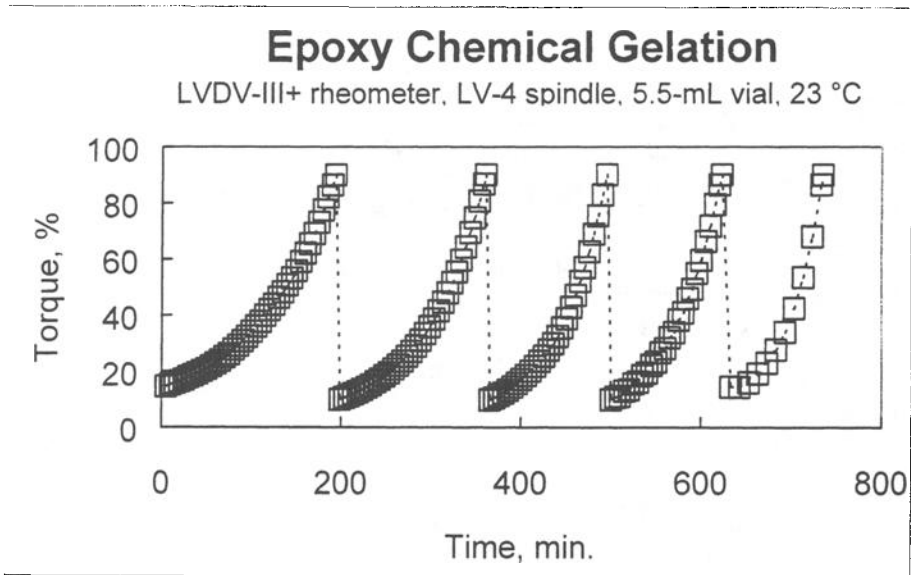


FIG. 1—Torque versus time for room-temperature epoxy cure.

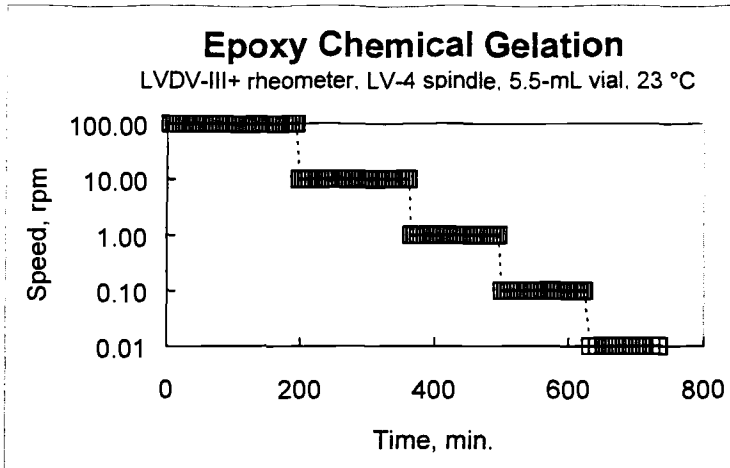


FIG. 2—Speed versus time for room-temperature epoxy cure.

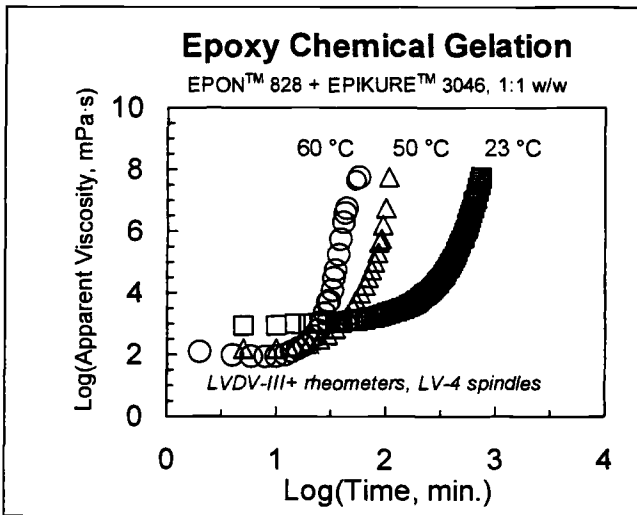


FIG. 3—Epoxy cure at 23, 50, and 60°C.

Repeatability between similarly-prepared batches appeared to be satisfactory. This is shown in Fig. 4. Some of the data, though not all, are shown, for the sake of clarity. Data were selected at nearly identical test times, from the printouts and the data files. Data at approximately 167 min - approximately 2.2 on the log-time axis - agree to within $\pm 1\%$ of each other. Figure 5 shows data for experiments run at 60°C. Reasonably good agreement is again seen, between data sets. The time to reach an apparent viscosity of about 2 million mPa.s ranged from approximately 63 min for run "B" to 68 min for run "C." Good repeatability of this technique

was also previously demonstrated with thermoreversible gels of chemically different systems in nonisothermal runs [2].

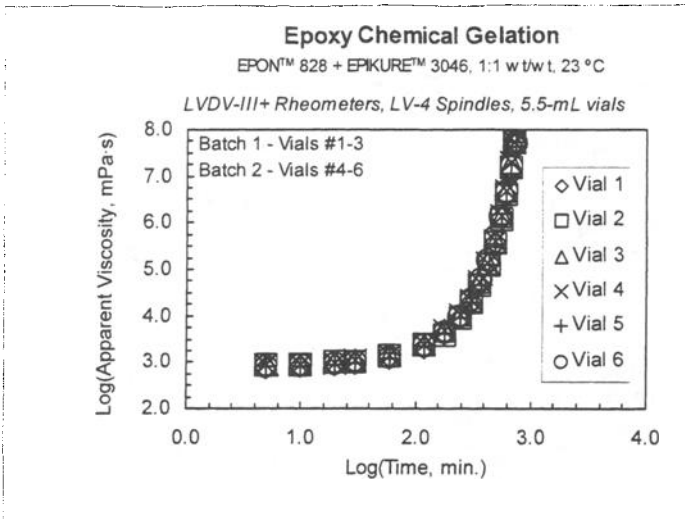


FIG. 4—Comparison of epoxy cure behavior between different runs at 23°C.

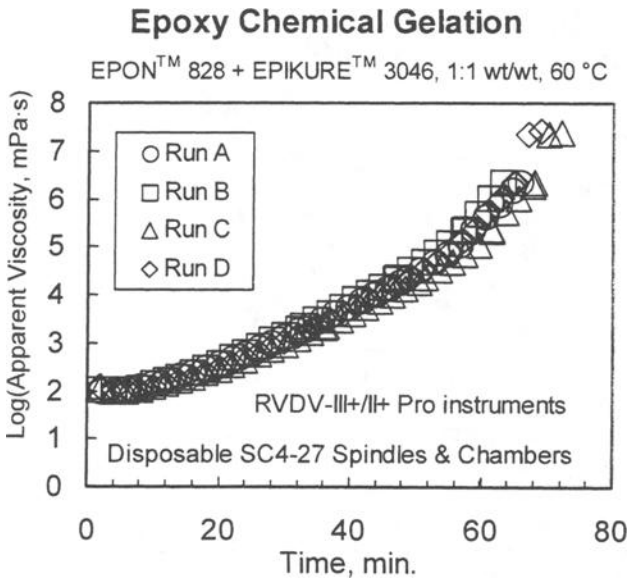


FIG. 5—Comparison of multiple batches' epoxy cure at 60°C.

Table 1 lists representative data from vial 2, analyzed at 23°C:

TABLE 1—Epoxy gelation data for vial 2 at 23°C.

| Speed, rpm | Torque, % | Viscosity, mPa·s | Time, h |
|------------|-----------|----------------------|---------|
| 100 | 14.7 | 864 | 0.0833 |
| 100 | 22.8 | 1 370 | 1.00 |
| 100 | 38.7 | 2 320 | 2.00 |
| 100 | 66.5 | 3 990 | 3.00 |
| 10 | 15.1 | 9 060 | 4.03 |
| 10 | 31.8 | 19 100 | 5.03 |
| 10 | 77.2 | 46 300 | 6.03 |
| 1 | 21.6 | 1.30×10 ⁵ | 7.11 |
| 1 | 63.3 | 3.80×10 ⁵ | 8.11 |
| 0.1 | 66.9 | 4.01×10 ⁶ | 10.2 |
| 0.01 | 25.2 | 1.51×10 ⁷ | 11.2 |
| 0.01 | 90.0 | 5.40×10 ⁷ | 12.1 |

The above data were taken at the beginning of the experiment - about two minutes of reaction time - and then at roughly one-hour intervals. The run automatically stopped after the last data point was recorded - that is, after the 90 % torque setpoint was reached at the lowest speed, 0.01 rpm. The data for this particular experiment spanned almost five decades of viscosity.

This technique appeared to be very successful for epoxy samples with cure times on the order of about one hour or more. There may be some concern about the system response for *fast-curing* materials at high extents of reaction, however, because the Brookfield viscometer's or rheometer's spring mechanical equilibration time may be slow at very slow speeds such as at 0.01 rpm, for example. Therefore, there may be some measurement artifact or inaccuracy at the highest viscosities measured at high extents of reaction. However, the rheological behavior or trend is still shown - the sample is a gel and becoming almost solid. Thus, even these data are still useful as a QC tool.

Conclusions and Recommendations

The novel control algorithm worked successfully. Automated, multidecade monitoring of viscosity during gelation of a commercial epoxy was demonstrated with satisfactory repeatability. These experiments were performed with instruments that are affordable for many users in the QA/QC realm and relatively simple to use. Additionally, the utility and convenience of disposable sample chambers was demonstrated for this application as well. This technique may be appropriate, by analogy, for determining "pot life" or "working time" of various materials, because these time periods are those in which viscosity is increasing to some user-determined limit. It is recommended that this algorithm be tested with other materials to gain additional insights into its optimization.

Acknowledgments

The author thanks Brookfield Engineering Labs, Inc., for permission to present this report. I thank my colleague, Sherman Caswell (Senior Sales Engineer), for suggesting that this work be presented to the Adhesives community. Thanks are also given to Resolution Performance

Products, L.L.C., which kindly provided free samples of the EPON™ Resin 828 and EPIKURE™ 3046.

References

- [1] "Physical Properties Guide for Epoxy Resins and Related Products," Resolution Performance Products, L.L.C., Houston, TX, 2001.
- [2] Moonay, David J., "Multi-Decade Viscosity Analyses During Chemical and Thermoreversible Gelation, Using Brookfield Viscometers or Rheometers and a Novel Control Algorithm," Poster paper #271 presented at the Society of Rheology 75th Annual Meeting, Pittsburgh, PA, October 13–16, 2003.